Ruprecht-Karls-Universität Heidelberg
Naturwissenschaftlich-Matematische Gesamtfakultät

Quantitative Analysis of the Structural Dynamics of Mitotic Chromosomes in Live Mammalian Cells

Dissertation

Felipe Mora-Bermúdez

Heidelberg, April 2006

Dissertation

submitted to the
Combined Faculties for the Natural Sciences and for Mathematics
of the Ruperto-Carola University of Heidelberg, Germany

for the degree of

doctor rerum naturalium

Presented by
M.Sc. Biologist Felipe Mora-Bermúdez
Born in San José, Costa Rica

Oral examination:_____

Quantitative Analysis of the Structural Dynamics of Mitotic Chromosomes in Live Mammalian Cells

Referees:

Dr. Damian Brunner
European Molecular Biology Laboratory (EMBL)
Meyerhofstrasse 1, D-69117, Heidelberg, Germany.

Prof. Dr. Renato Paro,
Zentrum für Molekulare Biologie der Universität Heidelberg (ZMBH). Im Neuenheimer Feld 282, 69120 Heidelberg, Germany

Examiners:

Dr. Iain Mattaj
European Molecular Biology Laboratory (EMBL)
Meyerhofstrasse 1, D-69117, Heidelberg, Germany.

Prof. Dr. Peter Lichter
Deutsches Krebsforschungszentrum (DKFZ)
Im Neuenheimer Feld 280, 69120 Heidelberg, Germany.

The following work was performed at the European Molecular Biology laboratory (EMBL), Heidelberg, from October 2002 to April 2006, in the laboratory and under the supervision of Dr. Jan Ellenberg.

I herewith declare that, under supervision, I independently wrote the following doctoral dissertation, using none other than the sources and aids listed. Also, during this work, the principles and recommendations in "Verantwortung in der Wissenschaft" (Responsibility in Science), by the Ruprecht-Karls-Universität Heidelberg, were observed.

20th of April, 2006

_____ _____

Date Signature

Bruscamente la tarde se ha aclarado
porque ya cae la lluvia minuciosa.

Jorge Luis Borges

(Suddenly the afternoon has cleared
as now the thorough rain is falling.)

I Table of Contents

II Acknowledgments

I would like to sincerely thank Jan for welcoming me in the group and mentoring me through this project. From the personal and professional points of view, it has been a pleasure to work here. Jan has been a personally kind but scientifically and technically challenging supervisor, a combination that I have cherished. I am thankful for the opportunity he has given me to express and follow my ideas, while at the same time directing, improving and correcting them.

Simply all of this work has been catalyzed by the constant training and help from each member of the group. Not a single day goes by in which I don't realize how the supportive atmosphere in the lab makes the work more enjoyable. Together with Jan, the fabulous team that was Joël, Daniel, Gwén and Péter during the first part of this project is to thank for what I know about imaging and image processing. I have had great collaborations with Daniel, Joël and more recently with Aurélien, and the results are an important part of the work I here present. Gwén's input and his macros have also greatly facilitated this work, and I had loads of fun with Péter in establishing imaging assays with the Leica. Nathalie's molecular biology and lab-organizing skills have made even tedious protocols more enjoyable, and Katharina made the biochemistry-trainned rookie feel more at ease in the early times. Lucia has also brightened-up the lab, and our spinning and resurging, expanding and diffusing conversations have been a lot of fun. I need two more minutes... before I can thank Antje for her witty way of easing-up the day and, together with Melina and Elisa, for the help with the Zusammenfasung and making sure I have lunch every day. Esther and Claudia were fun colleagues and the MitoCheck cousins have always been helpful with reagents and discussions.

I have also enjoyed fruitful collaborations with groups outside of embl, for example with Helga and Philippe at the University of Oslo. Also with Nathalie, Karl and Roland at the DKFZ, within the Mitocheck frame. Promising results from these ongoing projects are also included here.

The Gene Expression and Cell Biology/Biophysics crowds have been a fun bunch to have around, go for a beer, etc. I thank Melpi, our honorary group member, for nice discussions and help with the DeltaVision, Mikko for help with biochemistry experiments and for his friendship, Julien for our ongoing assay development, Veronika for help with parts of this manuscript, people in the 2002 predoc generation for their friendship. Christina and Sylvia, who also organized Matthias's indispensable Kaffee, were also always helpful.

My friends have been supportive and always fun to be with, to relax, to think about something else when weeks and months of lablife would yield only background, but also to share the brighter moments. Bea, Roland, Silvia, Stoilka, die wunderbare "Pinte Truppe"... thank you.

I would like to deeply thank mi familia for always caring and supporting me, through the difficulties faced before and during these times, and through the easy moments too. Every letter and number, every nm and µl, every bit and byte and neural pulse offered here carries an inherent gratitude to all of you.

My appreciation goes also to Damian, Iain and Renato for being part of my thesis committee and supervising this project, and to Peter Lichter for being part of my defense committee.

This Project would obviously not have been possible without the EMBL environment and the funding provided by the DFG (grant No. EL 246/1-1 and grant No. EL 246/2-1/2)

III Abbreviations

Abbreviations used in this dissertation are here listed. Scientific international (SI) units and chemical symbols of elements, nucleic acids and amino acids are standard and thus not listed.

2D	Two-dimensional (lateral axis xy)
3D	Tri-dimensional (xy and axial axis z)
4D or xyzt	3D over time
aa	Amino acid
α	Alpha or antibody
amp	Ampicillin
AOBS	Acousto-Optical Beam Spliter
AOTF	Acousto-Optical Tunable Filter
BSA	Bovine Serum Albumine
cc	Concentration
CCD	Charge-Coupled Device
cDNA	Complementary DNA copy
C. elegans	*Caenorhabditis elegans*
ddH20	Double-distilled H20
dNTP	2'-Deoxyribonucleoside triphosphate
dsDNA	Double-stranded DNA
D. melanogaster	*Drosophila melanogaster* („fruit fly")
DMEM	Dulbecco's modified eagles medium
DMSO	Dimethyl sulphoxide
DNA	Deoxyribonucleic acid
EGFP	Enhanced GFP
E. coli	*Escherichia coli*
EDTA	Ethylen-diamine-tetra-acetate
EM	Electron Microscopy
EtBr	Ethidium bromide
FCS	Foetal calf serum or Fluorescecne correlation spectroscopy
FP	Fluorescent protein
FRAP	Fluorescence Redistribution (or recovery) after Photobleaching
FRET	Förster (or fluorescence) Resonance Energy Transfer
GFP	Green Fluorescent Protein
HeNe	Helium-Neon (laser tube)
Kan	Kanamicin
kb	kilo base pair
IgG	Immunoglobulin G
LB	Luria-Broth
m*FP	monomeric variant of an FP
MCS	Multiple Cloning Site
M. musculus	*Mus musculus* (mouse)
NA	Numerical Aperture
NEBD	Nuclear envelope break-down
nt	Nucleotide
O/N	Overnight
ORF	Open reading frame
p	Plasmid or pico
PA	Photoactivation

PAGFP	Photoactivatable GFP
PCR	Polymerase Chain Reaction
Plk	Polo-like kinase
PMT	Photomultiplier Tube
PNUTS	PP1 Nuclear Targeting Subunit
PP1	Protein Phosphatase1
PSF	Point Spread Function (Here intensity PSF)
r or rev	Reverse
RNA	Ribonucleic acid
RNAi	RNA interference
rpm	Revolutions per minute
RT	Room temperature
S. cerevisiae	*Saccharomyces cerevisiae*
SD	Standard deviation
siRNA	Small Interfering RNA
S. pombe	*Schyzosacharomices pombe*
Scr	Scrambled (RNA oligonucleoide with random, non-silencing sequence)
UV	Ultraviolet
X. laevis	*Xenopus laevis*
wt	Wild type

IV Zusammenfassung

Chromatin ist der physiologische Träger der genetischen und epigenetischen Erbinformation in Eukaryoten und liegt im Zellkern in Form von Chromosomen vor. Die Dynamik und Flexibilität der Chromatinstruktur ist essentiell für die Aktivitäten des Genoms. Die stärksten Veränderungen der Chromatinstruktur treten während der Mitose auf, wenn kompakte Metaphasechromosomen gebildet und gleichmässig auf zwei Tochterzellen verteilt werden. Die Mechanismen, die diesen Strukturänderungen zu Grunde liegen, sind *in vivo* bislang nur schlecht verstanden.

Im ersten Teil meiner Dissertation habe ich daher eine Methode entwickelt, mit der man die Kinetik der Chromosomenkompaktierung während der Teilung lebender Zellen quantitativ bestimmen kann. Zellen, die das fluoreszenzmarkierte Histon 2b stabil exprimierten, wurden mittels mehrdimensionaler Konfokalmikroskopie untersucht. Die Kompaktierung der Chromosomen wurde auf drei verschieden Größenebenen bestimmt. Mit Hilfe von vierdimensionaler Konfokalmikroskopie wurde das Volumen des Chromatins mit einer Auflösung von ~800 nm gemessen. Durch die statistische Auswertung von Pixel-Intensitäten konnte eine Auflösung von ~200 nm erreicht werden. Zur Messung auf molekularer Ebene (~10 nm) wurde ein FRET-Reporter am Carboxyterminus des nucleosomalen Histons 2b eingesetzt. Die Messungen zeigten, dass (i) die mitotische Kompaktierung bereits mindestens 20 Minuten vor der Prometaphase beginnt, (ii) Kompaktierung mit molekularen Konformationsänderungen in der Carboxyterminalen Region des Histons korreliert, und (iii) die maximale Chromatindichte nicht in der Metaphase, sondern erst in der späten Anaphase erreicht wird.

Im zweiten Teil meiner Arbeit habe ich mich auf diese erstmals beschriebene maximale Kompaktierung während der Anaphase konzentriert. Messungen an einzelnen Chromosomen zeigten, dass die Kompaktierung in der Anaphase durch eine Verkürzung ihrer Längsachse hervorgerufen wird, welche erst nach der Trennung der Chromatiden einsetzt. Diese axiale Verkürzung verlief unverändert in Condensin-depletierten Zellen, und war unabhängig von der Kinetochor-vermittelten Bewegung der Chromatiden zum Spindlepol. Trotzdem war die axiale Verkürzung abhängig von der Gegenwart intakter dynamischer Mikrotubuli. Akute Störung der Verkürzung führte zu stark gelappten Zellkernen in den Tochterzellen. Dieser Phänotyp weist darauf hin, dass die zusätzliche Kompaktierung in der Anaphase für den korrekten Aufbau der Zellkernarchitektur nach der Mitose notwendig ist. Des Weiteren wurde durch akute Störung der Anaphasen-Kompaktierung in Condensin-depletierten Zellen die Zahl der Segregationsdefekte dreifach erhöht. Dies deutet auf eine weitere Funktion der Anaphase-Kompaktierung als Sicherungsmechanismus gegen Segregationsdefekte hin.

Die entwickelte Methode zur Messung der Chromosomenkondensation wurde im dritten Teil meiner Dissertation verwendet, um die Funktion von PNUTS für die Regulation der Chromatinstruktur zu untersuchen. PNUTS ist eine regulative Untereinheit die Protein Phosphatase 1 in den Zellkern lokalisiert. In Zellen, in denen PNUTS durch RNAi depletiert worden war, war die Kompaktierung in Prophase dreimal langsamer als in Kontrollzellen. Unsere Kooperationspartner (Prof. Philippe Collas, Universität von Oslo) hatten zuvor *in vitro* zeigen können, dass Zugabe von PNUTS die Dekondensierung von Chromatin beschleunigt. Demzufolge ist PNUTS für die mitotische Chromatinstruktur sowohl *in vitro* als auch *in vivo* von Bedeutung und ein höchst interessantes Protein, um den unbekannten molekularen Mechanismus der Chromosomenkompaktierung im Detail zu untersuchen.

V Summary

Chromatin, organized into individual chromosomes, is the physiological carrier of the genetic and epigenetic information in eukaryotes. In the nucleus of an intact cell, the structure of chromatin is dynamic and essential for genomic activities. The most dramatic changes in chromatin structure occur in mitosis, when compact metaphase chromosomes are formed, organized and partitioned equally to two daughter cells. How this vital reorganization of chromatin is accomplished remains poorly understood *in vivo*.

To address this, in the first part of my thesis I developed quantitative assays to determine the kinetics of mitotic chromosome compaction, using multidimensional confocal microscopy of live cells stably expressing fluorescent histone 2b. Condensation was measured at three different scales: Large-scale (~800 nm), where the chromatin volume was measured by high resolution 4D imaging; medium scale (~200 nm) by statistical analysis of pixel intensities; and molecular scale (~10 nm) by a FRET reporter of histone tail environment. These measurements show that (i) mitotic compaction may start at least 20 min before prometaphase; (ii) it correlates with changes in histone tail conformation; (iii) chromatin density is not highest in metaphase but in late anaphase chromosomes.

In the second part, I focused on the novel finding of highest compaction in anaphase. Single chromosome measurements revealed that chromatids compact in anaphase by a mechanism of lengthwise shortening that starts only after segregation of the sister chromatids is complete. This axial shortening was not affected in condensin-depleted cells, and was independent of the poleward pulling motion on kinetochores, but it nevertheless depended on dynamic microtubules. Perturbation of this shortening caused a severe phenotype of multi-lobulated daughter nuclei, strongly suggesting a function in post-mitotic nuclear assembly and architecture. In addition, if anaphase compaction was perturbed in condensin-depleted cells, segregation defects increased 3-fold, suggesting a second role for anaphase compaction as a rescue mechanism for segregation defects.

In the third part, the quantitative compaction assays were used to probe the role of PNUTS, a major protein phosphatase 1 nuclear-targeting subunit, in the regulation of chromatin structure. In live cells depleted of PNUTS by RNAi, compaction was slowed at least 3-fold. Our collaborators in the group of Philippe Collas at the University of Oslo had shown that PNUTS accelerates chromatin decompaction *in vitro*. PNUTS is thus involved in mitotic chromatin structure *in vivo* and *in vitro*, and my findings make it an interesting target for future research to understand the molecular mechanism of chromosome compaction.

VI Publications

Parts of this thesis are included in the following publications and manuscripts:

Mora-Bermúdez, F; Ellenberg J. Measuring Structural Dynamics of Chromosomes in Living Cells by Fluorescence Microscopy. *(In preparation).*

Mora-Bermúdez, F; Gerlich, D; Ellenberg J. Maximal chromosome compaction occurs by axial shortening in anaphase and depends on dynamic microtubules. *(In preparation).*

Harder, N; **Mora-Bermúdez, F**; Godinez Navarro, W; Ellenberg, J; Eils, R; Rohr, K. Automated analysis of the mitotic phases of human cells in 3D fluorescence microscopy image sequences. *(Submitted).*

Beaudouin, J.; **Mora-Bermudez, F**.; Klee, T.; Daigle, N.; Ellenberg, J. Dissecting the contribution of diffusion and interactions to the mobility of nuclear proteins. *Biophys J.* 2006 Mar 15;90(6):1878-94.

VII Introduction

VII. 1 Chromatin

VII. 1.1 Chromatin as information carrier

The genetic information essential to all life is coded as linear combinations of the nucleotides that form the DNA polymer. However, the DNA double helix does most likely not exist as a linear free molecule in living organisms. Instead, DNA is naturally organized in a complex, multi-scale macromolecular assembly called chromatin. Chromatin is the physiological carrier of not only the genetic but also the epigenetic information in eukaryotes. In the nucleus of an intact cell, the structure and composition of chromatin are dynamic and essential for genomic activities (reviewed in van Holde, 1988; Wolffe, 1998).

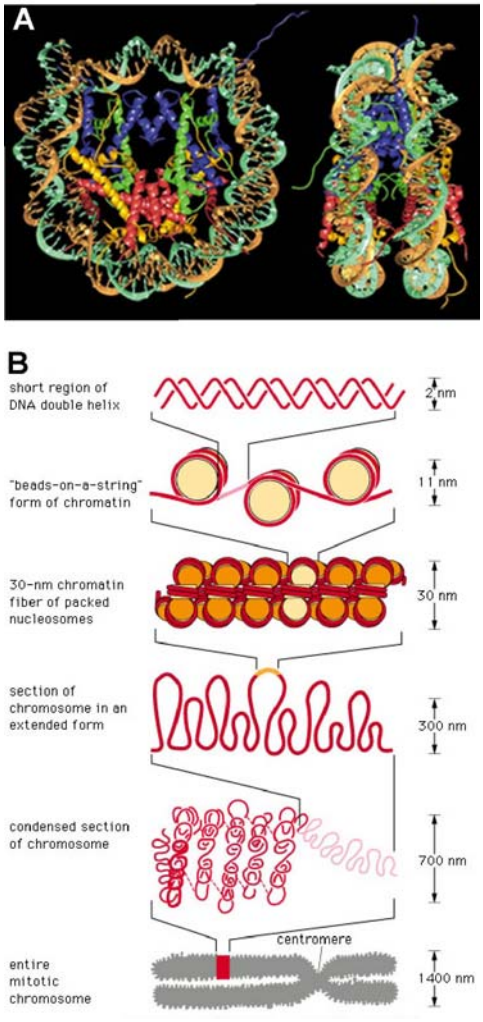

Figure 1. From DNA to chromosomes: chromatin packing. (A) Crystal structure of the core nucleosome particle with 146-bp of DNA as ribbon traces (brown and turquoise) and the eight canonical histone folds (blue: H3; green: H4; yellow: H2A; red: H2B). Parts of some histone tails are represented as unstructured protrusions. The views are down the DNA helix axis (left) and perpendicular to it (right) particle (from Luger et al., 1997). **(B)** Possible levels of DNA packing from the 2nm wide DNA double-helix to the µm-thick double chromosomes. Detailed *in vitro* structural information exists about the DNA double-helix, the 11 nm "beads on a string" nucleosome array and, to some extent, about the "30 nm" fiber. Higher orders of folding leading to entire mitotic chromosomes are hypothetical (from Alberts et al., 2002).

VII. 1.2 Functional states of chromatin

Chromatin in the interphase nucleus has historically been classified in two general functional states, depending on how intensely they are stained with DNA dyes: Heterochromatin and Euchromatin. This classification is likely to have functional validity, as the intensity of staining relates to the density of chromatin, and such density is thought to be inversely proportional to the level of gene expression (Wolffe, 1998). Interestingly, heterochromatin and euchromatin may be differentially and dynamically established in a process that involves interplays between competing repressor complexes and activators of transcription (reviewed in Elgin, 1996).

Heterochromatin was first defined as the fraction of chromatin that remains condensed after mitosis, when the cell is in interphase (Heitz, 1928). It has been described as high-density chromatin that is rich in repetitive elements and non-coding regions, and further classified in: 1) Constitutive heterochromatin, which contains centromeres and telomeres, essential for chromosome function in mitosis and nuclear architecture in interphase; and 2) Facultative heterochromatin, which is important for the global and local regulation of gene expression, for instance during differentiation and dosage compensation. **Euchromatin**, on the other hand, has been described as low density, relatively decompacted chromatin, that includes mostly active regions rich in genes and regulatory sequences (reviewed in Grewal and Elgin, 2002).

Epigenetic marks, such as covalent histone and DNA modifications, do not change the genetic information *per se*, as the types of nucleotide are not modified (reviewed in Richards, 2006). However, these changes do modify the way chromatin is sensed by nuclear factors. The importance of these epigenetic tags has been well established by the analysis of how combinations such modifications can decisively determine if a region is more hetero- or more euchromatic, and therefore what the levels of transcription and other activities may be (reviewed in Richards and Elgin, 2002). Recent studies have nevertheless shown that, instead of two discrete chromatin types, a whole spectrum of intermediate states probably exists in the functional interphase nucleus of an intact cell. Along this line, a direct relation between total gene expression levels and the compaction level of chromatin in interphase is not clear, as heterochromatin regions also have degrees of transcriptional activity, involved for instance in the RNA interference (RNAi) gene expression regulation process (Huisinga et al., 2006; Wassenegger, 2005).

VII. 1.3 Basal chromatin composition

VII. 1.3 i The chromatin fiber

The chromatin fiber is itself composed mainly of chromosomal DNA and proteins associated to it by electrostatic interactions. These proteins include core histones (H2A, H2B, H3, and H4), linker histones (H1) and non-histone proteins. Within the chromatin fiber, the nucleosome is thought to be the smallest functional unit. Each nucleosome consists of a core nucleosome plus associated linker histones. Core nucleosomes are in turn formed by approximately 146 base pairs (bp) of DNA tightly wrapped around a core histone octamer, which contains two copies of each core histone (H2A, H2B, H3 and H4). Each histone contains, in turn, a common conserved structural motif, called the histone fold, and an unstructured NH_2-terminal motif called the histone tail. The octamer forms when a dimer of H3 histones associates with a dimer of H4 to form a tetramer that interacts with two H2A-H2B dimmers (fig. 1A) (reviewed in Kornberg and Lorch, 1999; see Luger et al., 1997). Histone variants have also been acknowledged to play diverse roles in chromatin composition and function, for example H2A.X plays a role in DNA repair mechanisms of double-strand breaks (Redon et al., 2002; Rogakou et al., 1998). Also, the H3 variant H3.3 comes into regions of active transcription and replaces the canonical H3, probably after the transcription machinery has displaced it (Henikoff et al., 2004; Janicki et al., 2004). Histone variants are also implicated in mitotic processes, for example the centromeric variant cenH3 replaces H3 in centromeres and is linked to the correct attachment with the mitotic spindle (Blower et al., 2002).

In the "11 nm fiber", a zigzag chain of core nucleosomes joined by linker DNA can be appreciated and represents the typical view of the basal structure of chromatin fibers. In addition, histone H1 can interact with other H1 units and core nucleosomes, and may be involved in keeping them tightly packed together (van Holde, 1988). This packing has been correlated with the formation and organization of higher orders of chromatin structure, such as the "30 nm fiber" (fig. 1 B) (Bednar et al., 1998).

VII. 1.3 ii Histones as the main DNA organizers

The biochemical nature of the histones sheds light into the functions they have in chromatin. Histones are basic proteins, with a high content of arginine and lysine amino acid (aa) residues. These basic residues, charged positively at neutral pH, are able to closely associate with negatively charged phosphates in the DNA backbone. 1.7 turns of the DNA double helix are thus "wrapped" around histone octamers (fig. 1 A). This contact is mostly electrostatic in nature, but

may also involve some hydrogen bonding with the same phosphates and non-polar contacts with the deoxyribose groups (Luger et al., 1997; Luger and Richmond, 1998a; Luger and Richmond, 1998b). Also, these basic residues and other abundant residues in histones such as serines and threonines, can be covalently modified after translation. Methylation of lysine 9 in H3, for example, has been shown to be a specific binding site of the chromodomain protein HP1 (Bannister et al., 2001; Lachner et al., 2001) which, together with other factors such as small RNAs, may in turn mediates heterochromatin establishment and organization in interphase (reviewed in Grewal and Rice, 2004). Histone lysine methylation has also been tightly linked with gene expression regulation (Lachner et al., 2003) and differentiation in development (Tachibana et al., 2002). Intriguingly, phosphorylation of H3 may also play a role in the structural dynamics of mitotic chromatin. In particular, the phosphorylation of serine residues in H3 by aurora B kinases is a hallmark of compacted mitotic chromatin in a variety of organisms, and has been linked to chromosome compaction in *Drosophila* (Giet and Glover, 2001), the fission yeast (Mellone et al., 2003) and *Tetrahymena*. (Wei et al., 1999). However, no such evidence has been found in the budding yeast (Mellone et al., 2003) or in human cells (Hauf et al., 2003), and the mechanism by which this modification may participate in the organization of mitotic chromatin remains unknown (Prigent and Dimitrov, 2003). In this context, recent studies show that this modification releases HP1 from its H3 binding site in chromosomes during mitosis (Fischle et al., 2005; Hirota et al., 2005), although a potential relation with mitotic progression is not clear.

The numerous possibilities for histones modification, together with the dynamic interchange between canonical and variant histones, and the modifications of DNA through cytosine methylation in CpG duplets, constitute the exuberant epigenetic repertoire of the cell (Richards, 2006). This offers a virtually endless number of possible combinations for the regulation and inheritance of chromatin activity and organization. Such diverse mechanisms have not only been widely implicated in basal genomic activity and gene expression (Shilatifard, 2006), but also in more specific processes such as memory and learning (Levenson and Sweatt, 2005), and in malignancies like cancer (Lund and van Lohuizen, 2004) and abnormal hematopoiesis (Galm et al., 2006).

VII. 2 Chromosome Properties

VII. 2.1 Nucleosome arrays

The "30 nm fiber" is most likely the first level of higher order chromatin folding (see Bednar et al., 1995; Bednar et al., 1998). How nucleosome arrays form this fiber remains controversial. A model where nucleosomes are arranged within a "zigzag" stack upon each other was proposed after electron microscopy studies of chromatin arrays *in vitro* (Woodcock et al., 1993). This arrangement has received support from several approaches and is becoming the most favored view of how nucleosomes are organized. Electron tomography on fixed cells has, for example, shown structures compatible mostly with this model (Horowitz et al., 1994). Also, in live cells, the size and distribution of chromatin fragments generated by ionizing radiation matched simulation results based on it (Rydberg et al., 1998). Recently, crystallography observations at near-atomic scale have directly shown nucleosomes stacked in a two-start zigzag helical arrangement (Schalch et al., 2005).

VII. 2.2 Higher orders of chromosome structure

How nucleosome arrays are organized into higher order folds of chromatin within chromosomes remains controversial. Conceptual models have been put forward to explain chromosome formation and compaction, based mainly on observations of fixed cells and isolated chromosomes.

Protein scaffold?

In a model that relies on extraction methods to remove protein components of chromosomes in vitro, radially arranged loops of 30 nm chromatin fibers are proposed to be organized by central protein "scaffolds". Such scaffolds would act as the backbone of each "supra 30 nm" fiber, which would in turn stack into progressively thicker fibers and eventually chromosomes (fig. 2, left) (Marsden and Laemmli, 1979; Paulson and Laemmli, 1977). The two proposed main components of such a scaffold are important regulators of chromatin organization: topoisomerase II (Earnshaw and Heck, 1985; Gasser et al., 1986; Lewis and Laemmli, 1982) and condensin (Hirano and Mitchison, 1994; Saitoh et al., 1994). Importantly, topoisomerase II was later shown to be present in prophase chromatin, whereas condensin I could only be found later, in metaphase. This led to the refining of the model into a two-step mode of assembly, reflecting the sequential enrichment of both factors (Maeshima and Laemmli, 2003). This refined model has, however, recently been challenged by experiments showing significant folding of large scale fibers before

the appearance of a defined axis of either of these presumed main scaffold components (Kireeva et al., 2004). In addition, topoisomerase II has been shown to have a dynamic interaction with metaphase chromosomes, which is inconsistent with a static role in a proteinaceous backbone (Christensen et al., 2002).

Hierarchical folding?

An alternative view, not relying on proteinaceous chromosome "backbones", and based on methods aimed at preserving the sensitive native structure and composition of chromosomes, proposes that successive folds of progressively thicker fibers may be hierarchically arranged into chromosomes (fig. 2, right) (Agard and Sedat, 1983; Belmont et al., 1987; Sedat and Manuelidis, 1978). The main approach has been to compare light and electron microscopy observations to correlate the dimensions of different chromatin fibers in fixed cells, during different stages of the cell cycle, but also in live cells (Belmont et al., 1989). One additional intriguing approach has been to observe the compaction of engineered DNA sequences inserted in chromosomes (Dietzel and Belmont, 2001; Strukov et al., 2003), which has in turn given support to a refined "chromonema" model of hierarchical folding (Belmont and Bruce, 1994; Kireeva et al., 2004). However, the labeling of defined segments in native chromosome to follow their live structural dynamics remains a challenge. Collectively, these studies nevertheless suggest that the shape and thickness of the fibers observed in fixed and live cells is similar. This has revealed a discrete set of fiber widths, such as the ~100 and ~250nm fibers, which may be functional intermediates between a nucleosome array and a chromosome (Belmont and Bruce, 1994, Strukov et al, 2003). It seems therefore likely that a progressive thickening of chromatin fibers eventually forms chromosomes, and measurements of native chromosome elasticity in cells have supported this view (Houchmandzadeh et al., 1997).

Chromatin network?

However, direct and quantitative correlations between the structures observed in fixed- and live-cell experiments remain a technical challenge, and the structural differences below the resolution of conventional live-cell imaging are yet to be accurately detected and correlated. Also, other experiments on the mechanics of isolated chromosomes have questioned the existence of both a protein scaffold and a hierarchical structure, proposing instead a chromatin network model with regular links between neighboring thin chromatin fibers (Poirier and Marko, 2002).

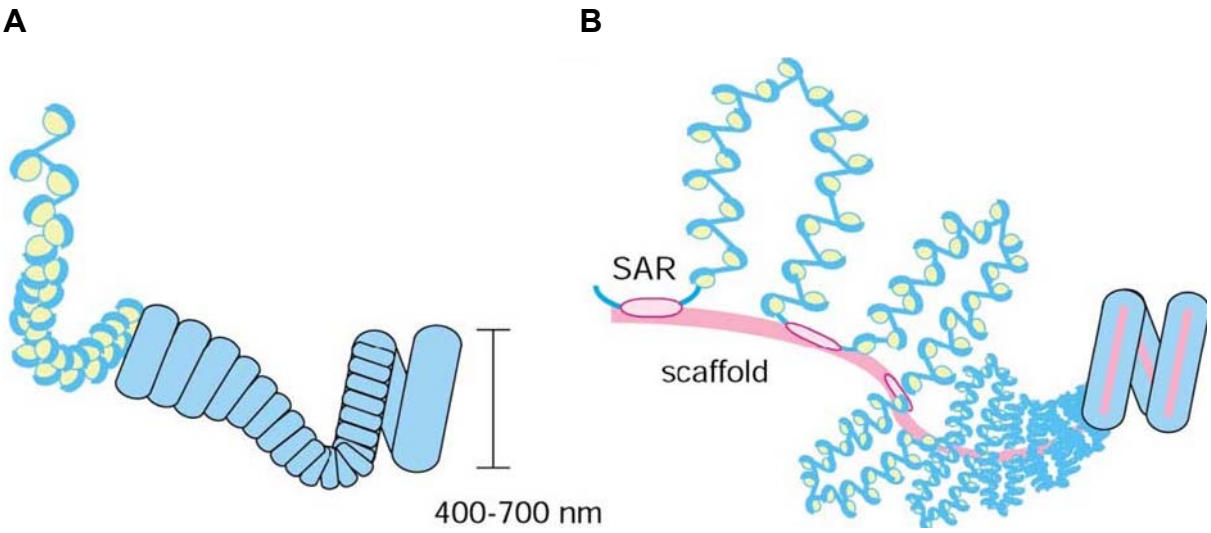

Figure 2. Schematic drawing of the two main conceptual models for mitotic Chromosome Organization. (A) Hierarchical folding. Higher-order chromatin fibers could be created by thinner chromatin fibers progressively folding and coiling into larger structures, possibly based on protein-protein and protein-DNA interactions between neighboring chromatin fibers. **(B) Scaffold.** A proteinaceous chromosome scaffold (magenta) could associate to *cis*-acting DNA "scaffold associated regions" (pink ovals) to fold chromatin fibers into loops (from Swedlow and Hirano, 2003).

VII. 2.3 Chromosome mechanics

The deformability and elasticity of extracted and reconstituted chromosomes has been studied by force extensions with micropipettes under transmission microscopy observation (Almagro et al., 2004; Claussen et al., 1994; Houchmandzadeh and Dimitrov, 1999). Interestingly, chromosomes could be extended 10-fold and still regain their original length (Claussen et al., 1994). This elasticity was confirmed for chromosomes inside cells, in a study that provided data consistent with a hierarchical folding of chromosomes and also proposed that their flexibility increased during mitosis (Houchmandzadeh et al., 1997). Fluorescence microscopy was also used to derive mechanical parameters of Drosophila embryo chromosomes, from the analysis of their shape and motion under mitotic forces (Marshall et al., 2001). Chromosomes were followed by interactively tracing their shapes and matching them with the most similar object in the next time point. From this, mechanical parameters were estimated, such as Young's elasticity modulus, which describes the tendency of an object to be deformed along an axis when a force is applied to it. Based on this, the authors conclude that, during the short cell cycle of Drosophila embryos, chromosomes are less rigid than in slower cycling systems, such as vertebrate cultured cells, and speculate that this could be the consequence of compacting chromosomes less, to allow for rapid rounds of division (Marshall et al., 2001).

VII. 3 The Chromatin Cycle

The ultimate level of high-order chromatin organization is the set of compact mitotic chromosomes that form during prophase, which were first described over 125 years ago by Walther Flemming (1879). Since then, studies mostly carried out in yeast, *Drosophila* and vertebrates have combined to show that chromatin is faithfully replicated and sister chromatids remain together until mitotic chromosomes have formed and can carry the genome between generations.

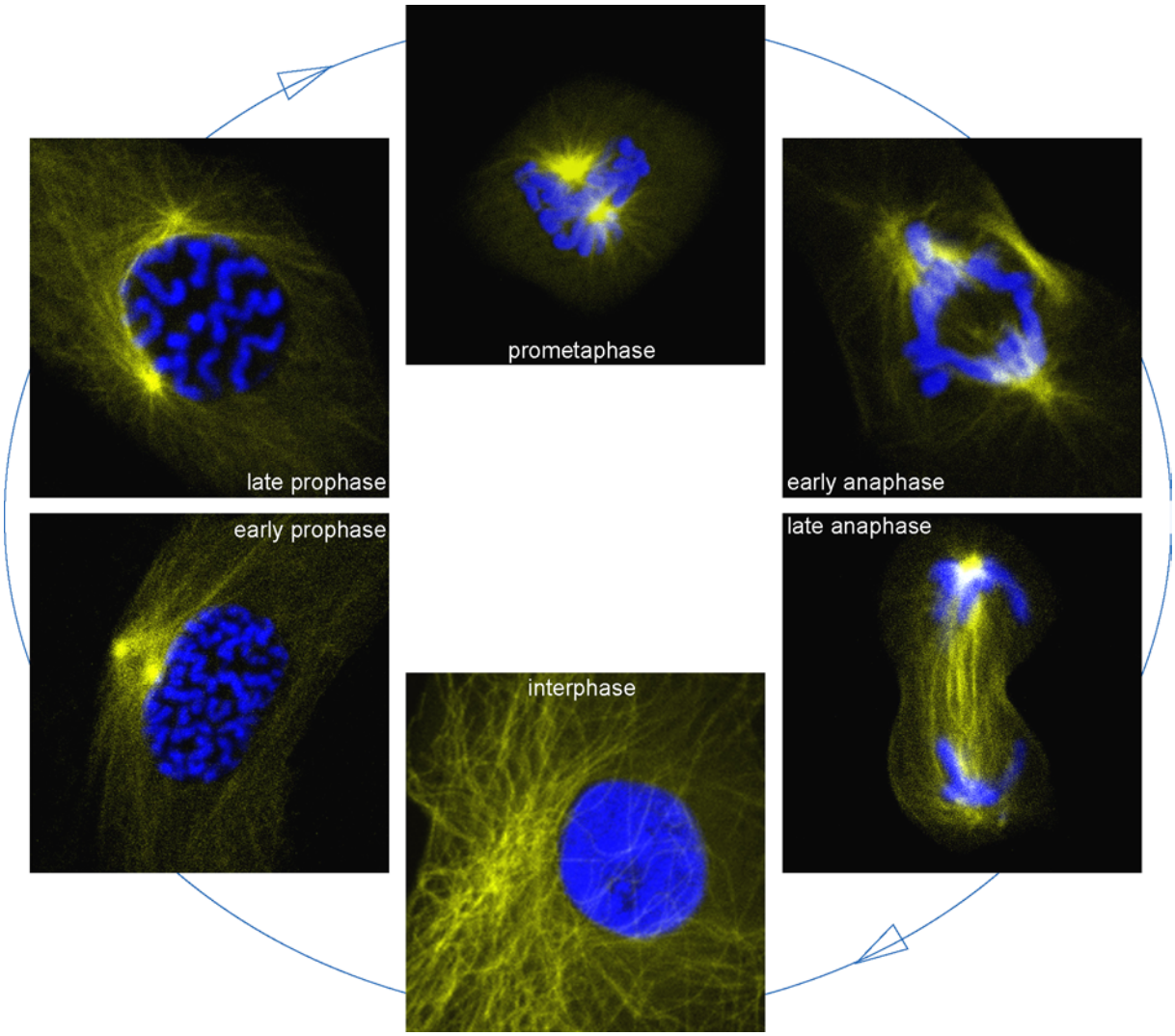

Figure 3. Confocal sections of selected cell-cycle phases in live PTK$_2$ cells stably expressing YFP-α-tubulin (yellow) and DNA counter-stained with Hoechst (blue). Interphase chromatin resolves and compacts into individual chromosomes during prophase. Chromosomes are congressed to the equatorial plane of the cell by microtubules during prometaphase. Sister chromatids are segregated during early anaphase and directed to the newly-forming daughter cells during late anaphase by the mitotic spindle.

VII. 3.1 Cohesins link genome replication and segregation

Karyokinesis, or the division of the nucleus during mitosis, is tightly linked to the "S" or synthesis phase of the cell cycle, when the DNA in chromatin is replicated once and only once (Machida et al., 2005). The main molecular link between the replication and division of the genome is a protein complex called cohesin, formed of combinations of the ATP-binding SMC subunits and kleisin subunits. This combination is also notably found in the condensin complexes, also involved in mitotic chromatin organization (reviewed in Nasmyth and Haering, 2005). Before and during replication, cohesin molecules associate with both the template and the newly crafted fiber of DNA (Guacci et al., 1997; Michaelis et al., 1997). In this way, the two independent macromolecules of identical DNA are then organized as two distinct chromatids, but nevertheless kept in close physical association until they are segregated in anaphase. The structural details of how cohesin manages to keep the template and new chromatid as a pair are yet to be fully uncovered (Gruber et al., 2003; Ivanov and Nasmyth, 2005). During interphase, these dual chromatids are relatively uncompacted and so occupy large volumes referred to as chromosome territories. These territories do not seem to significantly mix with each other, yet they interdigitate in three dimensions (Cremer and Cremer, 2001) and thus collectively render the impression of a single diffuse mass of chromatin.

VII. 3.2 Dual chromosomes must compact, resolve and attach before segregation

VII. 3.2 i Intra- and inter-chromosome cohesion

At the beginning of mitosis, all chromatin undergoes a progressive transformation process where the diffuse sister chromatids condense and resolve into rod-shaped dual chromosomes (reviewed in Swedlow and Hirano, 2003). This reorganization is critical for a precisely equal partitioning of replicated chromosomes to daughter cells and hence for the faithful transmission of the genome (Tanaka et al., 2000). Otherwise, segregation defects, with pathologic consequences such as aneuploidy and cancer, are likely to arise (Nasmyth, 2002)

However, before the cell undergoes karyokinesis, a rigorously choreographed sequence of events ensures that each daughter cell will receive an equal set of chromosomes. Therefore, the cohesin-mediated association between sister chromatids must remain until the cell is ready to make the partition (Nasmyth, 2002). The protein securin goes some way in protecting this association until the cell is ready, as it inhibits the action of separase, the enzyme charged with severing the link

between cohesins and mitotic chromatin during the metaphase-anaphase transition (Hauf et al., 2001; Uhlmann et al., 2000; Wirth et al., 2006).

However, the separase pathway of cohesin removal in anaphase is not the only one. In fact, most cohesin delocalizes from vertebrate chromatin as early as prophase, and yet the cells completes mitosis correctly (Losada et al., 1998; Waizenegger et al., 2000), when separase is not yet active. This early removal is probably mediated by cohesin phosphorylation by the polo-like kinase (Plk), and could involve the Aurora B phosphorylation of histone H3 (Losada et al., 2002; Sumara et al., 2002). After this early removal, some cohesin does remain associated with chromosomes until the metaphase, a sub-population on centromeres (Waizenegger et al., 2000; Warren et al., 2000) and another sub-population distributed along the junction of the two sister chromatid arms (Gimenez-Abian et al., 2004). These sub-populations are those whose removal is normally mediated by separase, but only shortly before the sister chromatids are split. This ensures that no segregation occurs before the anaphase onset. Interestingly, recent evidence shows that the centromere-bound subpopulation of cohesin is probably protected from the phosphorylation-dependent prophase removal by shugoshin, the same protein that prevents premature loss of centromeric cohesion in meiosis I (McGuinness et al., 2005; Salic et al., 2004).

In contrast to the central role cohesins play in keeping sister chromatids together, they seem not to play a role in chromosome compaction. Instead, other SMC-Kleisin complexes, called condensins, have been widely linked to mitotic chromosome compaction, although the role they play is yet to be defined with precision(Hirano, 2002). Interestingly, *in vitro* DNA supercoiling is regulated by what could be a cooperative interplay between condensins and topoisomerases (Kimura and Hirano, 1997; Kimura et al., 1999; Stray and Lindsley, 2003). These results have suggested an interesting hypothesis: analogous to what cohesins do with sister chromatids, condensins may organize and lock fibers that are brought together during the compaction within single chromosomes (reviewed in Nasmyth and Haering, 2005). The progressive establishment of such selective "intra-chromatid cohesions" could be responsible for the disentanglement and mechanical stability that chromosomes need in order to resolve and resist the forces they are subjected to during anaphase segregation (Bhat et al., 1996; Gerlich et al., 2006). Thus, it is possible that condensin complexes may act as intra-chromatid cohesins.

VII. 3.2 ii Chromosome k-fiber attachment

At the time when dual chromosomes are reaching a high level of compaction, the nuclear envelope is being disassembled (Beaudouin et al., 2002). In this way the microtubules of the mitotic spindle gain access to the chromosomes. In parallel, an interface called the kinetochore

has assembled around each chromosome centromere (Fukagawa, 2004). By establishing links mostly with this proteinaceous interface of the centromeres, microtubule "kinetochore" (k)-fibers are assembled, which can then congress all chromosomes toward the equatorial plane of the mitotic cell, in a process that may also involve interactions with the chromosome arms (Khodjakov et al., 1999; Rieder and Salmon, 1994). In this plane, chromosomes prepare for segregation by lining-up into a metaphase plate, established and maintained through a dynamic interplay of "push-and-pull" forces between opposing microtubules. It is at this point that the importance of the remaining sub-populations of cohesin becomes evident. These forces would readily split the sister chromatids prematurely, were it not for the tension that cohesins oppose to the K-fiber pulling. In this way, sister chromatid arms are kept together until all dual chromosomes are correctly attached (Tanaka et al., 2000).

During the congression and alignment process, it is systematically ensured that each of the paired kinetochores is captured by a k-fiber emanating from a different pole. Only such a bipolar and amphitelic attachment guarantees that each daughter cell receives one, and only one, copy of each chromosome (refs). For this, incomplete and incorrect attachments are dissolved in an interplay between the mitotic kinase Aurora B, cdc20 and components of the kinetochore and the "spindle checkpoint", which delays the onset of anaphase by inhibiting the anaphase promoting complex (APC) (Rieder et al., 1994). When all kinetochore pairs are correctly attached, the checkpoint is satisfied and the APC free to degrade securin and cyclin B. The now free Separase is then able to remove all remaining cohesin from chromosomes, and the sister chromatids are then ready to be segregated and eventually recruited to the daughter cells (Nasmyth, 2005; Zachariae and Nasmyth, 1999). After this, the tension between the twin kinetochores no longer exists and the chromosomes are split and directed to the newly forming daughter cells by the mitotic spindle (reviewed in Swedlow and Hirano, 2003).

VII. 3.3 How is mitotic chromosome compaction orchestrated?

Many macromolecular players are know to be involved in the process of mitotic chromosome formation, such as DNA and histones (van Holde, 1988; Wolffe, 1998), topoisomerase (Earnshaw and Heck, 1985) and the condensin complexes (Hirano and Mitchison, 1994). Among these, the conserved condensin complexes are very abundant in mitotic chromosomes and were proposed as the key compactors, based mainly on their strong *in vitro* effect on mitotic chromosome organization in *Xenopus* egg extracts (Hirano, 2002; Hirano and Mitchison, 1994). At the level of single molecules, this was supported by studies that showed how the ATP-dependent

supercoiling activity of condensins reduces the length of the naked DNA fibers that it binds to, both in pro- and eukaryotes (Case et al., 2004; Strick et al., 2004). However, further analysis of condensin function, and of the phenotypes observed in several eukaryotic models upon condensin perturbation, both *in vitro* and *in vivo,* show that their main role during the compaction process may be to disentangle and mechanically stabilize compacting chromosomes, rather than to mediate the compaction itself (Bhat et al., 1996; Gerlich et al., 2006; Hagstrom et al., 2002). Thus, the major biochemical activities directly responsible for mediating the compaction observed *in vivo* most likely remain to be identified.

Along this line, another important aspect is the regulation of electrostatic charges within chromatin and how this relates to the folding of its fibers. This control of charges very likely plays a central role in the conformational dynamics of chromosomes, and it has been shown that ionic forces can in principle provide all the free energy of folding required to form higher order fibers (Clark and Kimura, 1990). However, the precise orchestration between the mostly anionic forces in DNA and the cationic forces in mono- and polyvalent ions, polyamines, core histone tails, linker histones and other charged macromolecules is yet to be understood (reviewed in Hansen, 2002).

VII. 4 The study of Chromosome Compaction

The study of chromosome formation and organization presents a challenge to researchers. Chromatin is highly complex, dynamic and sensitive to environmental conditions, and each of these traits underscores its functional importance for cellular processes, but also complicates its study.

The multi-scale nature of chromatin structure represents a formidable challenge for structural biologists (reviewed in Luger and Hansen, 2005). The complexity of its composition has made it difficult for biochemists and geneticists to comprehensively characterize all the components and interactions that determine how chromatin is organized (reviewed in Belmont et al., 1999). Moreover, despite the rather immobile appearance of chromatin in living cells, recent studies have shown that, with the exception of DNA and core histones, many chromatin components exist in a constant dynamic exchange with the nucleoplasm (Beaudouin et al., 2006; Phair et al., 2004).

Thus, the perturbations of the physiological environment that are an often necessary part of the protocols used to study chromatin composition and organization are likely to cause enough disruption of the native structure to limit the interpretation of the data obtained. On the other

hand, the study of chromosomes within intact living cells suffers from the limited resolution of the noninvasive methods that can be used, such as light microscopy.

Despite such challenges, quantitative multi-dimensional studies of mitotic chromosomes observed inside live specimens are not new. For example, in live *Drosophila* embryos studied in 4D by microinjecting fluorescent histones, chromatin was shown to be more compacted in metaphase than in prophase or telophase (Swedlow et al., 1993b). Also, telophase de/compaction was shown to be anisometric, with some dense peripherally-located foci possibly serving as nucleators of de/compaction for more internally located and less dense chromatin (Hiraoka et al., 1989). The emergence of new tools for fluorescence microscopy, such as GFP-tagging (Lippincott-Schwartz and Patterson, 2003), has been instrumental in advancing the knowledge on chromosome dynamics in the past decade.

VII. 4.1 Live microscopy to study chromosomes

In this work, light microscopy was used to observe the process of mitotic chromosome formation in living cells. The power of live cell imaging to directly probe biophysical parameters such as chromosome mechanics and structure under physiological conditions is limited. Nevertheless, dimensional properties of chromosomes, such as the length and density are accessible with this technique, and have been the focus of this work. Also, genetically-encoded fluorescent markers, such as GFP, now provide convenient selective fluorescence labeling of virtually any desired protein and have also become the most widely-used tool to highlight chromatin proteins in intact cells (Belmont, 2001).

Deconvolution and confocal microscopy are currently the two main techniques to image tagged molecules with high spatial and temporal resolution. These methods have advantages and disadvantages, yet they are not mutually exclusive and can be combined. On most microscopes using a single objective lens for illumination and detection ("epi-fluorescence" mode) both suffer from anisotropic resolution along the optical axis. Deconvolution microscopy utilizes most of the light captured by the microscope objective by illuminating and capturing the whole imaging field simultaneously ("wide-field" mode), but needs to restore the out-of-focus signal to the position it was emitted from, using computational prediction. These image restoration algorithms are highly sensitive to the point spread function of the objective and scattering caused by the specimen, and must often be obtained for each sample analyzed. Confocal microscopy, by contrast requires no post-processing, as undesired out-of-focus light is simply prevented from reaching the detectors. As a consequence overall light efficiency is typically lower (Jonkman et al., 2003; Swedlow et al.,

2002). This work required optimal live-cell multi-spectral 4D imaging resolution and contrast that needed to be flexibly adjusted during the acquisition process. In addition acute perturbations and labeling, such as drug perfusions and photoactivation were an integral part of my approach. Therefore, laser-scanning confocal microscopy was used (see Gerlich and Ellenberg, 2003).

VII. 4.2 How far can live microscopy go?

VII. 4.2 i The limits of live-cell imaging

Under ideal conditions, conventional light microscopy can reach a resolution of approximately 200 nm, according to Abbe's diffraction limit. In praxis, the resolution power of light microscopy is further limited by a combination of the wavelengths of the incident and detected light, the numerical aperture of the detection optics, the specimen and type of experiment. In addition, a difference between the lateral (xy) and axial (z) resolutions must be considered. This difference is reported by the point spread function (PSF), which describes the 3D distortion of the beam of a point light source detected by an objective lens. In a conventional confocal system, the resulting axial amplitude of the PSF is roughly 3-fold larger than the lateral amplitude. This means that the resolution, and hence the certainty of the observation, is 3-fold worse in z than in xy (reviewed in Jonkman et al., 2003).

In this context, geometric dimensions of chromosomes can and have been studied by light microscopy, albeit within the anisotropic 3D resolution limit of several hundreds of nm imposed by the aforementioned variables. This resolution is low compared to the dimensions of the chromatin fiber intermediates between 11-250 nm. Improving spatial resolution of live cell imaging therefore remains a major challenge. However, as a noninvasive technique, live cell imaging has the key advantage to couple structural and dynamic information. Importantly, the dynamic information is only useful if observations are made without significantly perturbing cell physiology. This assumption needs to be validated for each experiment, as fluorescence labeling and the illumination radiation used in high resolution imaging can potentially harm the cell.

Minimizing labeling and illumination below toxic levels typically result in suboptimal spatial and temporal resolution of live cell images. In addition, the structural changes that underlie chromosome reorganization occur naturally in three dimensions over time *in vivo*. Therefore, 4D data has to be acquired, massively increasing the number of images needed to quantitatively capture and characterize chromosome dynamics (fig. 4). High resolution 4D live-cell imaging of entire cell cycles is thus needed to understand the dynamics of chromosome folding, but has to be achieved without significantly altering the physiology of the cellular process under observation.

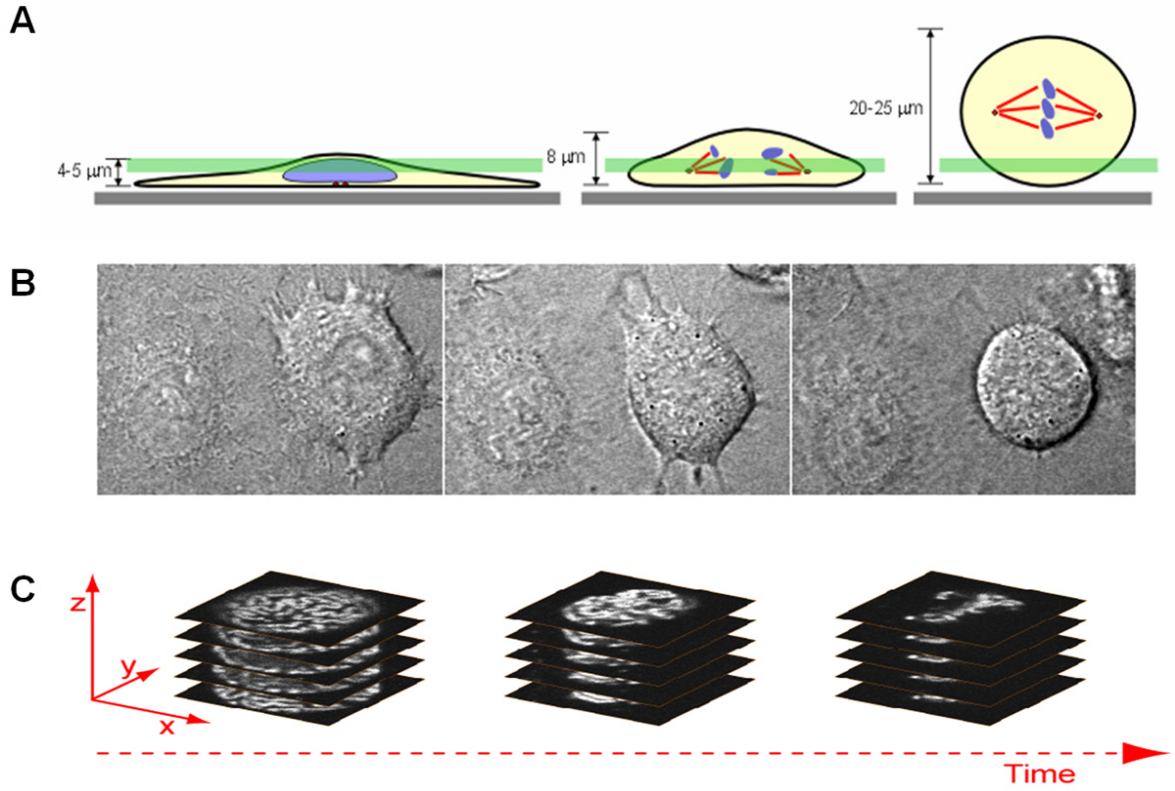

Figure 4. Imaging in 4D is required to capture all chromatin during mitosis.(A) Schematic, representation of the dramatic transformations undergone by a monolayer cell through mitosis. 1st image: cell and its nucleus lying flat during interphase, with the chromatin (blue) decompacted. 2nd image: in early mitosis, the cell starts to detach from the substrate, round-up and elevate as chromosomes condense and congress to the metaphase plate. In metaphase (3rd image), the cell is round and has detached and elevated almost completely from the substrate. If the imaging plane (green band) stays at the level of the interphase, the chromosomes are missed (drawings by P. Lénárt). **(B)** Transmitted light sequence of a mitotic cell (right side of each image) as it detaches, elevates and rounds-up; compare to the flat interphase cell (left side). **(C)** To record all chromosomes, a serial acquisition of fluorescence images along the Z-axis over time is needed (C adapted from Gerlich and Ellenberg, 2003).

VII. 4.2 ii Phototoxic damage, paradoxically useful for mitosis imaging

Photobleaching of fluorescence dyes during intense or prolonged imaging experiments is a common problem in live cell imaging, as it limits the time signal can be detected over background. However, the damage to live cells caused by excessive illumination, called phototoxicity, can be an even more severe problem and create artifacts and experiment failures (Khodjakov and Rieder, 2006; Zink et al., 2003).

Minimizing phototoxicity in live-cell mitotic experiments can be as important for cell viability as the use of appropriate cell culture environment on the microscope. This is because cells undergoing mitosis are particularly sensitive to excessive illumination and often react dramatically to it. The initial mitotic stages, such as the G2/M transition, may be the most sensitive and the

very act of observing chromosomes in early mitosis can prevent the cell from dividing (Mikhailov et al., 2002). Phototoxicity-induced damage can produce cytoskeleton, chromatin and other cellular damages, and chromosome compaction, congression and segregation defects, which readily trigger the activation of mitotic check-points. This can lead to a pause or a full stop of mitotic progression, to a return to a G2-like state and, in extreme cases, to apoptosis (reviewed in Khodjakov and Rieder, 2006). Equivalent damage during interphase may go largely undetected, since no major morphological reorganizations put the cell capabilities to the test.

This apparent disadvantage can paradoxically also be viewed as an advantage over interphase imaging: mitotic cells efficiently and rapidly raise "red flags" if illuminated excessively, and a normally dividing cell provides a good internal control for appropriate imaging conditions.

VII. 4.3 Measures of chromosome compaction

VII. 4.3 i The measurement of chromosome axis reveals aspects of chromosome organization

Axial measurements of chromosomes, i.e. of their width and length, offer an intuitive first assessment of chromosome compaction. Certain specific chromosomes can be identified reliably just based on axial measures with a general chromatin marker. In the budding yeast for example, the length of the particularly large chromosome VII has been extensively measured during anaphase, leading to the discovery of a Cdc14- and condensin-dependent chromatid resolution and axial shortening involved in the segregation of rDNA clusters (D'Amours et al., 2004). Aurora B phosphorylation of condensins was also shown to play a role (Lavoie et al., 2004; Sullivan et al., 2004), and, interestingly, this shortening proceeded in the absence of microtubules (Machin et al., 2005), suggesting chromosome-intrinsic segregation forces that could complement poleward pulling by the mitotic spindle. The chromosome VII pair of sister chromatids could be easily identified because it remains attached long after all others segregated.

However, the more chromosomes in a karyotype, the harder it becomes to accurately identify and follow single chromosomes through mitosis. For example, during prophase of adherent mammalian cells, chromosomes can be visualized separately as they individualize. In HeLa cells, recent width measurements combined with intensity analysis were used to show that no significant compaction occurs from prophase to prometaphase, even upon binding of condensin I to single chromosomes (Gerlich et al., 2006). This suggests that condensin I does not directly compact chromosomes. After prophase the cell undergoes dramatic morphological changes and

the proximity between chromosomes increases, making the tracking and length measurements very challenging, even when thin confocal or deconvolution sectioning is employed.

VII. 4.3 ii Chromosome volume and density

The terms condensation and compaction are widely used to describe the density state of chromatin. Usually, these descriptions are based on visual inspection and qualitative assessment of microscopy images. However, the compaction of chromatin, or of any other type of matter, can only be demonstrated by an increase in density. For this a quantitative analysis is necessary. This is illustrated by a study that found no difference between the volumes, and therefore the condensation states, of the active and inactive X chromosomes in fixed mammalian cells, despite having different 3D shapes (Eils et al., 1996). Thus, measuring a decrease in one or more axial dimensions of a chromosome, such as the length or width, can be a good indication that compaction has occurred, but this must nevertheless be complemented by a density or volume measurement before compaction is demonstrated beyond doubt.

One approach is to quantitate changes in the fluorescence intensity signal of chromatin regions. This was analyzed in live Drosophila embryos with chromosomes labeled with microinjected fluorescently labeled purified histones. In selected mitotic phases, mean fluorescence intensities were calculated by interactively selecting pixels inside chromatin regions in 4D sequences. Chromosomes were found to have a higher fluorescence concentration in metaphase than in prophase or telophase. Unfortunately, focal drift and cell movement hindered automated quantitations and the characterization of the condensation kinetics during the entire mitosis (Swedlow et al., 1993b).

Two studies of intact mammalian cells expressing fluorescent histones have estimated chromosome compaction changes during crucial mitotic transitions (Beaudouin et al., 2002; Manders et al., 2003). In one study, a full kinetic read-out of chromatin density from prophase until metaphase showed that compaction increases during prometaphase (Beaudouin et al., 2002). For this, the fluorescence intensity distribution of all pixels was analyzed in maximum intensity projections of 4D sequences from prophase to metaphase (Beaudouin et al., 2002). Nevertheless, the projection along the optical axis of 3D data sets can result in the loss of spatial information about local fluorescence intensities and overlaps. Along this line, the width of individual prometaphase chromosome has been shown to change little (Gerlich et al., 2006). Together, this suggests that the increased density observed during congression in projected images may be caused by compression of the chromosomes against each other rather than by compaction of individual chromosomes. At the end of mitosis, an analysis in single optical sections of the local fluorescence intensity distributions proposed that all chromatin decompacts first isometrically,

and then different regions showed different decompaction rates (Manders et al., 2003). Here also, the high proximity and overlap between chromosomes obscured the distinction between intra- and inter-chromosomal compaction.
In sum, while the de/compaction of chromatin in selected mitotic phases has been characterized, the quantitative analysis of all chromatin during entire mitosis has remained an unsolved challenge.

VII. 5 Motivation and Aims of this Project

Numerous studies have investigated the changes that underlie the transformation of interphase chromatin into rod-shaped mitotic chromosomes. A current line of research has for instance shown that chromosomes form by a progressive thickening of chromatin fibers. Despite such extensive study, the nature and orchestration of these changes remains to be understood. Beyond the comparison of dimensions in selected moments of the cell cycle, little is known on how or by how much these fibers are folded and dynamically regulated during the cell cycle *in vivo*.
Furthermore, with the exception of the rDNA case in yeast, most compaction studies have focused on prophase and prometaphase, when sister chromatid resolution and kinetochore assembly allows bipolar attachment of chromosomes to the mitotic spindle. Ultimately however, it is during anaphase that the importance of whole chromosome compaction becomes most evident. Compact and resolved chromosomes are easier to segregate and distribute to daughter cells. Having shorter chromosomes also reduces the risk of missegregation or damage when the cytokinetic furrow splits the cell (Swedlow and Hirano, 2003). This could be especially important in organisms with several long chromosomes, such as mammals. Therefore, more quantitative studies on the formation of mitotic chromosomes are needed. Specifically, a characterization of chromosome compaction throughout mitosis is missing. The compaction state of chromosomes during the critical segregation period in anaphase is also of high interest.

VII. 6 Specific Goals of this Project

This work has aimed at developing and applying quantitative assays to measure mitotic chromosome compaction in intact cells based on confocal fluorescence time-lapse microscopy and computerized image processing.

Defining chromosome compaction.

Ideally, a thorough characterization of compaction should start at the atomic level. However, even molecular resolution of chromatin structure has proven elusive, and more so in direct observation in live cells. Thus, a practical definition of chromatin compaction applicable to live cell studies is proposed:

The compaction state of chromatin has changed when the density of chromatin has changed. Therefore, if for example the volume that contains the fluorescent chromatin decreases, the density of the chromatin has increased and compaction, or condensation, has occurred. A reduction in one dimension of a single chromatin fiber, such as the length of a chromatid, is interpreted as compaction only if this change correlates with an increase in the chromatin density.

Assays to measure chromosomes

The specific goal of the first part of this project has been to develop quantitative confocal microscopy assays to measure the compaction of mitotic chromatin from G2 through mitosis in single living cells. Three main assays were thus developed:

In the first assay, 4D imaging is used to quantitate large-scale mitotic condensation. The volume occupied by chromatin, labeled by GFP-tagged core histones stably-expressed at low levels, is measured through mitosis by image segmentation and volume reconstruction to follow changes in condensation.

In the second assay, statistical differences in the distribution of pixel intensities of GFP-histones are analyzed at intermediate resolution. As condensation progresses in prophase, the spatial distribution of chromatin changes and fluorescence heterogeneity in the nucleus increases. This increase in heterogeneity is quantitated by calculating the standard deviation of the mean of all pixel intensities of fluorescent chromatin in the nucleus.

In the third assay, chromatin condensation at the molecular scale was measured with an *in vivo* FRET probe attached to a core histone, sensing the local nucleosome environment by time-lapse ratio imaging.

Collectively, these assays show that prophase chromosome compaction starts at least as early as 20 min before nuclear envelope breakdown, demonstrating that the unregulated access of cytoplasmic factors is not required for compaction.

Applications of the assays to chromosome biology

Unexpectedly, the volume occupied by chromatin during mitosis did not reach the minimum in metaphase. Instead, an additional compaction step occurred at the end of anaphase, between segregation and telophase decompaction. To characterize this novel anaphase compaction,

further assays were developed to measure the changes in length of individual chromosome arms during anaphase and to probe the requirements for this compaction pharmacologically.

These assays show that this novel anaphase compaction step occurs by a mechanism of progressive axial shortening of chromosome arms from telomere to centromere. This shortening progressed independently of the poleward motion of chromosomes produced by the pulling of the mitotic spindle at the kinetochore, but nevertheless depended on intact and dynamic microtubules. Acute perturbation of anaphase compaction by microtubule depolymerizing or stabilizing drugs caused a phenotype of multilobulated nuclei in daughter cells. Furthermore anaphase shortening was sensitive to acute treatment with the Aurora kinase inhibitor hesperadin, but proceeded normally in cells depleted of both condensin complexes by RNA interference. Segregation defects in condensin-depleted cells that are normally overcome in late anaphase failed to be rescued in cells were anaphase shortening was acutely perturbed by microtubule poisons. Together, this data suggests that anaphase chromosome arm shortening is a novel mechanism required for postmitotic assembly of normal nuclear architecture and to rescue segregation defects in anaphase, such as chromosome bridges.

Together, the three independent but complementary approaches developed in this project constitute a powerful toolbox to characterize and test the molecular requirements of chromatin compaction in living cells, over a wide range of spatial scales and through the cell cycle. This combination was used to uncover a compaction step in anaphase, potentially required for genome integrity and organization. Also the role of a potential chromatin regulator has started to be characterized. Furthermore, some of these assays are suited to study also other cellular structures, as shown for the fluorescence intensity distribution of the mitotic spindle.

VIII Material and Methods

VIII. 1 Material

VIII. 1.1 Laboratory equipment and reagents

VIII. 1.1 i Equipment

Microscopes	Zeiss LSM 510, Carl Zeiss, Jena Zeiss LSM 510 Meta Carl Zeiss, Jena Zeiss Axiovert 200M, Carl Zeiss Jena Zeiss Axiovert 40M CFL, Carl Zeiss Jena Leica TCS SP2 AOBS, Leica Microsystems, Mannheim.
Computer Hardware	Dell Dimension 8400. Dell Corp. PowerBook G4, Apple Corp.
Computer Software	Acrobat Reader 7.0, Adobe Amira 2.3 (TGS) Analyze-it® 1.7 Statistics Software Axiovision 3.0 and 4.0 (Carl Zeiss) Clone Manager Professional Suite (Sci Ed Central): Clone Manger 6 (6.0) Align Plus 4 (4.1) Primer Designer (4.2) Endnote 9.0 for Mac. (Thomson) Excel 2002, Microsoft Corp. Heurisko 4.0 (Aeon) Illustrator 10.0. Adobe Image J 3.0-3.6 (NIH) LSM 510 software 2.8-3.3 Firefox 1.07 (Mozilla) Photoshop 7.0 Adobe Word 2002, Microsoft Corp.
Incubator Heat-block	Eppendorf Thermomixer 5436
Chambers	EMBL Precision Workshop
Freezers	Liefherr comfort (-20°C) Heraeus HFU-86 450 Ultralow Freezer (-85°C)
Table centrifuges	Eppendorf Centrifuge
Magnetic mixer	Heidolph MR 3001
Microwave	Panasonic
Micro-Pipettes	P10, P20, P200, P1000 Gilson Pipetman
Pipette	Pipetus-Akku, Hirschmann
Milli Q Water System	Millipore® Molsheim, France.
Mini culture rotator	Rollodrum 10-7, New Brunswick Scientific
Reaction Agitator	Heidolph Reax 2000
Rotator of samples	CE, New Brunswick Sci. Inc.
Vacuum centrifuge	Speed-Vac Concentrator, Bachofer
Spectrophotometer	Ultraspect 2100, Pharmacia Biosciences
Thermal cycler	MJ Research Inc. PTC-1000 RoboCycler, Stratagene Gradient 96

Tweezers	Roth, Karlsruhe
Under-table centrifuge	Heraeus Varifuge 3.0R
Vortex	Vorterx-Genie 2, S.I.
Water baths	GFL, Burgwedel

VIII. 1.1 ii Reagents

DNA-from-gel purification kit	GenClean® Spin kit, Q Bio Gene
Filters & Filter paper	0,2 & 0,45 µm, Cellulose ester, Schleicher & Schuell, Dassel
"Fish" magnets	Spinbar, Neolab
Glass pipettes general glassware	Pyrex, Duran
Gloves	Powder-Free Pehasoft, Hartmann; Nitrile N-Dex®, Best
Mini & Midi Kits	Qiafilter®, Qiagen, Hilden
Parafilm	Pechinery, Menashsa, WI
Pasteur Capillary pipettes	WU Mainz
PCR-reaction tubes	Greiner; BD Biosciences
PCR-Purification Kit	Qiagen, Hilden
Petri plates	94 mm x 16 mm ,145 mm x 20 mm Greiner Polypropylene
tubes 15 & 50 ml	Greiner; BD Falcon
Reaction tubes	O,5; 1,5 & 2 ml. Sarstedt, Eppendorf
Syringes	1,0; 5,0; 10,0 & 50,0 ml, B-D
Tissues	KimWipes® Lite 200, Kimberly Clark

VIII. 1.2 Stock chemicals and solutions

Chemicals and media, unless otherwise listed, were of p.A. quality and obtained from the companies Sigma (München), Merck AG (Darmstadt), Roth (Karlsruhe) and Gibco (BRL)

VIII. 1.2 i Gel electrophoresis of nucleic acids

10X TBE-buffer	1M Tris 500 mM Borate 10 mM EDTA
Ethidium bromide	10 mg/ml in 1 x TBE
10X DNA-Sample buffer	1 x TBE 50 % Glycerol 0,25% Orange G

VIII. 1.2 ii Other buffers and solutions

PBS	137 mM NaCl 2.7 mM KCl 1.4 mM KH_2PO_4 4.3 mM Na_2HPO_4/Na_2CO_3 Adjusted to pH 7.4 with Na_2CO_3
Ethanol 70% and 100%	(for DNA precipitation and purification)
Methanol 100 %(	for DNA precipitation and purification)
1X TE	10 mM Tris/HC1, pH 7,5-8,5 1 mM EDTA

VIII. 1.3 Enzymes, markers, antibodies and nucleic acids

DNA molecular weight marker	GeneRuler™ 1kb DNA Ladder, MBI Fermentas
Restriction endonucleases & buffers	New England Biolabs, Frankfurt Roche Biochemicals, Mannheim
T4 DNA ligase & T4 Quick Ligase	(Quick Ligation Kit™) New England Biolabs, Frankfurt
Buffer & dNTP mix	TaKaRa (Buffer with MgCl2+ incl. And dNTP mix at 2,5mM of each dNTP)
PCR kit	Sprint® Advantage, BD Biosciences Clontech

VIII. 1.3 i Oligonucleotides (primers) for sequencing and PCR amplification of new chimera proteins.

Most constructs are core histones tagged with FPs and/or versions of the tetra-cysteine motif (tC) flanked by binding-enhancing aa (Adams et al, 2002). When these primers were used to generate a plasmid, the plasmid was typically named after the primer, e.g. the H2b-EGFP-tC_n2f generated the pH2b-EGFP-tC_n2 plasmid (or the abbreviation FUS-n2 after "fusion" of both donor and acceptor fluorophores to H2b for intra-molecular FRET). n=new optimized tCs (B. Martin & R. Tsien).

Primers for H2b and H3 core histone fusion constructs

A good template for amplification of all H2b fragments is pH2b-EGFP-tC. Template for H3 fragment amplification is pBOS_H3-EGFP (see below). Unless otherwise indicated, H2b primers, and therefore plasmids, contain the restriction contain the BsrGI-ApaI restriction sequences for digestion and vector insertion.

Name	***Sequence in 5'→3'***
H2b-EGFP_f2	CGGAATTCACCGCCACCATGCCAGAGCC
H2b-EGFP_r2	CCAAGTACACCAGCGCTAAGGGAGTGAGCAAGGGCGAGGAGGCTA
tc-H2b_rev	TCCCCCCGGGTTACTTAGCGCTGGTGTACTTGG
tc-H2b_fwd	CGGGGTACCGCCACCATGCGCGAGGCCTGCTGTCCCGGCTGCTGTACCGCGGG CCCGGGACCAGAGCCAGCGAAGTCTGC
tc-H2b_fwd2	CGGGGTACCGCCACCATGCGCGAGGCCTGCTGTCCCGGCTGCTGTACCGCGGG CCCTGGACCAGAGCCAGCGAAGTCTGC
H2b-tC_rev	ATCCCCCCGGGCCAGCGGTACAGCAGCCGGGACAGCAGGCCTCGCGCATCTTAG CGCTGGTGTACTTGG
H2b-tC_fwd	CGGGGTACCGCCACCATGCCAGAGCCAGCGAAGTCTGC
H2b-EGFP-tC_f (also called FUS)	GTACAAGCACCGCTGGTGCTGTCCCGGCTGCTGTAAGACCTTCGGGCCCGGGAT CCACCGGATCTAG
H2b-EGFP-tC_nf1	GTACAAGCACCGCTGGTGCTGTCCCGGCTGCTGTAAGACCTTCCTGGGCCCGGG ATCCACCGGATCTAGATAA
H2b-EGFP-tC_n2f (most used!)	GTACAAGTTCCTGTTCTGCTGTCCCGGCTGCTGTATGGAGCCTCTGGGCCCGGG ATCCACCGGATCTAGATAA
H2b-EGFP-tC_n3f	GTACAGCTTCCTGAACTGCTGTCCCGGCTGCTGTATGGAGCCTGGGGGCC
H2b-EGFP-tC_n3r	CCCAGGCTCCATACAGCAGCCGGGACAGCAGTTCAGGAAGCT
H2b-EGFP-tC_n4f	GTACATCAACGGCAGCTTCCTGAACTGCTGTCCCGGCTGCTGTATGGAGCCTGG GGGCC
H2b-EGFP-tC_n5f	GTACAAGGGCGCCACCCUGGGCAGCTTCCTGAACTGCTGTCCCGGCTGCTGTAT GGAGCCTGGGGGCC
H2b-EGFP-tC_n5r	CCCAGGCTCCATACAGCAGCCGGGACAGCAGTTCAGGAAGCTGCCCAGGGTGG CGCCCTT
H2b-EGFP-tC_n6f	GTACAAGGGCGCCCCTGGAGCTAACGTGACCCTGGGCAGCTTCCTGAACTGCTG TCCCGGCTGCTGTATGGAGCCTGGGGGCC
H2b-EGFP-tC_n6r	CCCAGGCTCCATACAGCAGCCGGGACAGCAGTTCAGGAAGCTGCCCAGGGTCAC GTTAGCTCCAGGGGCGCCCTT
tC-H3_rev	TCCCCCCGGGTTACGCTCTTTCTCCGCGAATGC
tC-H3_fwd	CGGGGTACCGCCACCATGCGCGAGGCCTGCTGTCCCGGCTGCTGTACCGCGGG CCCGGGAGCTCGTACTAAACAGACAGC
tC-H3_fwd2	CGGGGTACCGCCACCATGCGCGAGGCCTGCTGTCCCGGCTGCTGTACCGCGGG CCCTGGAGCTCGTACTAAACAGACAGC

Primers for H4 core histone.
The templeate for all H4 fragment amplifications is pBOS_H4-EGFP (see below). Unless otherwise indicated, tC-H4 and H4-tC primers, and therefore plasmids, contain the KpnI-XmaI restriction sequences for digestion and vector insertion

tc-H4_r1	ACCCTCTACGGTTTCGGTGGGTAACCCGGGGGGA
tc-H4_f1	CGGGGTACCGCCACCATGCGCGAGGCCTGCTGTCCCGGCTGCTGTACCGCGGGCCC GGGATCTGGCCGCGGCAAAGG
tc-H4_fwd2	CGGGGTACCGCCACCATGCGCGAGGCCTGCTGTCCCGGCTGCTGTACCGCGGGCCC TGGATCTGGCCGCGGCAAAGG
tc-H4_fwd3	CGGGGTACCGCCACCATGGCTGCACGCGAGGCCTGCTGTCCCGGCTGCTGTGCTAG AGCATCTGGCCGCGGCAAAGG
tc-H4_fwd4	CGGGGTACCGCCACCATGTCTATTAGAGAAGCTTGCTGTCCCGGCTGCTGTACCGCT GGACCAGGAAGCAAGACCGGATCTGGCCGCGGCAAAGG
tC-H4_fwd5	CGGGGTACCGCCACCATGAGAGAAGCTTGCTGTCCCGGCTGCTGTACCGCTGGACC AGGAAGCAAGACCGGATCTGGCCGCGGCAAAG
tC-H4_fwd6	CGGGGTACCGCCACCATGCACCGCTGGTGCTGTCCCGGCTGCTGTAAG ACCTTCTCTGGCCGCGGCAAAGG
tC-H4_fwd-n1	CGGGGTACCGCCACCATGAAGGACAAGACGACAGGGCCGACGACATACCTCGGCTC TGGCCGCGGCAAAGG
tC-H4_fwd-n2	CGGGGTACCGCCACCATGTTCCTGAACTGCTGTCCCGGCTGCTGTATGGAGCCTGG ATCTGGCCGCGGCAAAGG
tC-H4_fwd-n3	CGGGGTACCGCCACCATGGGAAGCTTCCTGAACTGCTGTCCCGGCTGCTGTATGGA GCCTGGATCTGGCCGCGGCAAAGG
tC-H4_fwd-n4	CGGGGTACCGCCACCATGGGAAGCTTCCTGAACTGCTGTCCCGGCTGCTGTGGATC TGGCCGCGGCAAAGG
tC-H4_fwd-n5	CGGGGTACCGCCACCATGGGAAGCTTCCTGAACTGCTGTCCCGGCTGCTGTTCTGGC CGCGGCAAAGG
tC-H4_fwd-n6	CGGGGTACCGCCACCATGAGAGAAGCTTG
TC-25DNH4_fwd	CGGGGTACCGCCACCATGAGAGAAGCTTGCTGTCCTGGATGCTGTACAGCTGGAAA GCCGGCCATCCGGCG (first 25 aa in H4 N-term missing)
TC-30DNH4_fwd	TCCCCCCGGGTTACCCACCGAAACCGTAGAGG (first 30 aa in H4 N-term missing)
H4-C1_rev	ACGTAGATCTGGCCGCGGCAAAGG
H4-C1_fwd	GGAAGATCTACCGCTGGACCAGGAAGCAAGACCGGATCTGGCCGCGGCAAAGG
H4-C1_f2	TAGGGGTACCTCTGGCCGCGGCAAAGGC
H4-C1_f3	TGATCCCGGGTCCCACCGAAACCGTAGAGG
H4-N1_rev	TCGAAGATCTACCGCCACCATGTCTGGCCGCGGCAAAGG
H4-N1_fwd	TCCCCCCGGGCCAGCGGTACAGCAGCCGGGACAGCAAGCTTCTCTCATCCCACCGAA ACCGTAGAGGG
H4-TC_rev	TCCCCCCGGGCCAGCGGTACAGCATCCAGGACAGCAAGCTTCTCTCATCCCACCGAA ACCGTAGAGG
H4-TC_rev2	TCCCCCCGGGCCAGCGGTACAGCATCCAGGACAGCAAGCTTCTCTCATCCCACCGAA ACCGTAGAGG
H4-TC_fwd	CGGGGTACCGCCACCATGTCTGGCCGCGGCAAAGG

VIII. 1.3 ii Expression plasmids

Unless otherwise indicated, existing and generated plasmids used for DNA transfection into mammalian cells were typically derived by subcloning into:

pEGFP-N1	Clontech
pEGFP-C1	Clontech

VIII. 1.3 iii Modified plasmids used

pH2b-EGFP	Pharmigen
pEGFP -H2b	Inserted H2b from pYFP-H2b into pEGFP-C1 (XhoI-BamHI). -SGLRSRAQASNSAVDGTATM- linker between the two proteins.

pH2B-PAGFP	(Beaudouin et al., 2006).
pH2A-EGFP	Kind gift from Michael Brandeis (cDNA flanked with NcoI-NcoI sites)
pBOS_H3-EGFP	Kind gift from Hiroshi Kimura. Inserted KpnI-XhoI in pBOS MCS (Kimura and Cook, 2001).
pBOS_H4-EGFP	Kind gift from Hiroshi Kimura. Inserted KpnI-XhoI in pBOS MCS (Kimura and Cook, 2001)
pYFP-α-tubulin	replaced the GFP by YFP in the Clontech construct (from P.Keller (Beaudouin et al., 2002)).
pmEGFP-α-tubulin	Inserted α-tubulin from pYFP-α-tubulin into pmEGFP (3 frag. BSRG1, BamH1, ApaL1)
pMeCP2-EGFP	Kind gift from Christina Cardoso (Brero et al., 2005)

For ptC-H2b, pH2b-tC, pH2b-EGFP-tC_n2 (also called FUS), ptC-H3-n*, ptC-H4-n*, pH4-TC-n*, see primers.
For H1, SUV39H1 and Hp1 plasmids, see materials in appendix 3 (Beaudouin et al., 2006).

VIII. 1.3 iv Primary antibodies (IgGs)

α-tubulin alpha	Sigma
α-tubulin, gamma	Sigma
human crest serum (kinetochores)	Kind gift from A. Ladurner

VIII. 1.3 v Secondary antibodies

Alexa Fluor 488	
Goat α-mouse	
Goat α-rabbit	Molecular Probes
Alexa Fluor 546	
Goat α-mouse	Molecular Probes
Cy3	
- Goat α-mouse	
- Goat α-rabbit	
- Goat α-sheep	Amersham Biosciences

VIII. 1.4 Bacteria

VIII. 1.4 i Bacterial strain

E. Coli XL1-Blue®	Sub-clonning grade, Stratagene

Media, buffers and chemicals for bacteria

LB-Medium, pH 7.0	EMBL reagents

Antibiotics were added to the cooled media (final concentration = 100 µg/ml). The stock-solutions for the used antibiotics were as follows:

Ampicillin solution	100 mg/ml in H2O, sterile filtered
Kanamycin solution	100 mg/ml in H2O, sterile filtered

The stock solutions were used at a 1:1000 cc

VIII. 1.4 ii Selection Media

LB-Amp	LB-Medium + 100 μg/ml Ampicillin

VIII. 1.4 iii Selection Plates

LB-Amp	EMBL reagents
LB-Kan	EMBL reagents

VIII. 1.5 Mammalian cells

Maternal wt lines	
HeLa	Human cervix carcinoma, adherent
NRK	Normal Rat Kidney, adherent
PTK2	*Potorous tridactylis* kidney 2, adherent

VIII. 1.5 i Derived lines with stable expression of fluorescent markers

NRK-NIH

pEGFP-H2b	See plasmids and primers sections
pPAEGFP-H2b	(Beaudouin et al., 2006).
pH2B-EGFP-tC	See plasmids and primers sections
pmEGFP-tubulin_alpha	idem
pEGFP-SUV39H1	idem
pEGFP-Hp1β	idem

HeLa (Kyoto)

pH2B-EGFP	(Hirota et al., 2004)

PtK_2

pYFP-α-tubulin	P.Keller (Beaudouin et al., 2002)

VIII. 1.5 ii Buffers, media and chemicals for mammalian cell protocols

All percentages are v/v

Freezing medium	90 % Fetal Calf Serum (FCS 10 % DMSO
DMEM medium	Gibco. Supplemented with: 10% FCS, 2mM glutamine, 100U/ml streptomycin, 100μg/mL penicillin.
MEM medium	Gibco. Supplemented with 10%) FCS, 2mM glutamine, 1mM Sodium pyruvate, 80μg/ml non-essential amino acids, 100U/ml streptomycin, 100μg/ml penicillin.
Imaging medium	Gibco. Pre-warmed at 37°C: CO2-independent medium without phenol red, 20% FCS, 2mM glutamine, 100U/mL streptomycin, 100μg/mL penicillin.
Selection medium	For cell lines transfected with a plasmid with a resistance gene to neomycin, 500ug/mL G418 (GIBCO) was added
Optimem Medium	Gibco. For optimal mix and delivery of transfection and RNAi-depletion preparations
Immunofluorescence medium	PBS; 10% FCS; 0,05% Azide; 0.2% Saponin

Aphidicolin	Sigma
FUGENE6	Roche
Hesperadin	Boehringer Ingelheim (Kind gift from J.M. Peters)
Hoechst 33342	Sigma
Nocodazole	Sigma
ReAsh	Kind gift from A. Schleifenbaum
Taxol	Sigma.

RNA interference reagents

siRNAs	Ambion Europe Ltd.
Oligofectamine	Invitrogen

Small interfering RNAs (siRNAs):

GFP	(Gerlich et al., 2006)
PLK	idem
PNUTS	(Landsverk et al., 2005)
Scrambled (Scr; nonsilencing control):	5'-UUCUCCGAACGUGUCACGUTT-3'
Smc2	5'-UGCUAUCACUGGCUUAAAUTT-3'

VIII. 2 Methods

VIII. 2.1 Molecular biology methods

VIII. 2.1 i Generation of DNA plasmids for fluorescent protein expression in mammalian cell lines

DNA methods in general were performed following standard protocols (Sambrook and Russel, 2001).

In short, DNA concentrations of the plasmids of interest were measured by photometry. Subcloning of DNA sequences for proteins of interest was performed by restriction digestion with specific endonucleases, followed by agarose gel electrophoresis, purification and ligation of the vector and insert DNA fragments of interest. Then, ligated plasmids were amplified in optimized bacteria and analyzed by restriction analysis after miniprep purification. Positive clones were then further amplified in midi-preps. The resulting amplified plasmids were then mostly used for fluorescent protein expression in living mammalian cells. Buffers, enzymes and kits used for these protocols are listed in the materials section.

VIII. 2.1 ii PCR amplification

Plasmids generated by ligating a PCR-amplified fragment to an existing vector fragment were controlled by DNA sequencing performed by the EMBL Genomics Core Facility (GeneCore). See primers sections.

Typical PCR cycles used for amplification were as follows:

Step	Temp. in °C	Duration in min and s.
1)Denaturing	94	30 s-1,5 min
2)Annealing	59-62	1 min-1 min30sec
3)Elongation	72	1-4 min, depending on size of expected fragment (rule of thumb: 2min per kb)
4)End	72	10 min

This was followed by cooling the samples at 4°C until needed.

Each PCR reaction contained: 5,0µl 10X reaction buffer (supplied)
4,0µl 1.25 mM mixed dNTPs (dATP, dGTP, dCTP, dTTP)
1,0-2,0µl of each of the 2 oligo solutions (~50,µM)
0,2µl Taq polymerase.
0,5-6µl of template DNA
and taken to 50,0αl with ddH20

VIII. 2.2 Bioinformatic sequence analysis

DNA and protein sequences were examined with the existing up-to-date non-redundant, annotated databases of the NCBI and EBI with BLAST2 algorithms, trough the respective internet interfaces, at the DNA and protein level. Analysis at the protein level to look for annotated proteins, homologues and putative domains were done with the ENSEMBLE, the PFAM and the Simple Modular Architectural Tool (SMART). Other bioinformatic research sites and tools were ExPasy (Switzerland) and Swiss-prot (Switzerland).
Sequence analysis for restriction endonuclease digestion strategy design, PCR and sequencing primers design, and multiple alignments of DNA and protein sequences were done with the Clone Manager Professional Suite software.

VIII. 2.3 Cell biology methods

VIII. 2.3 i Mammalian cell culture

Maintenance of cells. NRK and HeLa cells are maintained in DMEM medium, and PtK_2 cells are maintained in MEM medium. Cells were cultured in growth medium at 37°C in a humidified 5 % CO_2 incubator. For subculturing the cells, they were washed once with 0.5-1.0 ml of trypsin/EDTA solution, followed by addition of another 1-2 ml of trypsin/EDTA solution and incubated for 5 min at 37°C. The cells were then resuspended in a total of 2-4 ml of growth medium and plated into new culture dishes at the necessary dilutions.

Freezing and thawing of cells. Cells from a confluent dish were resuspended and centrifuged in a Megafuge (Heraeus) for 2 min at 1000 rpm. The supernatant was discarded, the cell pellet resuspended in ice-cold freezing medium and transferred into 1.5 ml cryo-tubes (Nunc). Cells were transferred to -80°C for O/N freezing. Long term storage was performed in liquid nitrogen. Cells were thawed quickly by warming them in a 37°C waterbath. To remove the DMSO from the freezing medium, the suspension was diluted 1:5 v/v in growth medium and centrifuged in a Megafuge for 2 min at 1000 rpm. The supernatant was discarded, the cell pellet was resuspended in the final growth medium quantity and poured into a dish. The cells were split for the first time after at least a 12 h incubation period, depending on confluency.

Plating and incubation of cells before imaging. NRK, HeLa and PtK_2 cells expressing fluorescently tagged proteins for live-cell microscopy were prepared typically 1-2 days before imaging, 10-50 000 cells were seeded into 1-; 2-; 4- or 8-well LabTekII chambers. For mitotic imaging and/or Hoechst 33342 imaging (0,1-0,2 μg/ml), the cells were changed to pre-warmed imaging medium at least 1 h before observation and maintained and imaged at 37°C on the microscope stage..

NRK cells synchronization. A critical step for imaging mitosis is the identification of cells at the desired cell cycle stage. In asynchronous cell populations the fraction of mitotic cells typically is only about 1-5%. However, mitotic cells can be enriched up to 20-50% by synchronization. NRK cells are easily synchronized by arresting them in the transition between the "Growth 1" (G1) and "Synthesis" phases (S-phase) and then releasing them from this block. Aphidicolin (0,5 μg/ml), which blocks DNA replication by directly binding and inhibiting DNA polymerase II, was pre-mixed in growth medium and added to the cells to start synchronization. After a maximum of 18 h incubation and 3-5 hours before imaging, the cells were released from the aphidicolin block by rinsing and then washing three times with medium, with 10 min incubations between each wash

VIII. 2.3 ii Gene delivery into mammalian cells

DNA transfection has become an important tool for studying the regulation and function of genes. Some of the more widely used transfection techniques include calcium phosphate co-precipitation, electroporation, and the use of viral vectors and also cationic liposome-mediated transfection. In this work the FUGENE6 transfection reagent (Roche) with a non-liposomal formulation was used.

For the transfection with the FUGENE6 transfection reagent the cells were ~50 % confluent. Cells were plated at the appropriate dilution on the previous day, in LabTeks of the desired size, then typically incubated O/N at 37°C before transfection. Cells were transfected according to the manufacturer's instructions. After transfection cells were incubated from 12 h up to 48 h at 37°C.

VIII. 2.3 iii RNA interference-mediated depletion of proteins

In recent years, an important tool for cell and molecular biology has become the downregulation of genes by depletion of endogenous transcripts with a small-interfering (si)-RNA-mediated enzymatic degradation involving the cellular RNAi machinery (reviewed in Hammond, 2005).

RNAi depletion of the common condensin I and II sub-unit SMC2 (CAP-E). An established assay was used to deplete targeted condensin sub-units by RNA interference (RNAi) using HeLa (Kyoto) cells stably expressing H2b-EGFP as described (Hirota et al., 2004), and transfection and imaging protocols as well as validated Scrambled (Scr) and SMC2 siRNA oligos as described (Gerlich et al., 2006). In short, annealing of siRNA oligonucleotides was performed according to the manufacturers instructions. For control transfections, annealing reactions were carried out with the non-depleting Scr siRNA, Oligofectamine only, or Optimem only as negative controls. Transfection efficiency was controlled in parallel by EGFP depletion, monitored by the loss in fluorescence, and also by Polo-like kinase depletion that results in a penetrant prometaphase arrest.
Oligonucleotide transfections into HeLa cells were carried out by incubating 100-200 nM duplex siRNA with oligofectamine (Invitrogen) in fetal calf serum (FCS)-free medium according to the manufacturer' s instructions. After 4-8 h FCS was added to a final concentration of 20% (v/v). All experiments were performed 48 hr or 72 hr after transfection. Imaging conditions are described in chromatid shortening assay section.

RNAi depletion of the PNUTS protein. In each of 3 independent experiments, HeLa (Kyoto) cells, stably expressing H2b-EGFP, were transfected by standard Oligofectamine treatment, with a final cc of 100 nM of the control or PNUTS siRNA oligonucleotide as described above.

Imaging of PNUTS-depleted cells. After 48 and 72h, 6 locations with groups of cells for each treatment were imaged every 7 min for a total of 12 h, with automated location-tracking and focusing (Rabut and Ellenberg, 2004). For all PNUTS-depleted and control (Scr) mitotic cells that stayed in the imaged location, the time spent in each mitotic phase was scored visually. In addition, for a subset of these cells, prophase condensation kinetics were measured by quantitative image processing assay developed for this type of analysis (see description on the fluorescence intensity distribution assay in the results section).

VIII. 2.3 iv Cell fixation for indirect immunofluorescence (IF) microscopy

Methanol fixation protocol.
To fix cells, glass cover slips were directly transferred from their growth medium into -20°C cold methanol and incubated for exactly 10 min. Methanol both fixes the cells and permeabilize their

plasma membrane. Cells were washed once with 1 ml of PBS at room temperature. At this stage the cover slips can be stored at 4°C for up to two days.

Paraformaldehyde (PFA) fixation protocol.

The advantage of PFA fixation is that this treatment does not extract soluble molecules from the cytoplasm. If desired, permeabilization of the membrane was performed with a detergent, e.g. Triton X-100 or saponin.

Cells were incubated for 20 min at room temperature in 3.5 % PFA in PBS. They then were washed thrice in general IF medium. Higher permeabilization was achieved with 0.1% Triton X-100 in PBS for 2-5 min at room temperature.

Immunostaining

After fixation, 10 µl of the primary antibody in its appropriate dilution in IF medium were applied and incubated for 0.5-1h at room temperature by pipetting the antibody mix on a parafilm surface and laying the coverslip cell-face down on the drop, and covering the entire parafilm surface with an opaque cap, to prevent desiccation and bleaching of the fluorophores. After three washes in IF medium, 10 µl of the secondary antibody were applied in similar fashion. Depending on the first antibody, a corresponding anti-mouse, anti-rabbit or anti-goat secondary antibody conjugated with an appropriate fluorescent dye was chosen. Unbound secondary antibodies were washed away three times with IF medium. Finally the cover slips were mounted on a 7.5 µl of Fluoromount placed on glass slides. After 10 min drying period the edges of the coverslip were sealed with nail-polish and were ready for fluorescence microscopy after 15 min drying. A double immunostaining is a variation of an immunostaining in that a mixture of two primary and then two different secondary antibodies, which recognize the first antibodies specifically, are used.

VIII. 2.4 Confocal microscopy and image processing methods

VIII. 2.4 i Fluorescence labeling of chromosomes

Green Fluorescent Protein (GFP) is an efficient and convenient tag to visualize virtually any protein in live cells. It has therefore been widely used to localize proteins in subcellular compartments (reviewd in Lippincott-Schwartz and Patterson, 2003).

GFP-histones. The abundance and very low dissociation from DNA of core histones, the spectral properties, photostability and high quantum yield of EGFP, and the relatively high tolerance of cells to histones with inert tags, make the stable expression of EGFP-tagged core histones the method of choice to follow dynamics of all chromosomes (Belmont, 2001; Kanda et

al., 1998; Kimura and Cook, 2001). Core histones are among the most abundant cellular proteins (20-30 Mio copies/mammalian nucleus, (see appendix(Beaudouin et al., 2006)) and bright labeling can be achieved at low expression levels compared to the endogenous protein. Chromosomes are a convenient landmark for mitosis and their labeling can thus be combined with that of other mitotic structures using spectrally distinct FPs or dyes. Stable cell lines that express fluorescent histones can be generated readily and provide convenient tools to investigate mitotic chromosome dynamics, even in high throughput (Neumann et al., 2006, in the press).

Hoechst. Cell-permeable chemical dyes that specifically bind DNA, such as Hoechst 33342, can be successfully used to stain chromosomes (Belmont et al., 1989; Zink et al., 2003). Importantly, Hoechst preferentially stains A-T-rich DNA, which leads to underepresentation of G-C-rich sequences and bright labeling of AT-rich repeat sequences. Also, Hoechst has to be excited with near UV or UV wavelengths and thus requires stringent phototoxicity controls (see below). The combined negative effects of DNA binding (high doses of Hoechst may prevent mitotic condensation), free radical production upon over illumination and direct UV phototoxicity can quickly perturb the cells. Nevertheless if used at low concentration (Beaudouin et al., 2002) and very low illumination conditions, Hoechst can be useful as a simple cell permeable and highly specific DNA counterstain. For high resolution work however, requiring intense illumination, stably-expressed genetically encoded fluorescent proteins were used.

VIII. 2.4 ii General imaging settings

2-, 3- and 4D imaging was performed on customized Zeiss LSM 510 or LSM 510 Meta (Carl Zeiss, Jena), or a Leica TCS SP2 AOBS (Leica Microsystems, Mannheim) confocal microscopes. Microscopes were typically equipped with z-scanning stages (HRZ 200), ultra-sensitive PMTs (Zeiss), a Kr 413 nm laser (Coherent GmbH, Dieburg, Germany) or 405 nm laser (Zeiss) and custom dichroics and emission filters (Chroma Inc., Brattleboro, VT) optimized for fluorescent protein imaging inside living cells.

Typically and unless otherwise indicated, images were acquired with a PlanApochromat 63X NA 1.4 oil DIC objective (Zeiss). Planapochromat objectives are corrected for spherical and chromatic aberrations and typically have a high numerical aperture. This translates into bright, sharp and flat images with a shallow depth of field. This lens also permits the acquisition of high-contrast transmitted light images because of an additional DIC prism. Fluorescent chromatin and other cellular structures were automatically tracked and focused during imaging using in-house developed macros previously developed in the group as described (Rabut and Ellenberg, 2004).

VIII. 2.4 iii The control of phototoxicity

An important initial step in live imaging experiments is to titrate the amount of light the biological system can tolerate without perturbing the process under investigation, in this case mitosis. This can be effectively assessed with comparison with the normal morphology and timing during cell cycle progression of cells undergoing division in the absence of continued illumination. One way to obtain such reference is by transmission or fluorescence imaging at the lowest possible space-time resolution to be able to follow the cell. For this, illumination should be performed with long wavelengths of low-energy visible light above ~500 nm, either with a laser or, if white light sources such as arc lamps are used, with appropriate dichroic mirror and excitation filter combinations that stringently exclude lower wavelength radiation. Normal cell cycle timing and morphology was thus established with minimal illumination, and the high resolution imaging was optimized to show as little deviation as possible from this reference. Typically, optimization was started with the minimum illumination required to obtain acceptable spatial resolution and signal-to-noise ratio and minimal sampling frequency to record the dynamic structural transitions of interest. For example, in the photomultiplier-based confocal microscopes used here, the pinhole was relatively open, the laser power and initial resolution was low (128^2 or 256^2 with low zoom), and the voltage-controlled gain high. Then, the illumination and sampling frequency was then progressively increased until the first signs of phototoxicity were detected.

The following parameters were used to control phototoxicity:

(1) Cell cycle duration
(2) Full mitotic progression without compaction, congression and segregation defects.
(3) Total duration of mitosis and of the different mitotic stages.
(4) Cytokinesis completion and substrate reattachment.
(5) The morphology of the cell, the nucleus and its structural components, such as chromosomes, cytoskeleton and membranes.

VIII. 2.4 iv Quantitative imaging and image processing

Fluorescence microscopy is most powerful when performed quantitatively to determine kinetic profiles, for example here of defined structural parameters of chromosomes. For this, it is necessary to first obtain quantitative images, where all fluorescence signal produced by the sample, including the background, are recorded within the dynamic range of the detector. My objective was to analyze the dimensions, geometry and the condensation state of chromatin

quantitatively. Typically, the entire volume occupied by chromosomes within the cell during the observation was sampled over time to enable tracking of chromosomes and compensation of inherent movements and deformations of the cell, the chromosomes and focus shifts. 4D images of only subsets of all chromosomes were also acquired during the chromatid length measurement assays to minimize illumination, but then only chromosomes fully contained in those limited stacks of images were selected for measurement.

A sequential multi-position acquisition of several cells during long periods was used here for the volumetric measurements. This facilitated and increased the throughput of quantitative images of the dividing cells. Also, tracking and auto-focusing can lower the risk of "missing the action", especially during long experiments, by compensating for focus drifts or cell movements (Rabut and Ellenberg, 2004). Full implementation of flexible procedures for 4D live-cell imaging usually requires solutions partially or fully developed by the researchers themselves. Many microscopes now offer the possibility to develop macros to extend the hardware-control capabilities, as utilized by our group (e.g. Rabut and Ellenberg, 2004).

General microscopy and image processing protocols from the group have been described (Beaudouin et al., 2002; Gerlich et al., 2001; Gerlich and Ellenberg, 2003). Other protocols developed and used for the new quantitative imaging assays presented here are described as part of the results section.

VIII. 2.4 v FRET microscopy methods

Förster (or Fluorescence) Resonance Energy Transfer (FRET) is a measure of the molecular proximity between two compatible chromophores, i.e. when the emission spectrum of a donor chromophore overlaps with the excitation spectrum of an acceptor chromophore. This property can be thus used to estimate distances between molecules of interest attached to them. FRET occurs by the radiationless transfer of excited state energy from a donor to an acceptor chromophore by dipole coupling. The efficiency of energy transfer thus depends on the spectral overlap, the relative orientation between the dipoles of the two dyes and, most importantly, it is inversely proportional to the sixth power of the distance between the two dyes. This is seen in equation 1, where E is the FRET efficiency, r the distance between chromophores and R_0 is the distance where the transfer has a 50% efficiency (known as "Förster distance" and typically ~2-6 nm).

(1) $$F = \frac{R_o^{\,6}}{R_o^{\,6} + r^6}$$

This makes FRET a highly distance-dependent phenomenon and gives it a practical range between 1-10 nm for most commonly used chromophores (Förster, 1948; Herman, 1989). This distance is in the range of the molecular proximities required for interactions. Therefore, by measuring the efficiency of FRET, protein-protein interactions can be identified and quantified *in situ*; but if specific techniques are used, also *in vivo* (Herman et al., 2004). FRET values can be obtained by fluorescence decay methods such as Fluorescence Lifetime Imaging (FLIM), and by fluorescence intensity methods (Wouters et al., 2001). In this work intensity-based methods were used to study chromatin in living cells. For this, I established reporters to sense possible interactions within and between the tails of the H2b core histone, tagged with EGFP and ReAsh.

FRET measurements with intensity-based methods: The tC-ReAsh system.

Possible interactions within and between the carboxy-terminus of the H2b core histone, tagged with EGFP and a the tetra-cysteine (tC) motif -CCPGCC- specifically designed to bind ReAsh, a biarsenic compound derived from resorufin, which becomes fluorescent only when specifically bound to tC motifs and upon excitation with either 532, 543 or 561nm laser lines and emits red light (fig. 21). This sequence also binds to FlAsh, a similar derivative from Fluorescein that emits green light (Adams et al., 2002). FRET in this system was monitored with the acceptor photobleaching, sensitized emission and spectral scanning techniques.

For fixed-cell measurements, the "acceptor photobleaching" technique has the advantage that FRET efficiencies can be easily calculated. The acceptor fluorophore ReAsh was bleached with 10-20 fast pulses of a 543 nm HeNe laser at maximal power (recent stronger lines with longer wavelengths, such as the 561 nm, allow more efficient bleaching and should be preferred). The increase in emission in the donor channel was used to calculate FRET according to:

(2) $$aF = 1 - \left(\frac{fb - B}{fa - B} \right) = F \bullet \alpha D$$

where *aF* is the apparent FRET efficiency, *fa* & *b* are the fluorescence signals before and after bleaching, B the extra-nuclear background, *F* the true FRET efficiency and αD is the fraction of tagged molecules in the sample (equal to 1 for intra-molecular reporters).

However ratio imaging is the better choice for time-lapse experiments, as the acceptor is not destroyed. Relative FRET efficiencies can be calculated and compared according to:

(3) $$rF = \frac{(Ff - B)}{(Df - B)}$$

Where *rF* is the normalized ratio of FRET efficiency, *Ff* is the sensitized emission fluorescence of the acceptor and *Df* is the donor fluorescence. (Wouters et al., 2001).

ReAsh labeling of cells. NRK cells were plated on LabTek chambers three days before the experiment. The following day, they were transfected with different constructs of histones tagged with FPs and/or with a tC motif, either in the same fusion protein, or in a second histone construct (see results). These cells were used to image chromatin during interphase and mitosis, and to probe interactions within and between the H2b tails, through FRET measurements. Typically, EGFP was the FRET donor and tC-ReAsh the acceptor.

Cells transfected with a fusion protein with a tC tail were incubated with a ReAsh solution: Prior to incubation with the cells, ReAsh was mixed with a 10-fold higher concentration of EDT, then pre-mixed with serum-free medium to the desired concentration. For live cells ≤ 0.5 μm was used. Typically, a good compromise between good signal, cell integrity, and little background was 0.2 μm. Cells are incubated with this solution a minimum of 1 h at 37ºC. Occasionally, for selection, cells were incubated for 48 h without visible deleterious effects to cell cycle or morphology. After the incubations, cells can be rinsed once and then washed 2 x 5 min before imaging with serum-free medium (serum greatly depletes ReAsh by unspecific bindings) to optimize mitosis progression. However if 0.2 μm were used without washing, no major effects were detected, and this compensated to some extent the photobleaching of ReAsh during imaging. For cells fixed with standard methods (see above), ReAsh cc can be up to 1-2 μm to ensure saturation levels of binding to the tC sequences, but this results in increased background. Washing of fixed cells can be done with PBS. ReAsh and EDT must be stored in small aliquots, at -20°C, protected from light to prevent bleaching and oxidation.

VI Results

VI. 1 Maximal chromosome compaction occurs by axial shortening in anaphase and depends on dynamic microtubules

VI. 1.1 A volumetric assay for large-scale chromatin compaction

To quantitate overall changes in large-scale chromosome compaction, a monoclonal NRK cell line was established that stably expresses EGFP-tagged core histone-2b (EGFP-H2b) as a fluorescent marker for chromatin (fig 5). This cell line had a normal morphology and cell cycle compared with the maternal line, and the fluorescence localization through the cell cycle, as well as the redistribution after photobleaching of EGFP-H2b was consistent with the literature (Gerlich et al., 2003; Kanda et al., 1998; Kimura and Cook, 2001).

All fluorescent chromatin was recorded from G2 through mitosis by 3D time-lapse (4D) automated confocal imaging, starting 4 to 5 hours after release from a G1/S block, before mitotic entry. Typically for each nucleus, 18 optical sections of 512*512 pixels, (xyzt resolution: 0.06*0.06*1.5 μm*5min) were acquired for a maximum of 10 h. After optimization of the long-term imaging conditions, this was the highest possible spatio-temporal resolution allowing sufficient signal to noise for subsequent data processing without perturbing mitotic progression (fig. 5). The relative changes in the volume occupied by the fluorescent chromatin through mitosis were quantitated using in-house developed macros, designed by Daniel Gerlich, formerly in our group and implemented for this purpose in Heurisko 4.0 (Aeon).

The raw fluorescence in each optical section was background subtracted and noise filtered by two-dimensional anisotropic diffusion that preserves edges in each optical section. Then, the intensity sum of all voxels in each 3D stack was equalized to the first time-point to correct for possible photobleaching effects, which were typically below 5 % during the entire experiment. A threshold to segment chromatin was set interactively in metaphase, when chromatin can clearly be distinguished from the cytoplasm (fig. 6 A). Within a narrow range, this threshold was then automatically adjusted for each 3D stack such that the intensity sum contained in the segmented chromatin volume was equal to the metaphase reference. The inverse of this volume then gives a

relative measure of the compaction. This volume is represented as isosurface reconstructions in figs. 6 A and 16 A & B (Amira 2.3, TGS Inc.). Variations of the segmentation threshold by ± 10% did not affect the measured kinetics of relative compaction (not shown). The spatial resolution of this assay is limited by the resolution along the optical axis of ~0.8 μm and the undersampling in this direction of 1.5 μm. Detailed discussions of quantitative 4D fluorescence imaging and image processing during mitosis have been published by the group (Gerlich et al., 2001; Gerlich and Ellenberg, 2003).

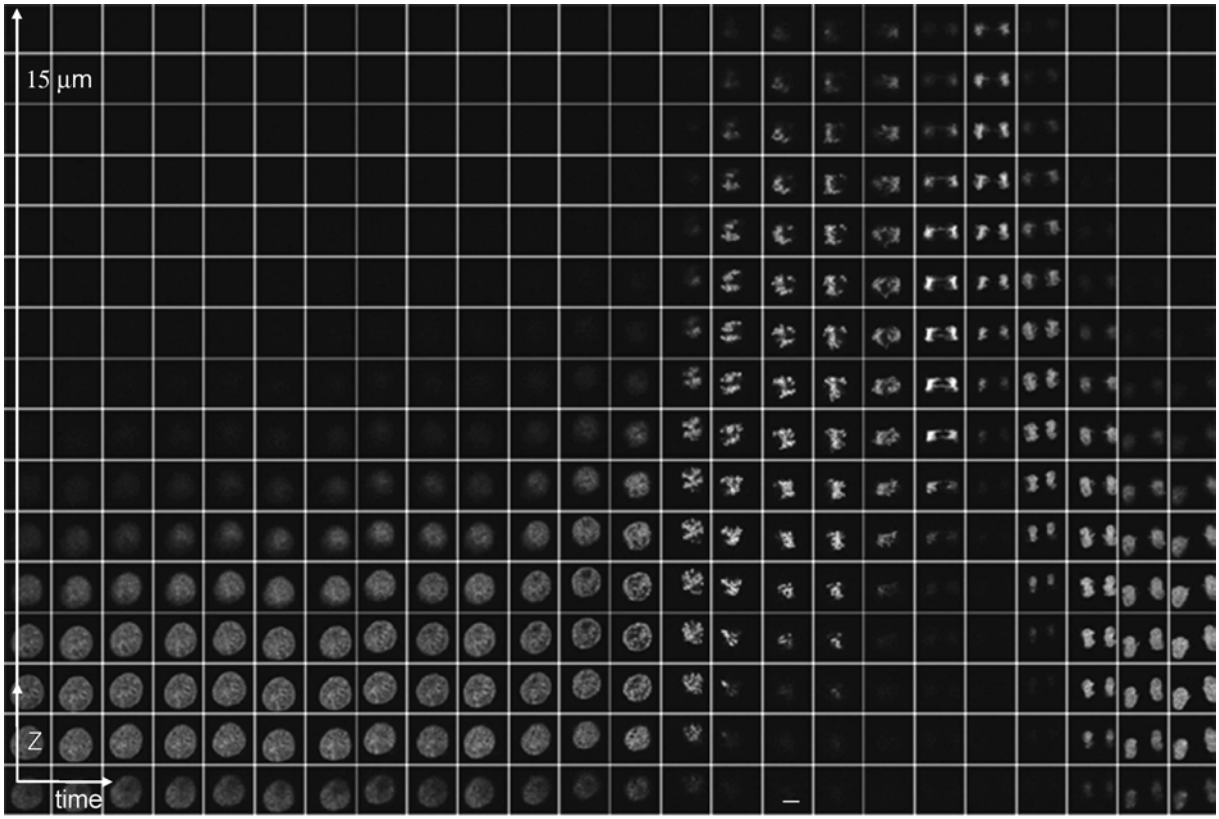

Figure 5. Imaging of an entire mitosis. Monoclonal NRK cell line used for the volumetric assay, stably expressing EGFP-H2b. Typical sequence of the entire chromatin recorded through mitosis by 4D confocal imaging. Images in columns were taken every 1.5 μm along the optical (Z) axis. Images in rows correspond to the time-lapse, taken every 5 min. Bar = 10 μm.

VI. 1.2 Chromatin occupies minimal volume in anaphase, not metaphase

VI. 1.2 i Chromatin is maximally compacted in anaphase

The volumetric assay showed, as expected, that the overall compaction of chromatin remained constant during G2 and increased markedly during prophase and prometaphase, reaching a first peak in metaphase (fig. 6 A, B). Sister chromatid segregation by the mitotic spindle then resulted in a decompaction in early anaphase. Surprisingly, after segregation was completed and before telophase decompaction started, chromatin recompacted to reach its overall maximal compaction 25% above metaphase levels in late anaphase, ~12 min after the metaphase-anaphase transition (fig. 6 B). Afterwards, chromatin rapidly decompacted during telophase as expected. Small variations in the duration of the individual mitotic phases prevented the precise temporal alignment of data from different cells at this relatively low time resolution. For plots with standard deviations for this assay on datasets with higher temporal resolution, and thus more suitable for precise alignment and averaging, see fig. 16 A, D. According to this assay, the overall volume occupied by chromatin decreases only between 2 and 3-fold from interphase to mitosis. It is necessary to note, however, that important changes in chromatin structure and compaction can occur below the resolution of 4D live-cell imaging and may thus be underestimated.

VI. 1.2 ii The retraction of protruding chromosome arms in anaphase may explain the compaction.

To characterize this novel anaphase compaction, dimensional changes of chromosomes were analyzed from metaphase to telophase in 4D datasets with higher temporal resolution. Around two minutes after anaphase onset, when segregation was completed and before decompaction in telophase, I observed a progressive retraction of the chromosome arms that protruded from the chromatin mass formed by sub/centromeric regions focused at the spindle poles (fig. 7 A). This retraction occurred from the telomere to the spindle pole, away from the central spindle and future cytokinesis plane. Quantitation of this retraction showed that it started after poleward migration of (sub)centromeric chromatin masses was ~80% complete and progressed at a constant rate, while pre-cytokinesis poleward migration showed plateauing kinetics, already slowing at the onset of retraction and then halting ~4 min after anaphase onset, when retraction had proceeded only one fifth (fig. 7 B). Consistent results were obtained from n=34 chromatids in n=15 cells in independent experiments (fig. 13 A). Thus, when poleward migration slows and

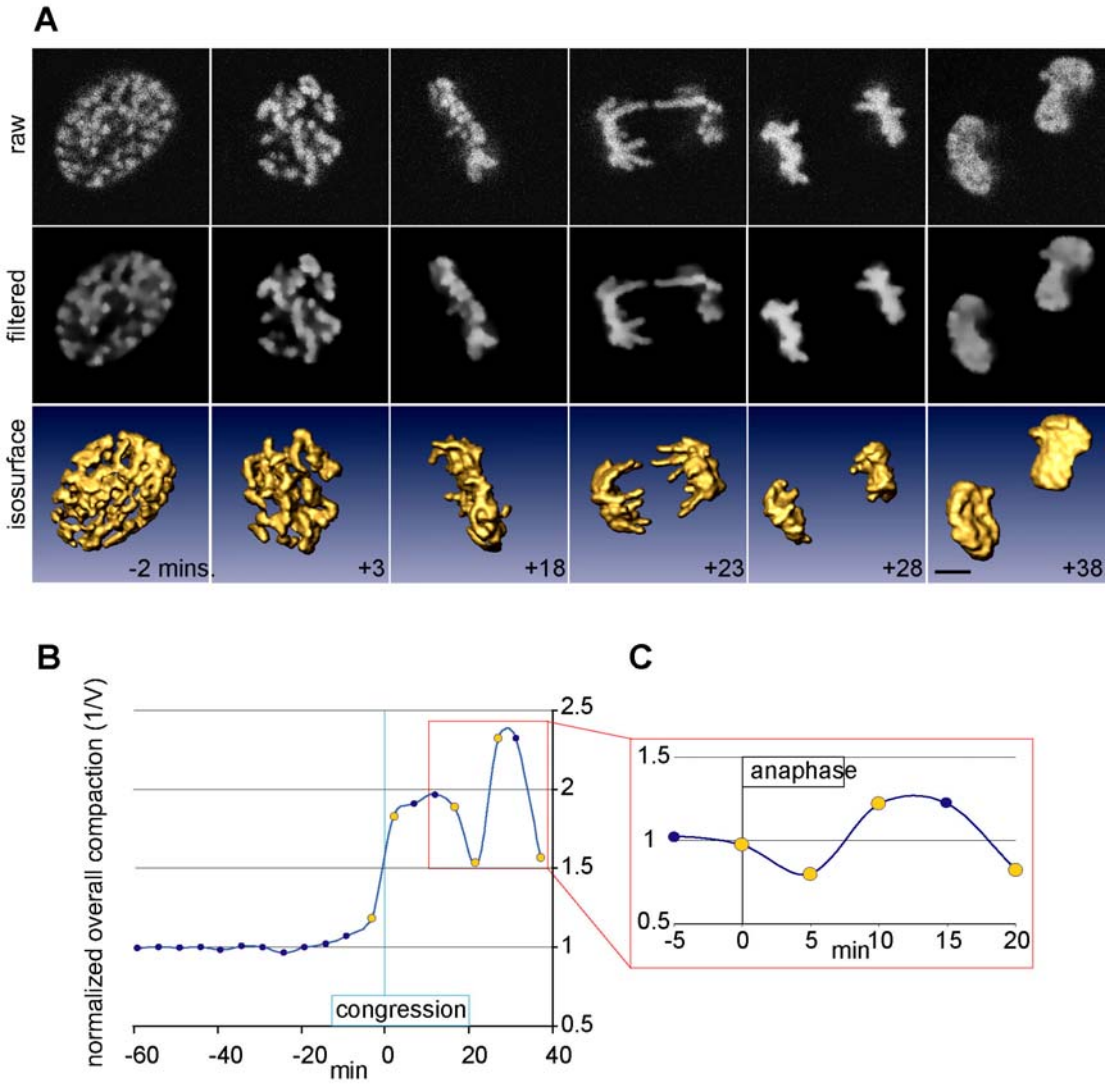

Figure 6. Overall compaction of chromatin by volume measurements: the highest compaction level is in anaphase. Large-scale changes in the volume occupied by chromatin through the cell cycle are quantitated in a monoclonal NRK cell line stably expressing EGFP-H2b. **(A)** Using in-house developed macros, the raw fluorescence signal in each confocal section in a stack (1st row) was filtered and normalized (2nd row). Then, the signal is segmented and quantitated by thresholding to measure relative changes in the volume that chromatin occupies over time (represented by an isosurface reconstruction with all sections (3rd row); time lapse = 5 min. The inverse of this volume gives a measure of the compaction. **(B)** Representative example where the compaction is normalized to 1 being the interphase situation. Congression is t = 0. Yellow dots in the curve correspond to the displayed images. Similar results were obtained from n=10 data sets from 5 experiments (not shown, but compare with fig. 16). **(C)** Zoom-in of the metaphase to telophase portion of the same compaction curve, normalized to 1 being the metaphase situation and with the same scale as fig. 16 C. Bar = 5μm.

stops, chromatid shortening reached its maximal steady rate, which remains unperturbed by the ingression of the cytokinetic furrow. This shows that chromosome arm retraction is both kinetically and temporally independent of poleward migration of separated chromosomes.

Chromosome arm retraction could indicate shortening of the whole chromatid, which would be a candidate mechanism underlying the overall reduction in chromatin volume observed in late anaphase in the volumetric assay.

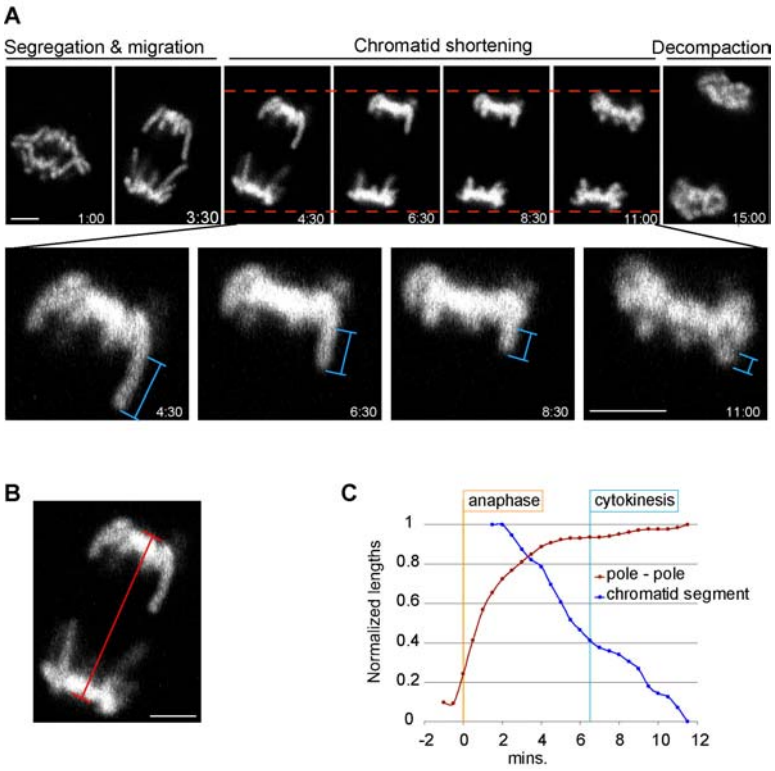

Figure 7. Anaphase chromatids retract. Confocal sections of the same NRK cell line as in figs. 5 & 6; but time-lapse = 30 s. **(A)** 2 to 3 min after anaphase onset, protruding chromatid arms retracted toward the separating poles and away from the equatorial division plane. Horizontal red lines mark the migrating fronts of chromatin masses. **(B & C blue)** Normalized length of a protruding chromatid segment (blue rulers in A). **(B & C red)** Normalized distance between the migrating edges of the chromatin mass formed by sub/centromeric regions (red ruler in B). The slight increase in distance between the chromatin masses that re-starts after 8-10 min was caused by the post-cytokinesis movements of the entire daughter cells. (See fig. 13 A for all data and lengths in μm). T = 0 is anaphase onset. Bars = 5μm.

VI. 1.3 Assays to measure chromosome length during anaphase

At the level of single chromosomes, arm retraction could be due to compaction by axial shortening of the chromatid, or simply a rearrangement of the chromosome position caused by continued poleward migration of its centromere, which could pull arms into the chromatin mass without shortening along the axis. To differentiate between these different mechanisms, 2 assays were developed.

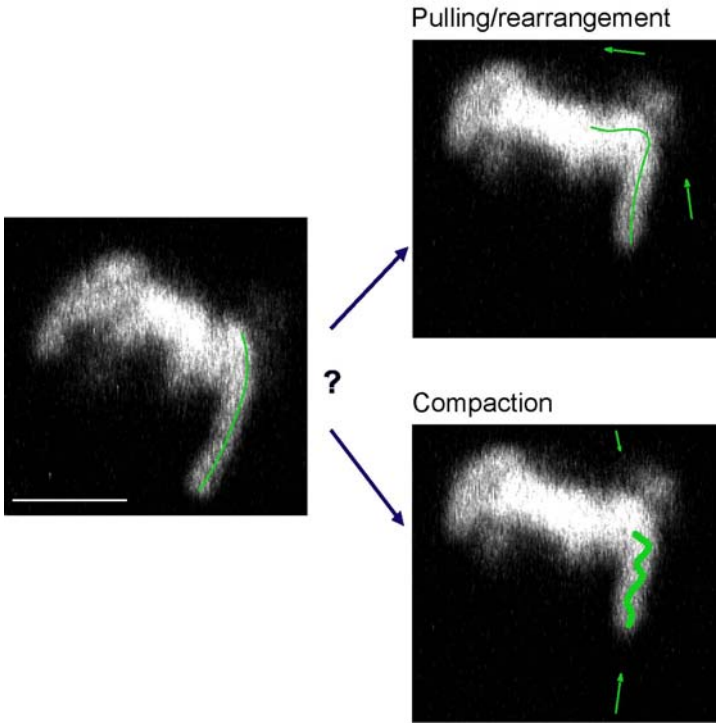

Figure 8. Two possibilities to explain the chromatid shortening in fig. 6. Is it a result of the poleward pulling? Or is it a compaction of the chromatid?

VI. 1.3 i Selective photolabeling of single chromatid arms

First, to measure defined segments in single chromatid arms during mitosis, an NRK cell line stably expressing H2b-PAGFP was used. Protruding segments of single chromatids were selectively photoactivated immediately after telomere separation in single optical sections with a short pulse of 405 or 413 nm laser. We could mark up to 5 µm long segments of single chromosomes during anaphase and follow their subsequent behavior during retraction with dual-color 4D imaging (Fig. 10 A).

VI. 1.3 ii Dual labeling of chromatin and pericentromeres

Second, to measure the entire length of single chromatid arms during anaphase, we differentially labeled pericentromeric heterochromatin by transient expression of the methyl CpG-binding protein MeCP2 tagged with EGFP, with vital Hoechst counter-staining as general chromatin marker (Fig. 9). Here we could measure the total length of single chromosome arms during anaphase, without being limited to protruding segments that could be marked by photoactivation (Fig. 10 B).

In both assays, the following imaging conditions were used: Anaphase was recorded in live NRK cells by 4D dual-color imaging. Stacks of five 256*256 images, (xyzt resolution 0.11*0.11*1.5 µm*30s) were acquired around the center of the chromatin mass. The lengths of chromosome segments were measured interactively using the LSM 510 3.2 software (Carl Zeiss, Jena). Only

chromatid arms contained in single confocal slices over time were analyzed to avoid distortions along the optical axis.

Illumination with 405/413 nm light in photoactivation and imaging to follow the fluorescence of non-photoactivated PAGFP, or Hoechst can perturb cell physiology. We thus minimized laser exposure and did not detect strong negative effects on mitotic progression, as cells completed segregation, poleward migration, cytokinesis, chromatin decondensation and reattachment to the substrate (see fig. 10 A, C). Nevertheless, chromatid shortening was slightly slower in some cases compared to cells not illuminated with 405/413 nm light. We therefore confirmed the qualitative shortening in 30 PA experiments and 15 dual pericentromere/chromosome labeling experiments, but quantitated the rate of shortening only in cells not exposed to 405/413 nm illumination (see below).

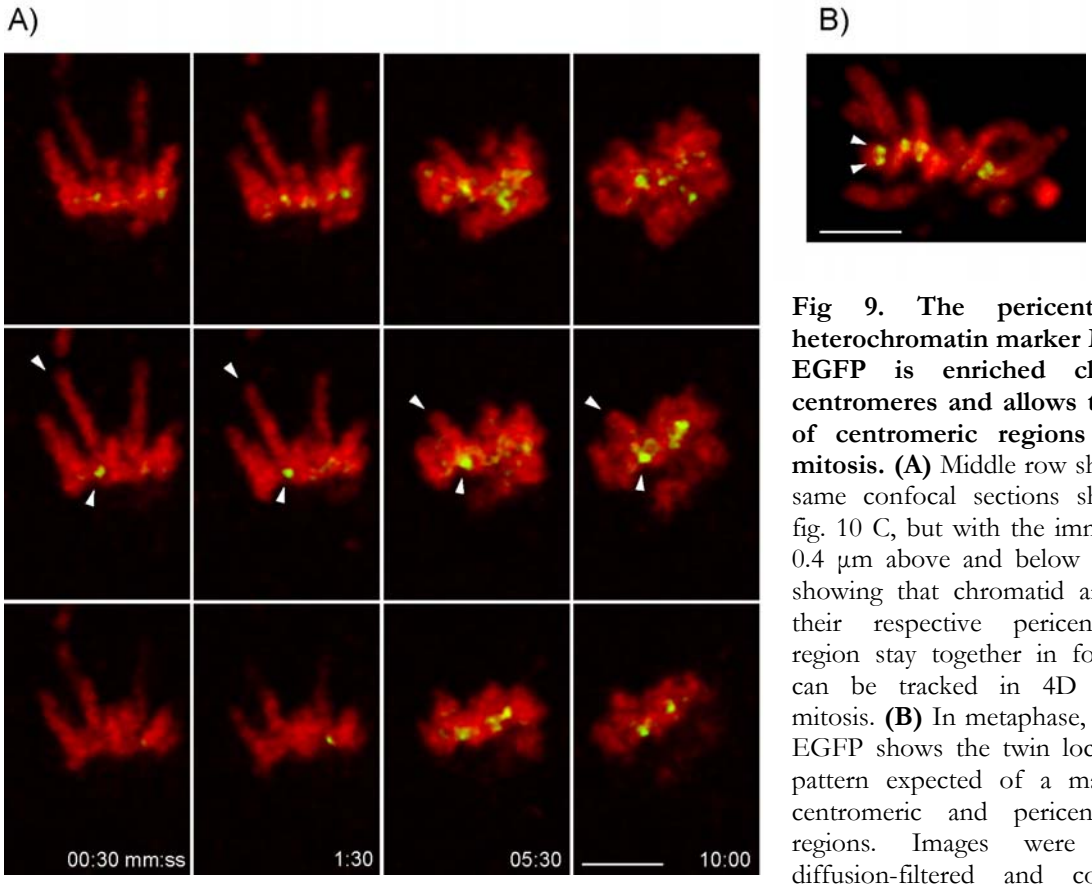

Fig 9. The pericentromeric heterochromatin marker MeCP2-EGFP is enriched close to centromeres and allows tracking of centromeric regions during mitosis. (A) Middle row shows the same confocal sections shown in fig. 10 C, but with the immediately 0.4 µm above and below sections, showing that chromatid arms and their respective pericentromeric region stay together in focus and can be tracked in 4D through mitosis. **(B)** In metaphase, MeCP2-EGFP shows the twin localization pattern expected of a marker of centromeric and pericentromeric regions. Images were equally diffusion-filtered and contrasted linearly to enhance red/green contrast. Bars = 5µm.

VI. 1.4 Single chromosome arms shorten along their telomere-centromere axis after segregation

If chromosomes compacted axially, the length of labeled segments followed with the two developed assays should decrease. If instead chromosomes were relocated within the chromatin mass, the length should remain constant but the whole segment should move within the chromatin mass (fig. 8). Photoactivation clearly showed that labeled segments of chromosome arms that protruded from the rest of the more tightly arranged chromatin mass shortened axially from the telomere to the chromatin mass (presumably towards their centromere), reducing their starting length to about half after ten to twelve minutes (Representative example of n=30 similar experiments in Fig. 10 A). In addition, this shortening correlated with a 2-fold increase in the intensity of the fluorescence labeling and thus the histone density in the segments, which also kept their position and orientation relative to the rest of the chromatin, (Fig. 10 A) inconsistent with a simple pulling and relocation mechanism.

To demonstrate axial shortening between telomere and centromere directly, we then imaged cells where both the entire chromosomes and pericentromeric region were differentially labeled by Hoechst and MeCP2-EGFP (Fig. 9). The distance between the pericentromeric region and the telomere of single chromosomes clearly started to shorten 1-2 min after anaphase onset, reducing their starting length to about half after 8-12 min (Representative example of n=15 similar experiments is shown in Fig. 10 B).

Together, these two assays clearly show that chromosome arms shorten axially after their telomeres have been segregated in anaphase. Given the consistent results obtained from measuring photoactivated protruding arm segments and measuring entire chromosome arms, I could use single color imaging of the general chromatin marker GFP-H2b, which allows acquiring data at higher resolution, to further investigate the mechanism of axial shortening.
The kinetics of shortening also excludes that this axial shortening results from a spring-like elastic recoil of chromosomes after stretching in anaphase. Shortening occurred slowly over several minutes with near-linear kinetics. Also, in 31 out of 34 control chromatids (91%), the post-segregation shortening either initiated more slowly than its mean rate, or started only after a delay of up to 1.5 min (Fig. 12 B, open arrow), consistent with a progressive axial compaction, but not with a spring-like recoil.

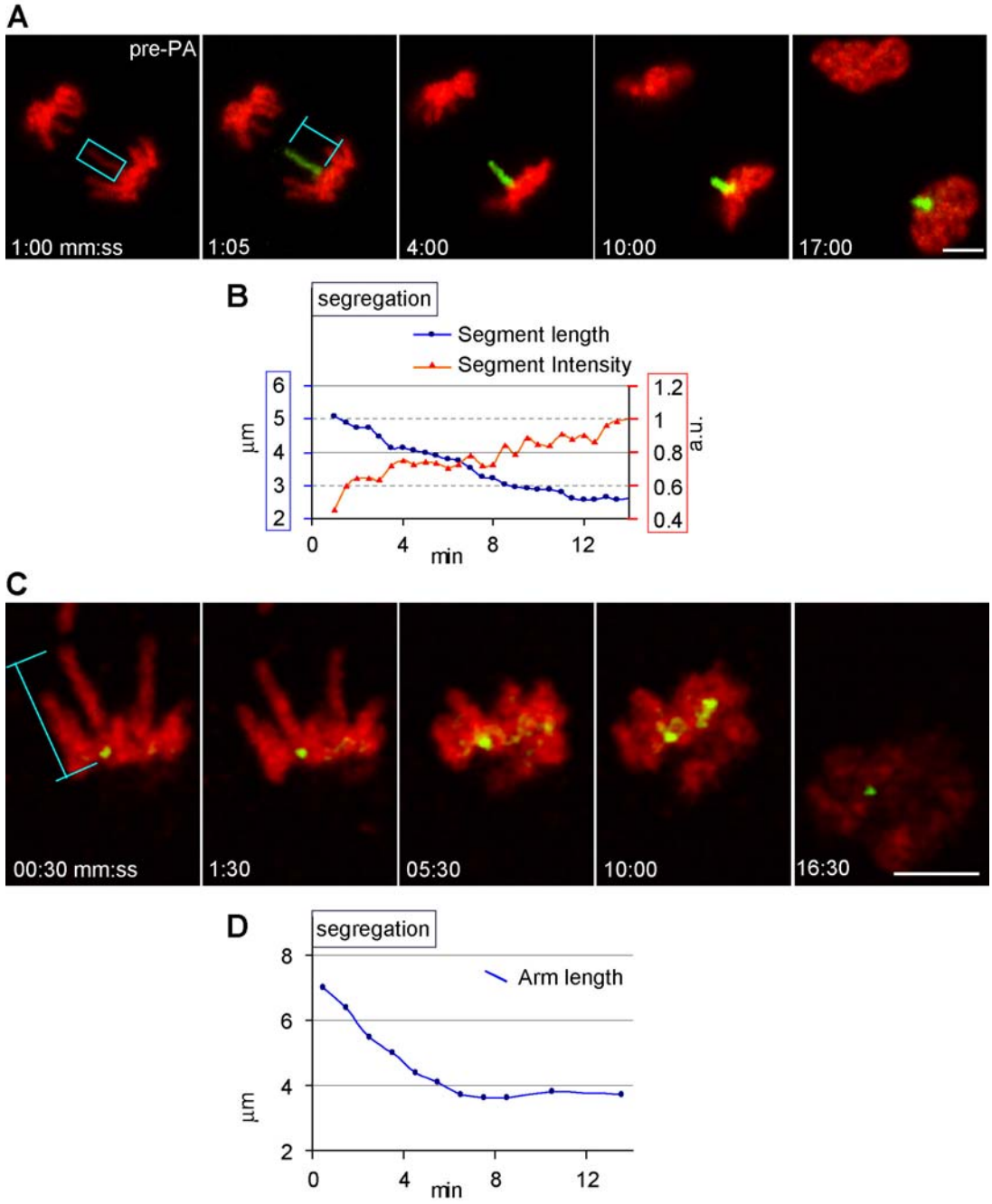

Figure 10. Chromatid arms compact by axial shortening in late anaphase. (A) Confocal sections of 4D imaging series of NRK cells stably expressing H2b-PAGFP. Distinct protruding regions in single chromosomes were labelled by photoactivation with 1 short near-UV pulse after segregation, which is t = 0. **(B)** In blue, length of painted segment over time in min. In red: fluorescence intensity of the same entire segment through mitosis; both quantities were measured from the raw signal (Representative example of n=30 segments from 19 cells and 5 experiments). **(C)** Confocal sections of 4D imaging series of NRK cells with chromosomes labelled by Hoechst (red) and pericentromeric heterochromatin labelled with MeCP2-EGFP (green). **(D)** Length between the pericentromeric region and the distal tip of single chromosomes over time in min. Accurate measurement of the fluorescence intensity for entire single chromatids through mitosis was challenged by the rapid blurring of boundaries between chromosomes as anaphase progressed (Representative example of n=15 arms from 9 cells and 6 experiments). Images were equally diffusion-filtered and contrasted linearly to enhance red/green contrast. Bars = 5µm.

VI. 1.5 An assay for the action kinetics of microtubule-perturbing drugs in anaphase

Axial chromosome compaction could be caused either by chromatin intrinsic forces or by forces involving mitotic microtubules. To test whether microtubules were involved, it was crucial to perturb them as acutely and rapidly as possible, without affecting chromosome segregation in early anaphase. For this, an assay was developed to quantitate the kinetics of action of taxol and nocodazole on live mitotic spindles. High doses of these two potent microtubule perturbing agents were applied immediately after segregation of the last pair of sister chromatids.

Experimental conditions. To verify that the drugs would affect microtubules rapidly enough to affect chromosome arm shortening within 10-12 min after segregation, their kinetics of action were measured by 4D imaging of NRK cells stably expressing α-tubulin tagged with EGFP and stained with Hoechst to follow mitotic progression at low resolution. In such data sets the proportion of structured tubulin signal was later quantitated by analysis of the pixel intensity distribution of tubulin. Typical stacks of three 256*256 images (xyzt resolution pixel size: 0.11*0.11*2 μm*30 s), were acquired around the pole-pole axis of the mitotic spindle. To perturb microtubules, pre-warmed solutions of nocodazole or taxol ranging from 0.1 to 50 μM were added to the imaging medium immediately after segregation of sister chromatids.

Quantitative image processing. To automatically quantitate the effects of the drugs, I developed macros in ImageJ (http://rsb.info.nih.gov/ij/; See appendix 1)

Maximum intensity projections of the fluorescent tubulin channel were generated and masked by Gaussian diffusion and thresholding with a single value defined interactively to segment the whole cell. The extracellular background was subtracted from the raw intracellular signal in the segmented images. Then, the mean fluorescence intensity and the standard deviation (SD) of all pixel intensities within the cell were calculated. The SD was then normalized to the corresponding mean fluorescence intensity in each image to account for cell movements and focus shifts. The normalized SD of pixel intensities is a simple relative measure of the heterogeneity of the fluorescence distribution (Fig. 11), and is therefore high in cells with structured microtubules as a result of taxol stabilization and low in cells containing just soluble tubulin after depolymerization by nocodazole.

Optimal microtubule perturbation conditions. A final concentration of 20 μM of both taxol and nocodazole was optimal to most efficiently perturb microtubules with limited unspecific damage to the cell during the 10-15 min duration of anaphase. This microtubule-perturbation assay showed that 20 μM nocodazole began to depolymerize anaphase microtubules within 30 s after addition and the spindle was almost completely depolymerized after 2 min (Fig 11 B, C),

consistent with previous findings from the group in fixed NRK cells (Beaudouin et al., 2002). Microtubule depolymerization with nocodazole did not unspecifically affect all aspects of chromosome dynamics, because all treated cells decompacted chromatin in telophase in the presence of nocodazole (see Fig. 12 E). However, as expected, most of the nocodazole treated cells did not complete cytokinesis and attachment to the substrate in G1 normally.

Similar to nocodazole, 20 µM taxol also strongly perturbed mitotic spindle morphology by hyperstabilizing microtubules within 2 min after addition, as shown by a strong increase in the structured microtubule fluorescence. (Fig. 11 B, C). In contrast to nocodazole, all taxol-treated cells completed cytokinesis and decompacted chromatin with close to normal kinetics, and attached to the substrate, albeit with a delay (Fig. 12 C).

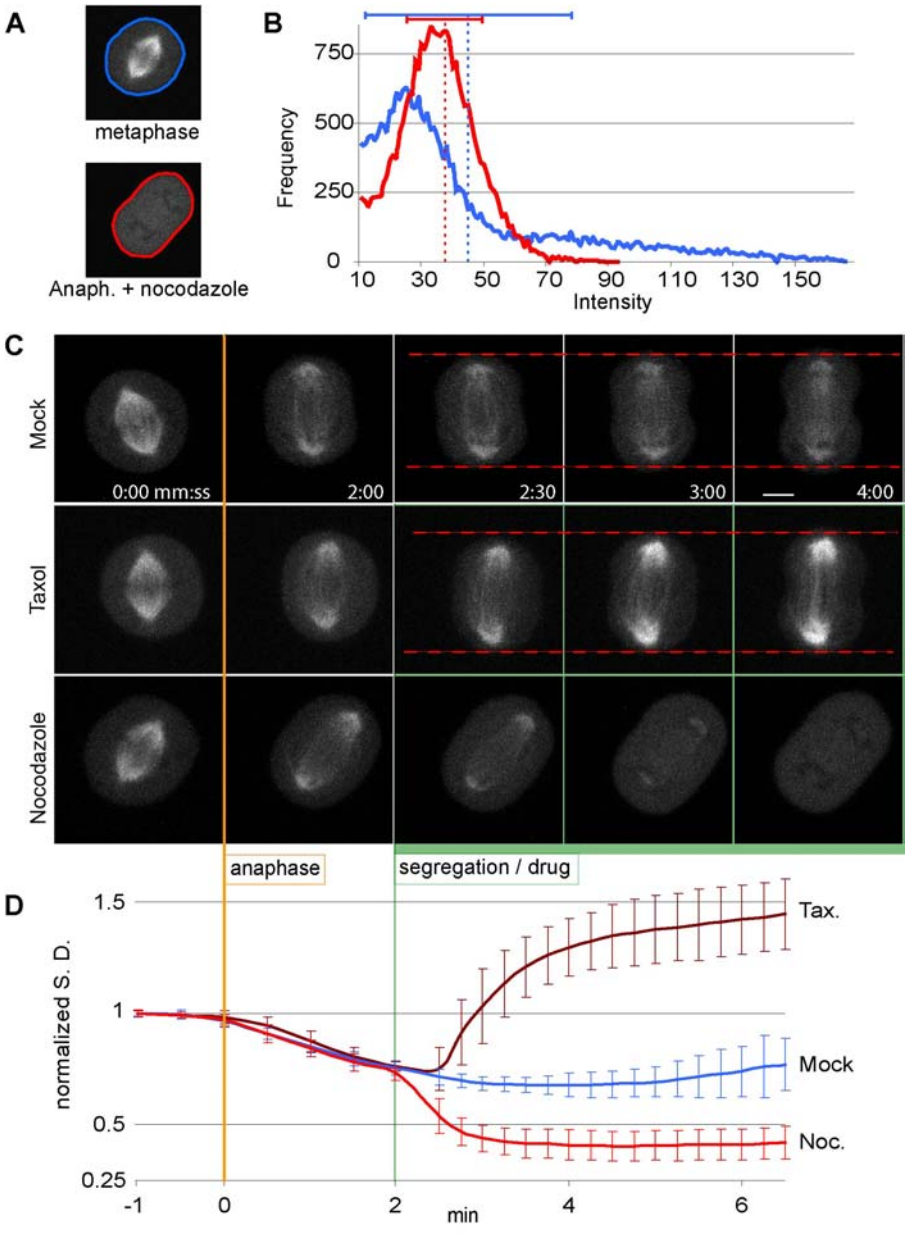

Figure 11 (prev. page). Microtubule poisons acutely perturb the anaphase spindle within 2 min. 4D imaging from meta- to telophase of a monoclonal NRK cell line stably expressing mEGFP-α-tubulin. **(A)** The normalized standard deviation (SD) of all pixel intensities inside the cell was calculated with developed macros (appendix 1). **(B)** Distribution of intensities: metaphase in blue; anaphase incubated 2 min with nocodazole in red. Dotted vertical lines are the mean intensities for each. The SD is high in cells with distinct structured microtubules (blue horizontal bar) and low in cells with mostly soluble tubulin after depolymerization (red horizontal bar). **(C)** Nocodazole or taxol added to the imaging medium 2 min post-anaphase onset, when segregation is completed. **(D)** In n=10 mock-treated independent cells, only pre-warmed medium with an equivalent cc of solvent (DMSO) was added. Spindle microtubules display a constant intensity distribution during metaphase and the fluorescence heterogeneity decreases when K-fibers depolymerize in anaphase, thus lowering the SD by ~30%. When nocodazole was added to n=10 cells from independent experiments, microtubules depolymerized within 30 s and were almost completely depolymerized after 2 min, as shown by a further lowering in the SD by ~30% compared to controls. Taxol strongly hyperstabilized microtubules within 45 s of addition to n=10 cells from independent experiments, as shown by a strong increase in the local brightness and heterogeneity of the microtubule fluorescence and a ~50% increase in SD, compared to controls. Note that some spindle elongation proceeds in the presence of taxol (C, red dashed bars).Bars = 5μm.

VI. 1.6 Requirements for anaphase chromosome shortening: a new role for microtubules in mitosis

VI. 1.6 i Dynamic microtubules are required for shortening

To identify the mechanism underlying axial chromosome shortening, I used the microtubule perturbation assay to test whether microtubules were necessary. For this, the length of protruding arms was measured in mock-treated cells and compared to cells where anaphase microtubules were acutely perturbed with taxol or nocodazole. To optimize the 4D imaging and minimize phototoxicity, cells expressing EGFP-H2b only were used to follow chromosomes. In mock-treated cells, shortening of all 34 measured chromatids was completed within 14 min post-anaphase onset (Fig. 12 A, B) and proceeded at an average rate of ~0.6 ± 0.1 μm/min. By contrast, in cells where microtubules were acutely depolymerized by nocodazole after segregation of all sister telomeres, 29 of 36 (81%) measured chromosome arms failed to fully compact within the normal time of 15 min (Fig. 12 E, F) showing that polymerized microtubules were required for normal axial shortening.

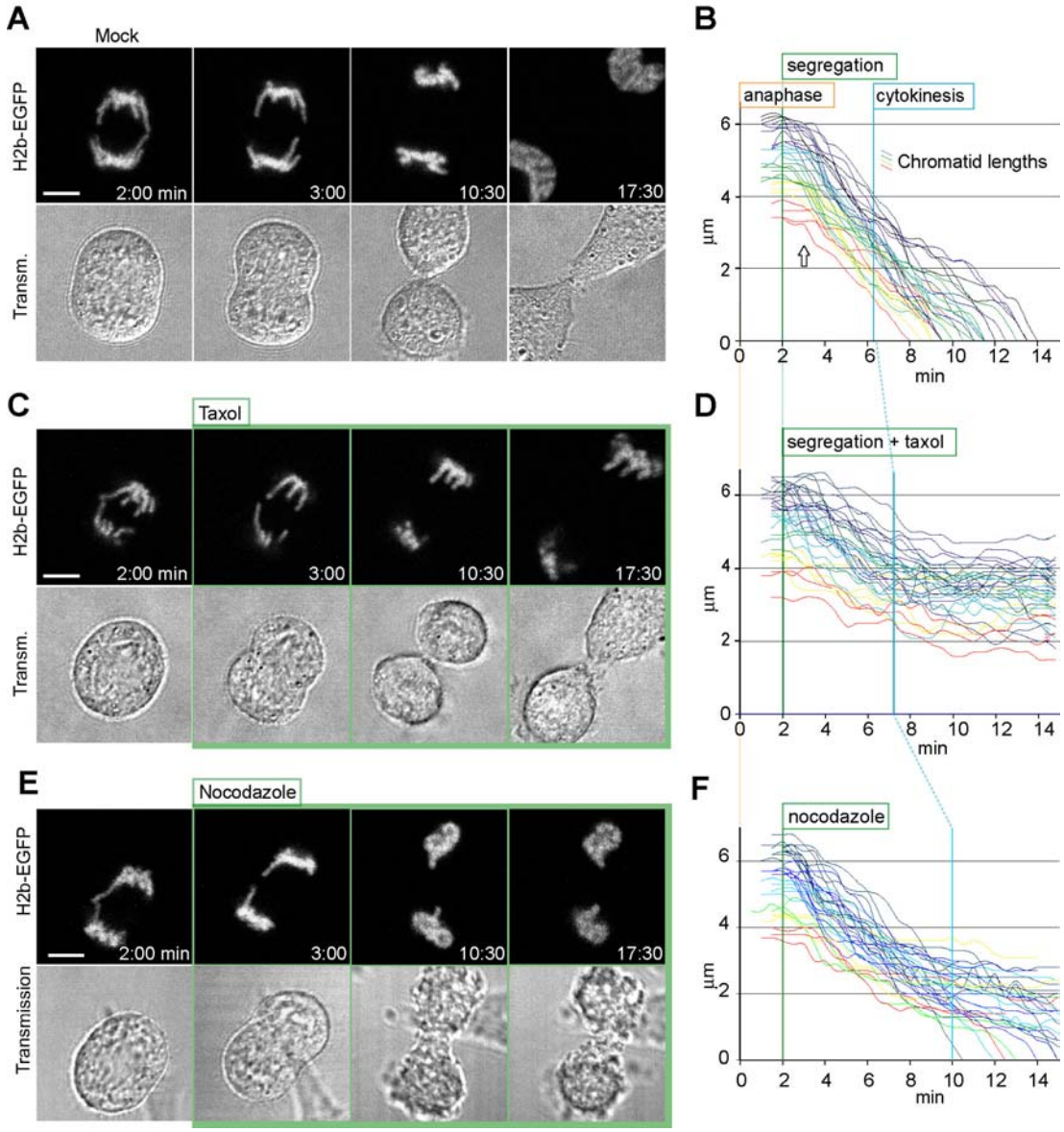

Figure 12. Dynamic microtubules are required for chromatid arm shortening in anaphase. The length of single protruding chromatid arms was recorded and measured as in fig. 7. Microtubule-perturbing drugs were added as described in fig. 11**. (A)** Representative cell of n=15 mock-treated cells from independent experiments, **(B)** Lengths of n=34 chromatid arm protrusions. In 31/34 chromatids (91%) the mean steady rate of shortening of 0.6 ± 0.1 µm/min is reached after a 0.5-1.5 min delay after full segregation (open arrow). **(C)** Representative cell of n=15 independent experiments where microtubules were hyperstabilized by taxol immediately after segregation of all sister chromatids (green frame). **(D)** Length of n=36 measured chromatid arm protrusions. Note normal chromatin poleward migration, decompaction and cytokinesis of taxol-treated cell, delayed substrate reattachment and formation of abnormal multi-lobed nuclei instead of smooth, round daughter nuclei. Every extra lobe was directly traced back in 4D confocal data sets to an incompletely compacted chromatid arm (Compare last EGFP-H2b frames in A & C, see also fig. 16 B, C)**. (E)** Representative cell of n=15 independent experiments as in (C) but where microtubules were acutely depolymerized by nocodazole. **(F)** Lengths of n=36 chromatid arm protrusions. Note the higher penetrance of the taxol phenotype, explained by the fact that 20 µM nocodazole could not depolymerize all anaphase microtubules -reported to be several-fold more stable than in metaphase (Zhai et al., 1995)- within 10-15 min, as we could still detect few microtubules by immunofluorescence (not shown). Therefore, some remaining microtubules may have been sufficient to participate in the compaction of some chromosomes, although slower than in controls. Bars = 5µm.

Then I asked whether the presence of microtubules in a hyperstabilized form would be sufficient to support axial shortening or whether dynamic microtubules were required. In cells where microtubules were rapidly stabilized by addition of taxol immediately after segregation of the last sister chromatids, all 36 measured chromosome arms failed to shorten normally (Fig. 12 C, D). While all these cells performed cytokinesis and chromatin decondensation with near-normal kinetics, and a delayed substrate reattachment, they failed to eventually form the smooth, round daughter nuclei that characterize an unperturbed mitosis. Instead, multi-lobed nuclei were formed, and each extra lobe could be directly traced back in 4D data sets to result from an incompletely shortened chromatid arm (Fig. 12 C; Fig. 16 B, C). This showed that the presence of dynamic microtubules is required for the axial shortening of chromosome arms in anaphase. The pleomorphic nuclear morphology in taxol treated cells furthermore suggests that shortening is required for the formation of smooth nuclei with normal chromatin architecture after mitosis.

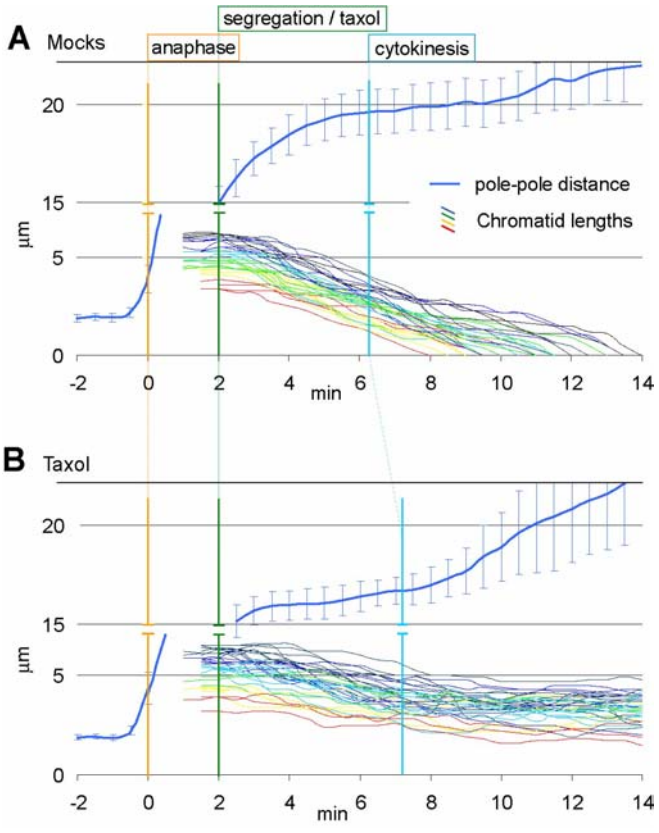

Figure 13. Single chromatids shorten independently of pole-pole separation of chromatin masses in anaphase. Measurements as in fig. 7. **(A)** Distance between chromatin masses migrating toward opposing poles of the daughter cells in 15 independent control cells (blue curve, see also fig. 7 C). The average separation rate between both chromatin masses before cytokinesis was 3.6 µm/min ± 0.52 µm/min (or 1.8 µm/min for the separation of a single chromatin mass from the equatorial plane of division). The mean shortenings of n=34 single chromatid segments (same as in fig. 12 B) reach a roughly-steady rate of 0.63 µm/min ± 0.11 µm/min, 3-4 min after anaphase onset. **(B)** Same measurements for cells where microtubules were hyperstabilized by taxol addition 2 min after anaphase onset, when segregation was complete segregation (chromatid segment shortenings same as in fig. 12 D). Bars = 5µm.

VI. 1.6 ii Aurora B activity may be required for shortening

The kinase Aurora B has been implicated in chromosome alignment and segregation (reviewed in Ducat and Zheng, 2004). To test for a potential additional role in chromosome shortening, the

specific inhibitor Hesperadin was acutely applied in a similar fashion to the nocodazole and taxol experiments above, to inhibit Aurora B activity immediately after segregation of all chromatids. Preliminary results have been encouraging. In 2 experiments, chromatid arm shortenings were abruptly stopped within 30 s of Hesperadin addition while mock treated cells showed no effect (Fig. 14). Furthermore, in the presence of Hesperadin, and in contrast to the nocodazole and taxol experiments, several protruding chromatid segments remained in the area of the cleavage furrow ingression until cytokinesis. These preliminary results suggest that Aurora B activity may be required for anaphase chromatid shortening and will be very interesting to pursue in my future work (see Discussion).

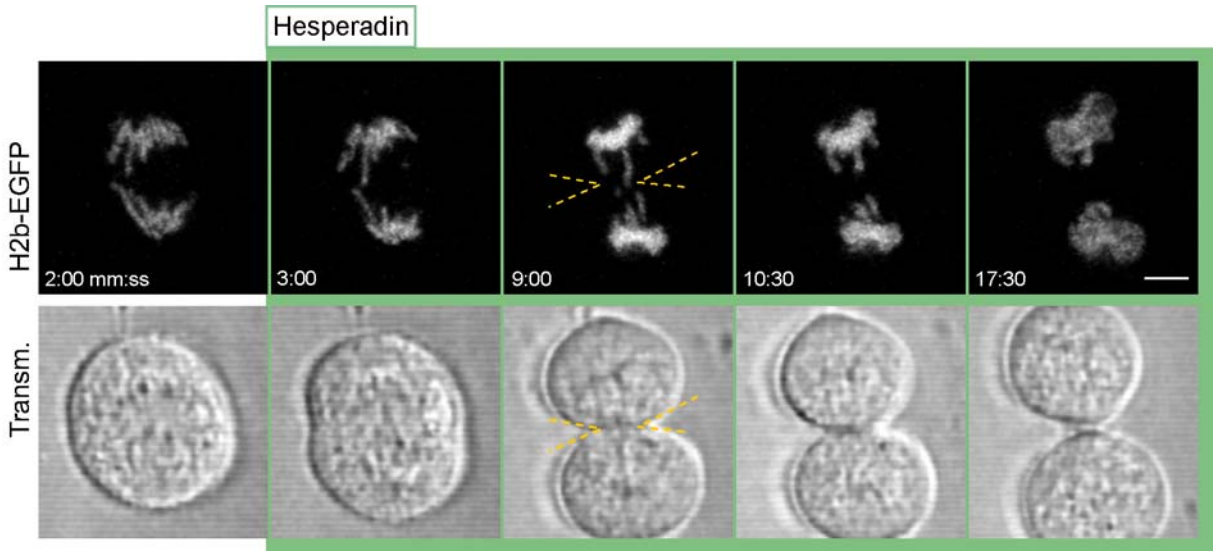

Figure 14. Aurora B may be required for anaphase chromatid shortening and chromosome integrity. 1 of n = 2 cells from preliminary independent experiments with Aurora B kinase activity perturbed by the specific inhibitor hesperadin immediately after segregation of all sister chromatids (green frame), several chromatid arms failed to shorten normally and some were prone to damage by staying in the path of the closing cytokinetic furrow (yellow dashed lines). Both cells performed chromatin poleward migration, decompaction and cytokinesis similar to controls (see fig. 12 A), but had a delayed substrate reattachment and formed abnormal multi-lobed nuclei, as in the experiments in fig. 12. Bars = 5µm.

VI. 1.6 iii Condensin depletion does not affect shortening

Condensins have been shown to participate in anaphase shortening of rDNA loci in budding yeast (D'Amours et al., 2004; Lavoie et al., 2004; Sullivan et al., 2004) and previous work in the group has shown that condensin I is enriched on chromosomes during anaphase in mammalian cells (Gerlich et al., 2006). Therefore, to test whether condensins are required for axial chromatid arm shortening, I used a well established RNAi depletion assay of the shared condensin I and II

subunit SMC2 (Gerlich et al., 2006; Hirota et al., 2004). In HeLa cells stably expressing H2b-EGFP transfected with control siRNA, axial shortening of protruding chromatids proceeded similarly as in the NRK control cells (compare figs. 12 B & 15 B). In condensin depleted cells, the same phenotypes described previously were observed (Gerlich et al., 2006), namely a higher percentage of cells with segregation defects, such as anaphase bridges. However, again consistent with our previous observations, while most chromosomes appeared entangled in early anaphase, the majority of these segregation defects were eventually resolved and these chromosomes exhibited axial shortening with normal kinetics and total reduction in length (Fig. 15 C, D). These results strongly suggest that axial shortening of chromatids in anaphase can proceed independently of condensins. Strikingly, several chromatids whose segregation was initially severely impaired were rescued (Fig. 15 C, open arrow heads) in the absence of significant poleward movement of the chromatin masses (fig. 15 C, red horizontal dashed lines). This strongly suggests that mechanisms other than poleward pulling of centromeres mediated this rescue.

VI. 1.7 Acute perturbation of chromatid shortening impairs rescue of segregation defects in condensin-depleted cells

To test whether chromatid arm shortening could function as a mechanism to rescue chromosome segregation defects, condensin-depleted cells were used as sensitized background with a high frequency of segregation defects. In these cells, arm shortening was acutely inhibited by the microtubule perturbation assay described above and the number of segregation defects remaining at the moment when the cytokinetic furrow starts to cleave the cell was counted (Fig. 15 A). In n = 14 mock-treated/mock-depleted cells, no defects were detected. Similarly, in taxol-treated/mock-depleted cells, 1 defect in n = 13 cells was detected (0.08 ± 0.28 defects per cell). In n = 17 mock-treated/SMC2-depleted cells, we observed a 2-3 min delay in anaphase segregation compared to cells treated with control siRNA (Fig. 15 B, D) and we counted 1.7 ± 1.0 segregation defects per cell that could not be resolved before cytokinesis onset (Fig. 15 C, filled arrows) consistent with previous observations from the group (Gerlich et al., 2006). To test if microtubule-dependent shortening was involved in segregation, taxol was applied 3-5 min after anaphase onset, when the two chromatin masses were separated by at least the distance at which all chromatids are segregated in control siRNA treated cells. In condensin-depleted cells, this distance is reached 1-3 min later than in control cells, presumably due to the massive entanglement of chromosomes in early anaphase (Fig. 15 C). In n = 14 taxol–treated/condensin depleted cells, 5.3 ± 1.6 segregation defects per cell were counted, a more than 3-fold increase

compared to mock-treated/condensin-depleted cells (Fig. 15 E, F). This data suggests that microtubule-dependent axial shortening of chromosomes contributes to the rescue of anaphase bridges and other segregation defects, before the cytokinetic cleavage furrow "cuts" them, leading to unequal segregation.

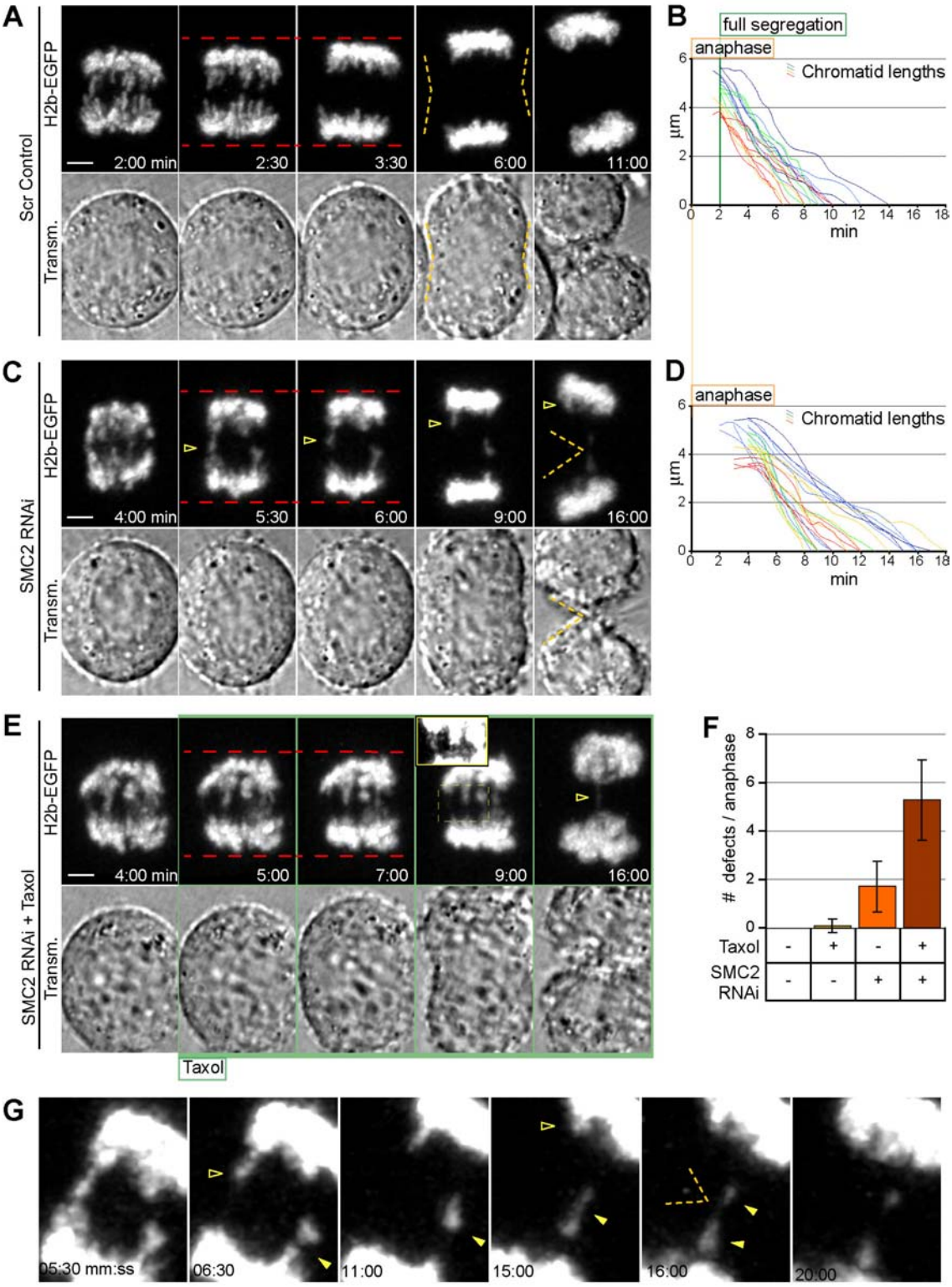

Figure 15 (prev.page). Rescue of segregation defects in condensin-depleted cells is impaired in cells where chromatid shortening is perturbed by microtubule poison treatment. Representative examples of n ≥ 13 cells from independent experiments. **(A)** Mock-treated/mock-depleted cell; yellow dashed lines highlight the cell contour curved by start of cleavage furrow ingression in cytokinesis. **(B)** Length of protruding chromatid segments over time in min (n = 20) in mock-treated/mock-depleted cells**. (C)** Mock-treated/SMC2-depleted cell; note that most chromatids eventually shorten and chromatin displays near-normal compaction after 9-10 min. A late bridge is rescued (open arrow heads) without significant poleward movement of chromatin masses (red horizontal dashed lines). A non-rescued lost chromosome is cut in two fragments of different size by the cytokinetic furrow (see full arrow in **(G)** non-rotated zoom-in; furrow outlined by orange dashed lines). **(D)** Length of protruding chromatid segments over time in min (n = 23) in mock-treated/SMC2-depleted cells; note the 2-3 min delay in shortening starts, due to a typical overall anaphase delay in condensin-depleted cells. **(E)** Taxol-treated/SMC2-depleted cell. At least 5 segregation defects persist when cleavage furrow starts ingression (zoom-in shows 2 additional bridges detectable by contrasting), and one persists even after full cleavage (open arrow head). **(F)** Mean number of segregation defects when cleavage furrow ingression starts (See A). In mock-treated/mock-depleted cells, no defects detected. In taxol-treated/mock-depleted cells, 1 defect in 1 cell detected (0.08 ± 0.28 defects/cell). In mock-treated/SMC2-depleted cells, 1.7 ± 1.0 defects/cell detected. In taxol–treated/condensin depleted cells, 5.3 ± 1.6 defects/cell detected.

VI. 1.8 The reduction of global chromatin volume in anaphase depends also on dynamic microtubules

To confirm that the anaphase arm shortening was responsible for the global compaction of chromatin observed with the volumetric assay, the kinetics and drug sensitivity of both assays were compared. Both phenomena occurred at exactly the same time and with concordant kinetics (Fig. 16 E). To test if the reduction of chromatin volume was equally sensitive to microtubule perturbation as the axial shortening, the high-resolution 4D imaging assay (Fig. 6) was used at the highest temporal resolution compatible with normal mitosis between metaphase and telophase (18 optical sections of 512*512 pixels, xyzt resolution: 0.06*0.06*1.5 μm*2min). The chromatin volume was then compared between control cells and cells were taxol was added immediately after the completion of chromosome segregation (Fig. 16). In mock-treated cells, anaphase compaction levels were consistently higher than in metaphase, similar to the observations at lower time resolution for entire mitosis (compare Fig. 16 D and zoom-in of metaphase to telophase in Fig. 6 C, plotted with the same scale and normalization as in 6 B). However, in taxol-treated cells, anaphase compaction above metaphase levels was abolished (Fig. 16 D). Therefore, microtubule-dependent axial shortening of chromosome arms directly explains the maximal reduction in chromatin volume observed in anaphase.

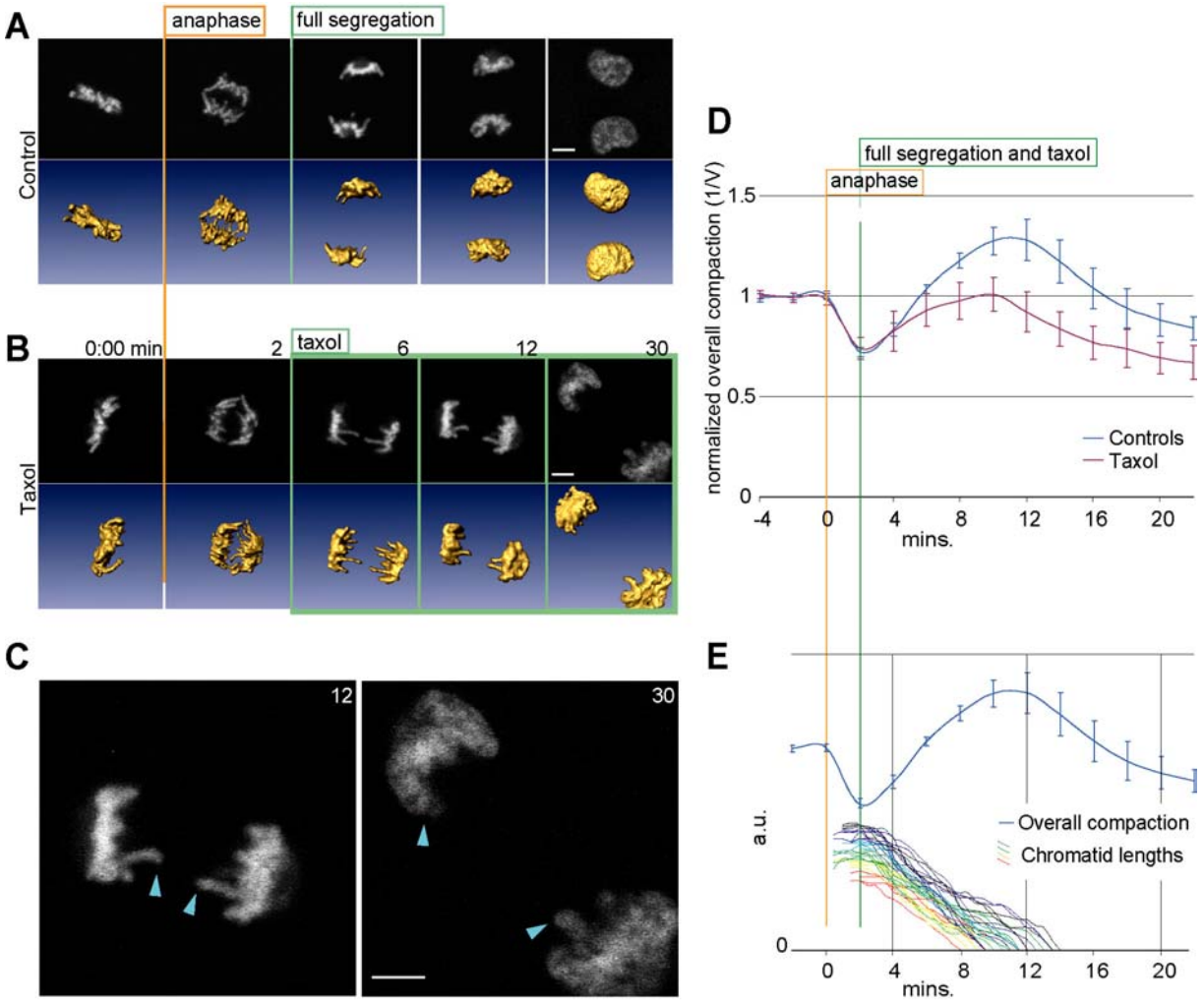

Figure 16. Large-scale anaphase compaction occurs simultaneously with single chromatid shortening and is also dependent on dynamic microtubules. **(A-D)** Same assay as described in fig.6, but with higher temporal resolution (time lapse = 2 min) and between metaphase and telophase. **(A)** Chromatin volume measurement in n=10 mock-treated cells from independent experiments, and **(B)** in n=10 taxol-treated cells from independent experiments. **(C)** Zoom-in of last two images of (B), abnormal poly-lobed daughter nuclei phenotype in taxol-treated cells. Each abnormal lobe was traced back to an uncompacted chromatid (arrow heads, see also 5 C). **(D)** Quantitations of volume measurement (compare controls in D and zoom-in of metaphase to telophase in Fig. 6 C). **(E)** The overall large-scale compaction of chromatin occurs during the same interval as all the individual axial shortenings of chromatids (same shortenings as in fig. 12 B), and with concordant kinetics. Bars = 5μm.

VI. 2 Additional Assays for Chromosome Compaction at Different Scales: Development and applications

VI. 2.1 A fluorescence distribution assay to measure compaction at medium scale

In prophase, when mitotic chromosomes form, the volumetric assay detects compaction 7-8 minutes before congression. However, careful visual examination indicates that prophase compaction may start even earlier. The reason is that the volumetric assay does not detect fine structural changes unless the surfaces of the structures can be segmented. Therefore, a quantitation of small-scale compaction was needed. For this, the distribution of pixel intensities in the chromatin region can be analyzed.

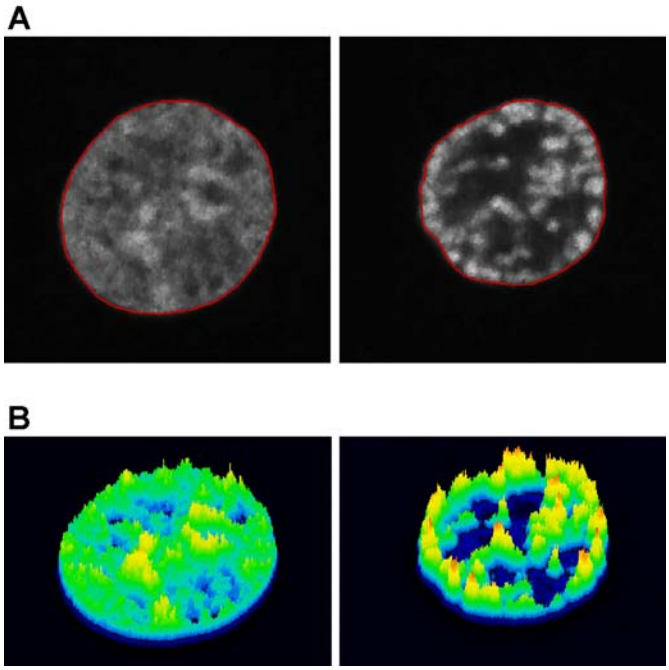

Figure 17. Chromosome compaction measured with the intensity distribution assay. (A) Single confocal sections of an NRK cell line stably expressing EGFP-H2b (described in figures 5 & 6), in interphase (left) and late prophase (right). The nuclear periphery can be delimited by the chromatin signal (red contours). **(B)** Same images where the intensity of each pixel is color- and height-coded; low intensities in blue-green and high intensities in yellow-red. The segmented chromatin signal changes from a relatively homogeneous distribution in interphase (most pixels green), to a much more inhomogeneous distribution in prophase (most pixels either blue or yellow-red). The standard deviation (SD) between pixel intensities increases proportionally to the increase in homogeneity, and thus to the increase in compaction, and is computed as described in Fig. 11 and sect. VI.1.5.

If, during compaction, chromatin density simultaneously decreases in some regions and increases in others, this will result in a more inhomogeneous fluorescence distribution (fig. 17). One simple

way to compute this is the standard deviation (SD) between the single pixel intensities. This assay has a resolution of ~200 nm and was originally developed in collaboration with Daniel Gerlich, formerly in our group, to analyze chromatin, but it was described in detail and used in a previous section to compare structured vs. soluble GFP-tubulin populations (Fig. 11; section. VI.1.5 and appendix 1). In short, homogeneous fluorescence gives a low SD, whereas inhomogeneous labeling produces a high SD. More heterogeneously distributed chromatin with a high SD can thus be used as an indicator that chromatin is locally more compact. To obtain results that can be compared over time, changes in the spatial distribution of fluorescence intensities should be consistently followed inside the same cellular compartment. Therefore, an area of measurement defined by an independent reference is needed, such as the nuclear periphery that surrounds all chromatin in this case.

VI. 2.2 Role of PNUTS in mitotic compaction probed with the fluorescence distribution assay

In collaboration with the group of Philippe Collas at the University of Oslo, I have started to investigate the potential role of PNUTS, a major *p*rotein phosphatase 1 *n*uclear *t*argeting *s*ubunits (reviewed in Ceulemans and Bollen, 2004), in the dynamic regulation of chromosome structure. In an *in vitro* nuclear assembly assay that mimics mitotic chromatin decondensation, recombinant PNUTS was shown to accelerate this decondensation (Landsverk et al., 2005).

To investigate the potential role of PNUTS on chromosome dynamics *in vivo*, PNUTS was depleted by siRNA in HeLa (Kyoto) cells stably expressing H2b-EGFP as chromatin marker (Fig. 19 A). A visual scoring of time-lapse images was then performed to count the time that each mitotic cell remained in mitosis, and in the different mitotic stages (Fig. 18). This assay did not reveal a major effect in the duration of telophase. In contrast, the average time between initiation of chromatin condensation in prophase and nuclear envelope breakdown was increased 3-fold in PNUTS depleted cells (n=89 cells; 60.1 ±3 8.4 min) compared to scrambled siRNA controls (n=102 cells; 20.1±6.8 min), $p<0.0001$. This quantitation was, however, limited by the accuracy of the visual determination of subtle changes in the structure and distribution of chromatin during the G2/M transition, and during the subsequent mitotic phases (But see section VI.3.1 below and appendix 2, for a development to improve this assay by automation).

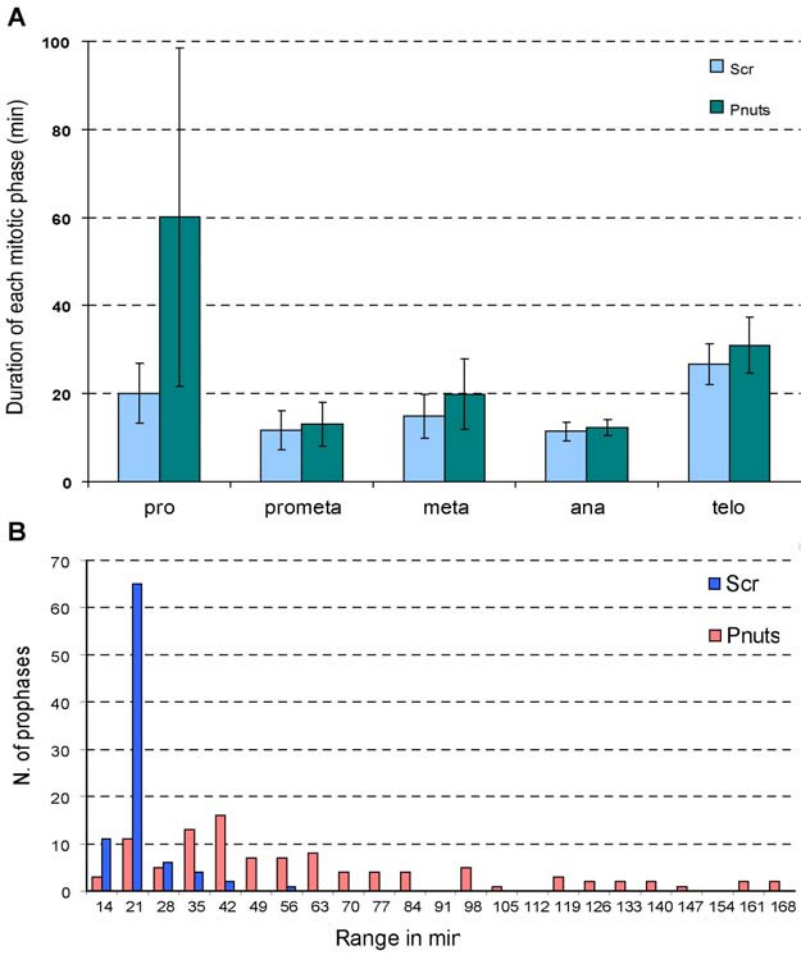

Figure 18. PNUTS depletion increases the time required for compaction during prophase (A) Durations of mitotic phases in PNUTS-depleted and control Scr cells (see fig 19). Prophase compaction lasts 60.1 +/- 38.4 min in n = 102 PNUTS-depleted cells (Green) compared to 20.1 +/- 6.8 min in n = 89 control (Scr) cells (Blue). PNUTS-depleted cells are also slightly delayed in the other mitotic stages. The large difference in prophase is statistically highly significant ($p<0.0001$), by both the Mann-Whitney U test and the t-test for independent samples with unequal variances. For the other mitotic phases the effects are small and may rather be caused by a general mitotic delay resulting from the strong prophase effect. Nevertheless, the differences in metaphase and telophase were likewise significant. For prometaphase and anaphase, the result depended on the statistic used and significance level chosen: $0.05 < p < 0.01$ for both phases in both tests. **(B)** Frequency distribution of prophase duration for Scr and PNUTS-depleted cells. 65 of 89 control cells require between 14 and 21 min to condense chromatin in prophase (median=18 min; 95% confidence interval (CI) = 18-21 min). By contrast, the distribution for PNUTS-depleted cells is much broader, with the highest frequency of cells (16 of 102) between 42 and 49 min (median = 48; 95 % CI = 42-56 min).

Therefore, to obtain an automated quantitation of the potential effect of PNUST in chromatin dynamics, the pixel intensity distribution assay previously described was then used to measure differences in the homogeneity of the chromatin signal in control vs. PNUTS-depleted cells (Fig. 19). This analysis suggested that the distribution of fluorescent chromatin in PNUTS-depleted cells, and thus the compaction state, started to progressively change as early a ~2.5 hours before

NEBD, as it was already ~5% more heterogeneous than in control cells increasing logarithmically as cells approached congression (Fig. 19 C).

Collectively, these results indicate that PNUTS is implicated in chromatin dynamics in mitosis, both *in vivo* and *in vitro*. Within the frame of this collaboration, I plan to pursue the investigation of the role of PNUTS in chromatin condensation.

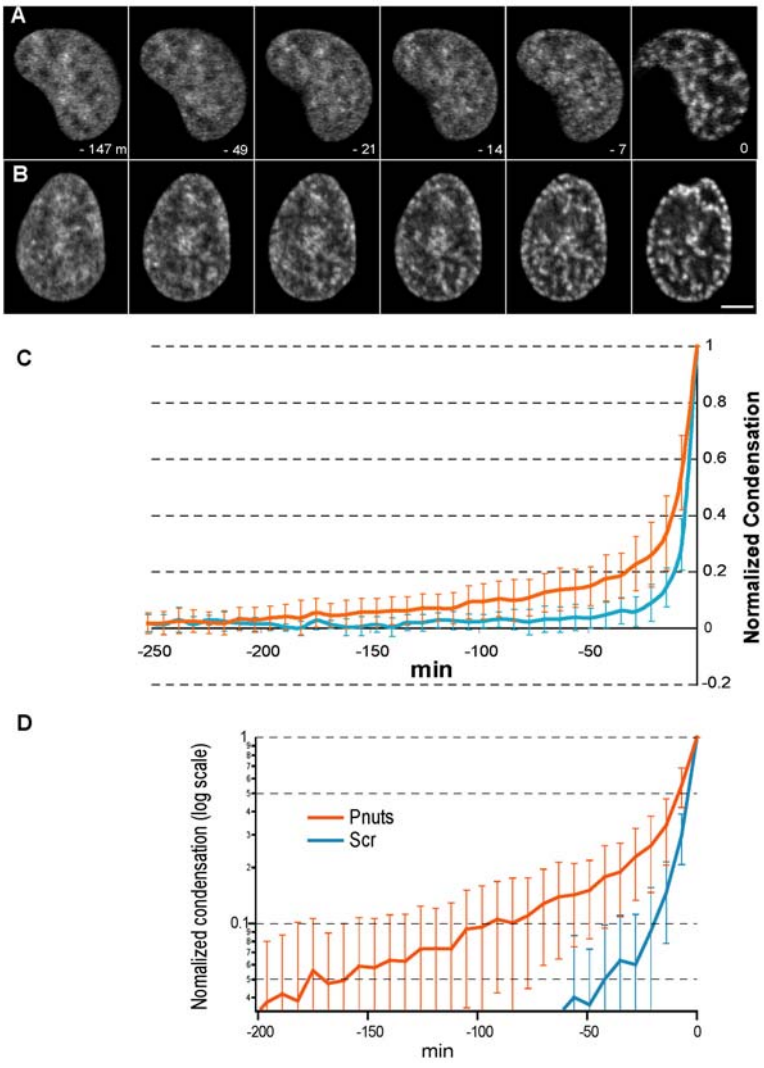

Figure 19. Depletion of PNUTS extends mitotic chromatin condensation in prophase. Subsets of individual cells used in fig. 18 were randomly selected to quantitate chromatin condensation using the intensity distribution assay (Fig. 11 and sect. VI.1.5). **(A,B)** Confocal sections of representative HeLa cells stably expressing H2b-EGFP and transfected with either control (Scrambled, or Scr) or PNUTS siRNA in 3 independent experiments. Chromosome congression is t = 0. **(A)** Scr cell from n = 89. **(B)** PNUTS-depleted cell from n = 102. **(C)** Mean normalized condensation kinetics for 14 Scr cells and 15 PNUTS-depleted cells. **(D)** The same data in semi-log scale in shows that, as early a ~2.5 h. before NEBD, chromatin in PNUTS-depleted cells is 5% more heterogeneous than in Scr cells, and 10% more heterogeneous 1.5 h. before congression. Interestingly, the abnormal condensation in PNUTS-depleted cells (lapse from 200 to 50 min before congression), follows single-exponential kinetics, suggesting a single rate-limiting step. Bar = 5µm.

VI. 2.3 Further development of the fluorescence distribution analysis

If the fluorescence distribution assay is to be used during the entire mitosis, without the limitation of having the nuclear periphery as boundary of measurement, the analysis strategy must then be modified. This can be done in two possible ways:

VI. 2.3 i Cellular periphery as SD measurement boundary

To obtain an intuitive and unbiased boundary of measurement, the cell periphery, delimited by the plasma membrane, can be used. A suitable segmentation of the fluorescence signal for the measurement requires data with a clear separation between the intensities corresponding mostly to the signal, and those corresponding mostly to the background. If the acquired gray values are optimally distributed along the entire dynamic range of the detectors, such a clear separation is possible, even in the case of mitotic chromatin, where the combination of intra-cellular autofluorescence and the small soluble histone pool gives a low but distinct signal above the extracellular noise. As mentioned, the segmentation threshold is then set interactively. Alternatively, the cellular periphery can be determined from transmitted light images of the cell and the SD can be calculated for all pixels within the cell. Importantly, with this approach, a homogeneity measurement of the cell is obtained that includes, but is not limited to chromatin. Also, the geometry of the cell, and therefore the area of measurement, changes dramatically during mitosis. This can influence the intensity distribution without being directly related to changes in the fluorescent chromatin. These limitations must be considered and reflected in the interpretation of the results.

VI. 2.3 ii Fluorescence intensity distribution analysis without thresholding

Alternatively to the SD measurement approach, a more mathematically rigorous analysis of the changes in fluorescence intensity distribution can be performed. Within an automated quantitation, an interactively-set threshold is the main potential source of bias, and if the thresholding step is eliminated, the bias is greatly reduced. Since thresholding is typically used to separate the signal of interest from the background, an alternative way to classify and separate the background signal was needed. Together with Aurélien Bancaud in our group, we are designing a strategy to quantitate changes in the fluorescence intensity distribution without using thresholds in the post-acquisition image processing.

Preliminary results indicate that fluorescence background behaves very similar to a Poisson distribution. Therefore, a Poisson function can be used to describe and subtract the background component from each intensity value in an image, regardless of its position. Preliminary results also indicate that this new set of Poisson-corrected values has a distribution that can be described with a combination of 2 Gaussian functions. Each of these functions describes subpopulations of intensity values that may reflect distinct states of chromatin compaction. A quantitative analysis of changes within and between each of these populations could provide a robust and unbiased description of chromatin compaction kinetics, in 3D datasets of all chromatin through mitosis, and without arbitrary thresholds. This strategy may thus become a powerful tool to detect medium and even small scale changes in the compaction state of chromatin. Furthermore, this analysis can be extended to study other cellular structures, for example the mitotic spindle (Fig. 20). Similarly to chromatin, a Poisson function can help to subtract the background component from each intensity value in an image. Preliminary results indicate as well that these Poisson-corrected values have a distribution that can also be described with a combination of 2 Gaussian functions. One function can describe the subpopulation of intensity values mainly given by the soluble tubulin, and the other function can describe the subpopulation mainly given by the polymerized microtubules. In addition, the integral of these functions may give a precise quantitation of the contribution of each population to the total tubulin fluorescence.

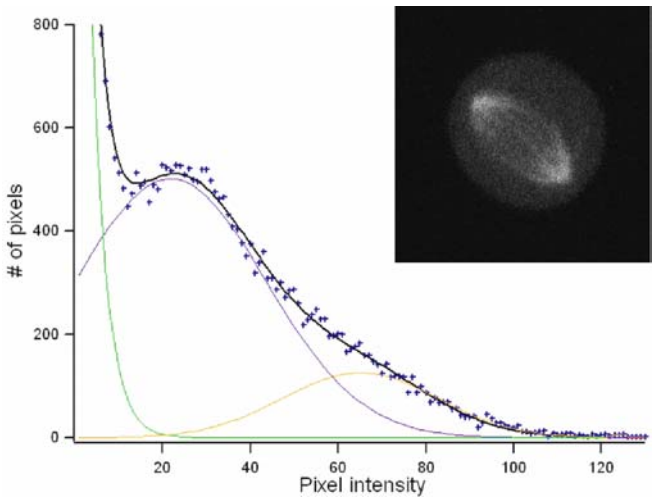

Figure 20. Threshold-less fluorescence distribution analysis. Pixel intensity distribution (blue crosses) in an early anaphase monoclonal NRK cell line stably expressing mEGFP-α-tubulin (inset). The mostly extra-cellular low intensities, coming primarily from detection noise, are fitted with a Poisson function (green curve). The largest fraction of intermediate intensities, coming mostly from depolymerized tubulin, is fitted with a 1st Gaussian function (purple curve). The largest fraction of relatively high intensities, coming mostly from polymerized tubulin in the mitotic spindle, is fitted with a 2nd Gaussian function (yellow curve). The combined fit is given by the black curve. Fitting implemented by A. Bancaud.

VI. 2.4 A FRET assay for chromosome compaction at the molecular scale

The molecular interactions that mediate chromosome compaction remain to be identified. Along this line, an *in vitro* assay has shown that the tails of the core histones may influence the condensation of mitotic chromosomes (de la Barre et al., 2001; de la Barre et al., 2000), and, in addition, the crystal structure of *X. laevis* nucleosomes shows a contact between the tail of histone H4 and an acidic patch in the H2a-H2b dimmer of an adjacent nucleosome. Importantly, this contact is absent in *S. cerevisiae,* in which mitotic chromatin is less compacted compared to higher eukaryotes. This suggests a higher-eukaryote-specific interaction (Luger et al., 1997; White et al., 2001). The *in vivo* relevance of such *in vitro* and crystallographic data remains to be determined but it suggests that core histones may play an important role in chromatin compaction.

To address this, a FRET-based assay was developed to obtain structural and molecular information on chromatin condensation in the context of the cell. Specifically, this assay was designed to probe the role that core histones may play, by looking for intra- and inter-nucleosomal interactions between fluorescently tagged histones. An exciting part of this approach was the possibility to follow such changes through the cell cycle. This was achieved by adapting the assay for *in vivo* measurements using time-lapse ratio imaging.

VI. 2.4 i A *bona fide* FRET-based intra-molecular reporter for the local nucleosome environment

In a first step, EGFP and tC-bound RaAsh (EGFP-tC/ReAsh; see methods) were identified as a good FRET pair within chromatin, as it showed relatively high FRET efficiency when tagged to H2b, by both the "acceptor photobleaching" and "spectral scanning" techniques. Cross talk between the spectra of EGFP and tC/ReAsh was controlled in cells expressing H2b-EGFP alone and H2b-tC alone. In this context, several favorable spectral properties make EGFP and ReAsh very suitable for FRET detection in live cells with ratio imaging.

- The excitation spectrum of EGFP has very little overlap with the excitation spectrum of ReAsh. Thus the cross-excitation of ReAsh with the laser-line used to excite EGFP (Argon 458 nm line in this work) is negligible.
- The overlap integral of the emission spectrum of the donor (EGFP) over the excitation spectrum of acceptor (ReAsh) is high, which promotes a high energy transfer between the two molecules.

- The emission spectrum of EGFP has little overlap with the emission spectrum of ReAsh. Thus the "leak-through" of EGFP emission onto the detection channel of ReAsh in a simultaneous detection mode can be minimal with a suitable combination of dichroic mirror and emission filters. Alternatively, a suitable setting of acquisition by spectral-scanning (Fig. 22) can be used, either with grating optics or an acousto-optical beam splitter (AOBS), as used in this work.

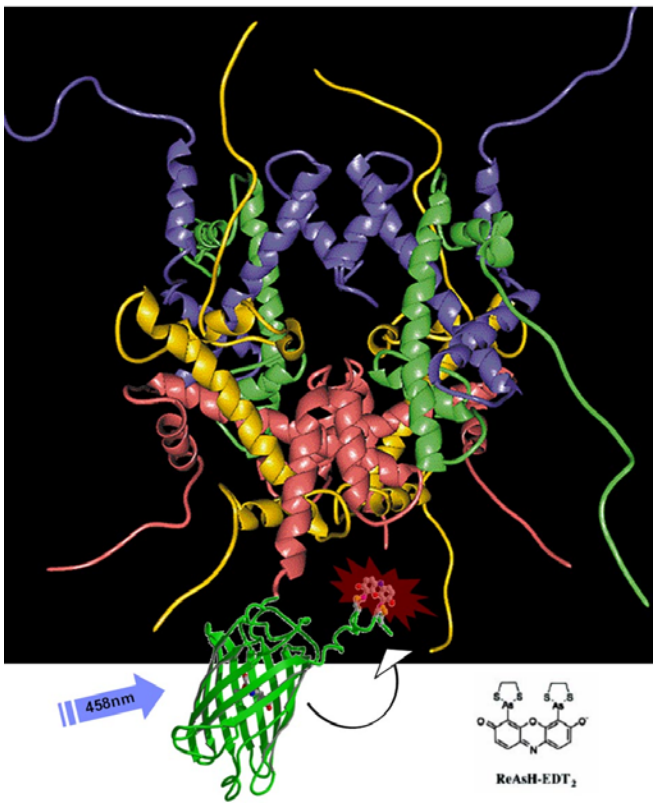

Figure 21. H2b-EGFP-tC/ReAsh FRET reporter for chromatin. An optimized tetra-cysteine (tC) motif was fused to the Carboxy-terminus of EGFP, fused in turn to the core histone H2b (red helix within the core nucleosome octamer; from K. Luger). The resorufin bi-arsenide derivative ReAsh –as FRET acceptor- binds non-covalently to the tC with high affinity. Upon EGFP –as FRET donor- excitation with a 458 nm laser (purple arrow), energy is transferred by resonance between both chromophores (arrow). This energizes ReAsh and results in emission of red light. (EGFP fusion and ReAsh molecule from R. Tsien)

VI. 2.4 ii Intra- and inter-molecular interactions between histone tails searched with FRET

The fusion H2b-EGFP-tC (Fig. 21) was used as positive control for FRET efficiency, measured directly in interphase chromatin and in mitotic chromosomes. The most efficient and therefore most used version of this chimera was the "new 2" (see materials), in which the H2b and EGFP sequences are followed by the motif -KFLF-tC-MEPLG (B. Martin, pers. com. See also Adams et al., 2002; Gaietta et al., 2002).

Surprisingly, using the "acceptor photobleaching" technique (see methods), the apparent FRET efficiency for this chimera was nearly 3-fold higher in metaphase chromosomes than in interphase

chromatin (13,2% ± 6.8% vs. 33,9% ± 5,1%; images not shown), strongly suggesting that the CHO-terminal of H2b may undergo conformational changes or compactions that increase the proximity of fluorophores. Therefore, the H2b-EGFP-tC/ReAsh fusion is a *bona fide* reporter of the density of the nucleosomal environment and may report on molecular–scale changes in chromatin compaction.

Potential inter-molecular interactions between histone tails were search by monitoring apparent FRET efficiencies with the acceptor photobleaching technique in cells expressing several combinations of core histone chimeras. Apparent FRET efficiencies were compared between interphase and metaphase. Unfortunately, none of these combinations gave a signal that was significantly above background levels, neither in interphase nor in metaphase. Thus, no inter-molecular FRET could be detected between core histones.

Combinations of core histone chimeras tested for inter-molecular FRET

H2b-H2b	H2b-H2a	H2b-H3	H2b-H4*	H2a- H3	H2a-H4	H3-H4
H2b-EGFP + H2b-tC	H2a-EGFP + H2b-tC	H2b-EGFP + H3-tC	H2b-EGFP + H4-tC	H2a-EGFP + H3-tC	H2a-EGFP + H4-tC	H3-EGFP + H4-tC
EGFP-H2b + H2b-tC	H2a-EGFP + tC-H2b	H2b-EGFP + tC-H3	H2b-EGFP + tC-H4	H2a-EGFP + tC-H3	H2a-EGFP + tC-H4	H3-EGFP + tC-H4
EGFP-H2b + tC-H2b		H2b-tC + H3-EGFP	H2b-tC + H4-EGFP			H3-tC H4-EGFP
H2b-EGFP + tC-H2b		tC-H2b + H3-EGFP	tC-H2b + H4-EGFP			tC-H3 H4-EGFP
		H2b-EGFP + tC-H3	H2b-EGFP + tC-H4			
		EGFP-H2b + H3-tC	EGFP-H2b + H4-tC			

*For the H2b-H4 combinations, different linker lengths between the histone and the fused tC motif were tested (see materials).

VI. 2.4 iii An in vivo FRET assay for compaction

The "Acceptor photobleaching" technique is limited in that it can only be performed one time on the same sample, since the acceptor fluorophore is irreversibly destroyed. Therefore, the assay was adapted and optimized to record changes in FRET efficiency in live cells, in real time (see methods). The sensitized emission of the acceptor was recorded by the non-bleaching technique of "wavelength" or "spectral scanning", through the cell cycle, using the positive intra-molecular FRET reporter H2b-EGFP-tC/ReAsh (Fig. 22). Relative FRET efficiencies were then calculated and compared by ratio-imaging (eq. 3 sect. VIII.2.4)

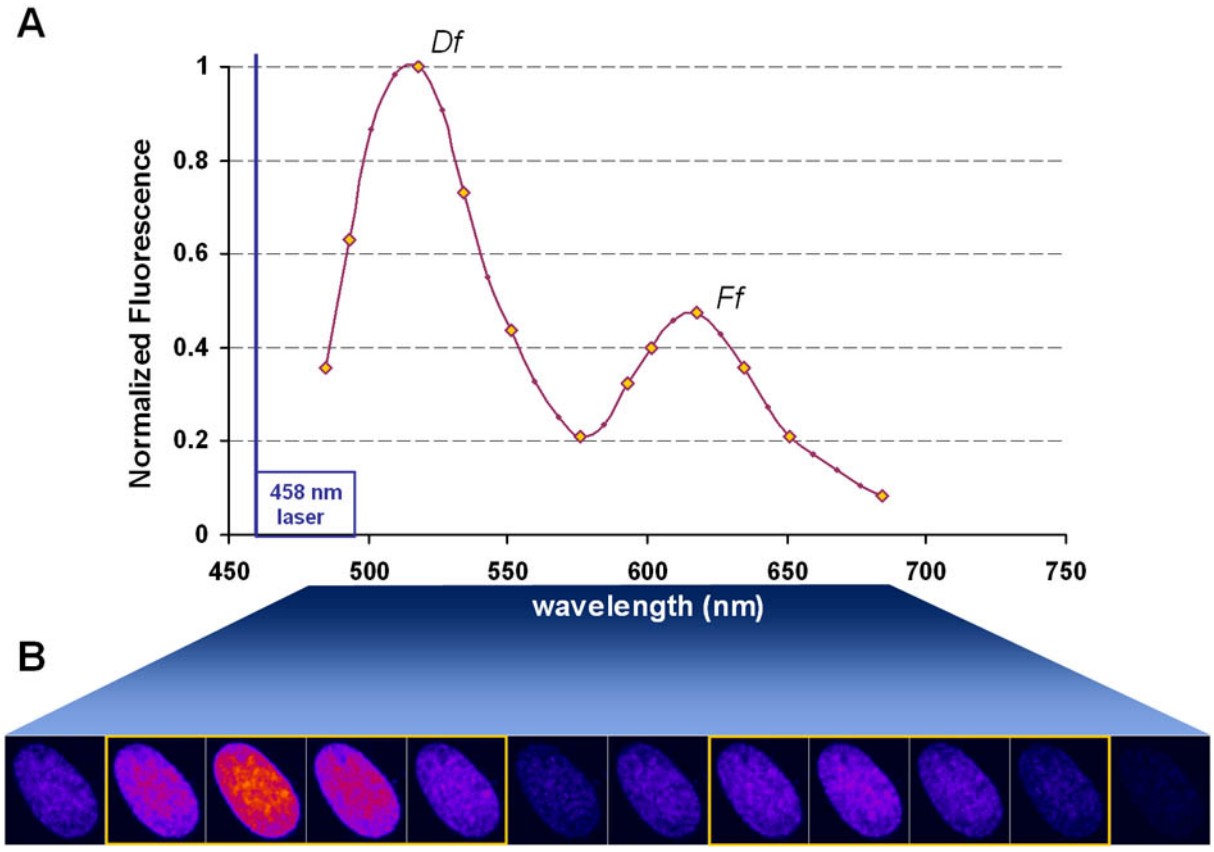

Figure 22. Emission spectral scanning of the H2b-EGFP-tC/ReAsh FRET reporter. (A) Upon 458 nm laser illumination, the emission spectrum of the chromatin FRET reporter described in fig. 21 can be recorded by sequential scanning of defined spectral windows, using an AOBS system (Leica Microsystems, Mannheim). Optimal spectrum regions for detection of the donor fluorescence signal (*Df*) and acceptor sensitized emission signal upon FRET (*Ff*) can be identified and used for ratio imaging (see eq. 3; sect. VIII.2.4). **(B)** NRK cell line with incubated ReAsh bound to the transfected H2b-EGFP-tC FRET reporter. Low fluorescence intensities coded in blue-violet, high intensities coded in red-orange. Typical windows used for optimal detection were thus 495-550 for *Df* and 600-675 for *Ff* (yellow frames).

Imaging conditions to minimize phototoxicity with the ReAsh were optimized for detection of FRET with minimal phototoxicity. A single excitation with the 458 nm laser line was used per time point, and the emission was split toward two detection channels, either with suitable dichroic mirrors and emission filters or with an AOBS. Using simultaneous detection, the EGFP fluorescence was obtained in one defined spectral window (typically 495-550 nm), and the ReAsh fluorescence produced mostly by the FRET in another spectral window (typically 600-675 nm) (Fig. 22). The ratio between the FRET channel and emission channel was used as a relative quantitation of FRET.

From metaphase to anaphase the ratio FRET was maximal, likely reflecting an increased fluorophore proximity caused by a reduction in the space between the fluorophores during chromatin condensation. During telophase, a gradual decrease of FRET is seen until a baseline level is reached and maintained during interphase (Fig. 23). Thus, this *bona fide* FRET reporter can be used to measure relative compaction changes in mitotic chromatin in live cells.

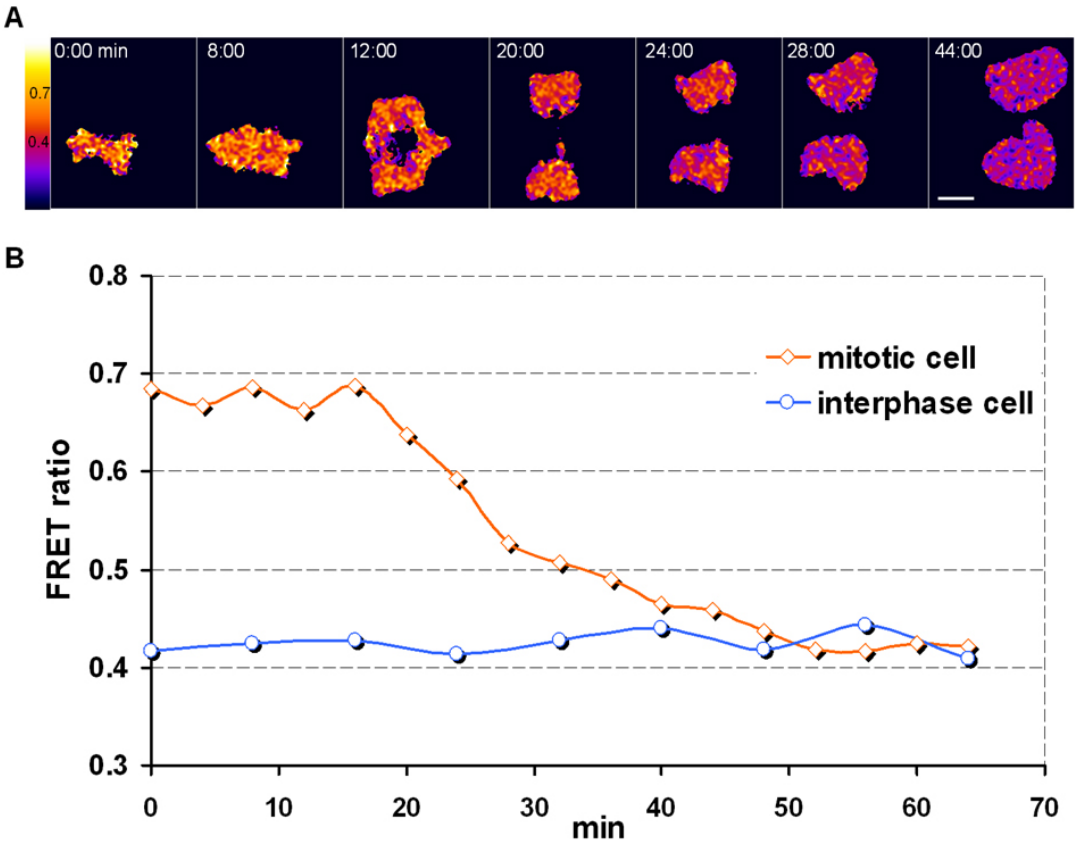

Figure 23. FRET levels correlate with metaphase-to-telophase chromatin compaction levels. (A) Cells, Fret reporter and color coding as in fig. 22 but in mitosis, from metaphase to telophase end. **(B)** Ratiometric FRET (see eq. 3 in sect. VIII.2.4) is high in metaphase and anaphase, and decreases during telophase (orange curve). An interphase cell shows a constant level of FRET during a similar time-lapse (representative cells of n = 5 for each). Time-lapse = 4 min. Bar = 5µm.

Preliminary time-lapse FRET imaging sequences during an entire cell cycle confirmed that baseline FRET efficiency in interphase increases only in mitosis and decreases again at mitotic exit (Fig. 24). However, these measurements were challenging, since most cells imaged before mitotic entry did not proceed to mitosis. This is likely a result of the high sensitivity of cells in early mitosis to the phototoxicity caused by the imaging and the radical production of the tC-bound ReAsh upon illumination

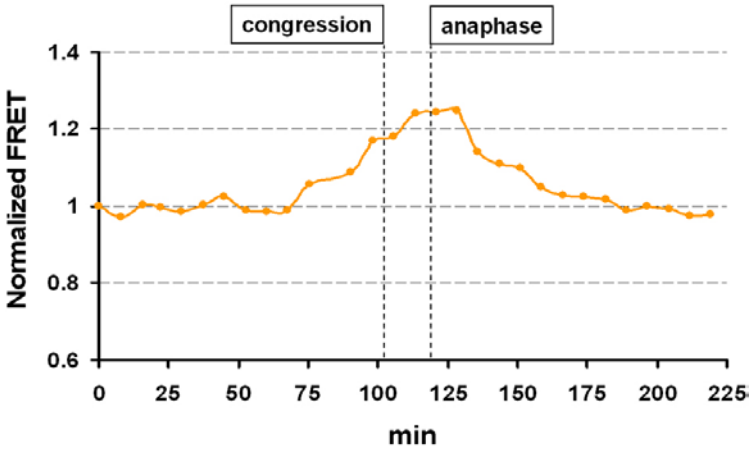

Figure 24. FRET levels correlate with chromatin compaction levels through mitosis. Preliminary FRET recordings as in fig. 23, but of entire mitosis starting in G2 (n = 2). Time-lapse = 8 min. Bar = 5µm.

VI. 3 Additional Results on Chromatin Organization

VI. 3.1 Automated recognition, tracking and analysis of mitotic cells

Appendix 2. As mentioned in the section VI.2.2 on PNUTS, the visual quantitation of structural changes in chromatin has limited accuracy and a low through-put. To address this, an assay for the automated segmentation, tracking and classification of fluorescently-labeled nuclei in large, multi-dimensional imaging datasets is being developed in collaboration with Nathalie Harder, Karl Rohr and Roland Eils at the DKFZ Heidelberg, and within the frame of the MitoCheck project (Harder et al., submitted; appendix 2). The ultimate aim of this approach is the quantitative analysis of mitotic progression in unperturbed and perturbed cells, in combination with the RNAi depletion and/or pharmacological inhibition of potential mitotic factors (Neumann et al., in the press). For this, such an automatic classification tool can be combined with other types of analysis made, for example, with the assays presented in the previous sections. The definition of the strategy and parameters to classify and analyze mitotic phases and potential phenotypes, as well as the entire primary imaging data used in the manuscript in Appendix 2 are part of this project.

VI. 3.2 Dynamics of Chromatin Proteins

Appendix 3. At the end of mitosis, the rod-shaped chromosomes in daughter cells decompact anisometrically (Heitz, 1928; Hiraoka et al., 1989; Manders et al., 2003). The remaining different levels of density have been used to define types of interphase chromatin, such as eu- and heterochromatin (see introduction). The establishment, maintenance and organization of such types of chromatin remain poorly understood, despite their functional importance (reviewed in Grewal and Elgin, 2002). The histone methyltransferase SUV39H1 and the heterochromatin protein 1 (HP1) have been identified as mayor players in the organization of interphase chromatin. Also, the linker histones H1 may play an important role in chromatin organization. In collaboration with Joël Beaudouin, formerly in our group, the contributions of interactions and diffusion to the mobility of these proteins were analyzed; the results were published in Beaudouin et al., (2006).

The generation and initial analysis of the localization and mobility of the fluorescently-tagged versions of these proteins, and the establishment of conditions for their final analysis in the publication in Appendix 3 are part of this project.

VII Discussion

VII. 1 Applying Chromosome Compaction Assays

VII. 1.1 Limitations of measuring chromosome volumes in live cells by confocal microscopy

The volumetric imaging assay employed here has the power to detect large-scale changes in the compaction of all chromosomes in the cell. For this, automated 4D confocal microscopy of live cells stably expressing GFP-H2b was combined with an image processing protocol that preserve edges and small features. Also, the quantitations were performed in a mostly automated and thus unbiased way. The one aspect not automated was the interactively chosen threshold, set to best separate chromatin from background. The possibility that some bias could remain in the threshold choice is not ruled out. Nevertheless, this was set in metaphase, when chromosomes are very compacted and evenly aligned and therefore easiest discriminated form the background. A systematic readout of the kinetics of compaction from interphase and through mitosis was thus obtained.

The interpretation of the assay is also limited by the anisotropy and spatial resolution of conventional confocal microscopy, combined with the maximal signal-to-noise ratio and temporal and spatial resolution compatible with unperturbed progression from G2 through mitosis of the cells under observation (see "Phototoxicity" section VIII.2.4). In mammalian cells with many chromosomes, this limited spatial resolution made it difficult to distinguish if the reduction in global chromatin volume resulted from increased compression between different chromosomes or from compaction of single chromosomes. Nevertheless, our high temporal resolution analysis of single chromosome arm lengths by multicolor 4D imaging and photoactivation during anaphase established a clear kinetic correlation between global volume reduction and a mechanism of axial shortening of chromatids in anaphase, both of which exhibited identical sensitivity to acute microtubule perturbations. This unambiguously showed that axial shortening of individual chromosomes is responsible for the maximal compaction.

VII. 1.2 Comparison of the volumetric and intensity distribution assays

The volumetric and intensity distribution assays presented in the previous section measure compaction at levels that probably overlap, one with ~800 nm and the other with ~200 nm resolution. This means that the scale of dimensional changes from the level of entire chromosomes to intermediate fibers of 100-200 nm are potentially covered when both assays are combined.

Figure 25 shows the same dataset analyzed with both methods. The volumetric assay efficiently reports on large-scale changes in chromosome compaction throughout mitosis. In prophase, when mitotic chromosomes form, the volumetric assay detects compaction 7-8 minutes before congression. However, careful visual examination indicates that prophase compaction may start earlier. The reason is that the volumetric assay does not detect fine structural changes unless the surfaces of the structures can be segmented. By contrast, the fluorescence distribution assay that measures the level of homogeneity of chromatin by calculating the SD between pixel intensities, detects compaction as early as 15 min before congression (Fig. 25 B, orange frame), confirming and quantitating the intuitive visual assessment.

It must be noted that conformational changes in chromatin could in principle contribute to local changes in homogeneity, without necessarily resulting in significant compaction. However, density changes between prophase and other stages have been quantitated here and in other studies (Swedlow et al., 1993a). Thus, with the knowledge that compaction does increase in prophase, the fluorescence distribution assays can be used to contribute a finer read-out in early prophase.

The SD assay requires the same boundary of measurement over time to generate comparable results. In the case of microtubules, this boundary was given by the cell periphery, within which the tubulin fluorescence is contained. In the case of chromatin it is the nucleus that contains the chromatin fluorescence. However, when the nuclear envelope disassembles and chromosomes congress to the metaphase plate, this boundary disappears and the region of measurement can hardly be set in unbiased fashion. Thus, the SD assay is well suited to report on chromatin compaction as long as the nuclear boundary is defined. Afterwards, the volumetric assay becomes more advantageous, as the measurement can be carried through mitosis. The fluorescence distribution assay is currently being further developed to circumvent the limitations described here with promising preliminary results (see results, VI.2.3). This comparison illustrates the power

of combining two different but complementary assays to quantitate chromosome structural dynamics in intact cells.

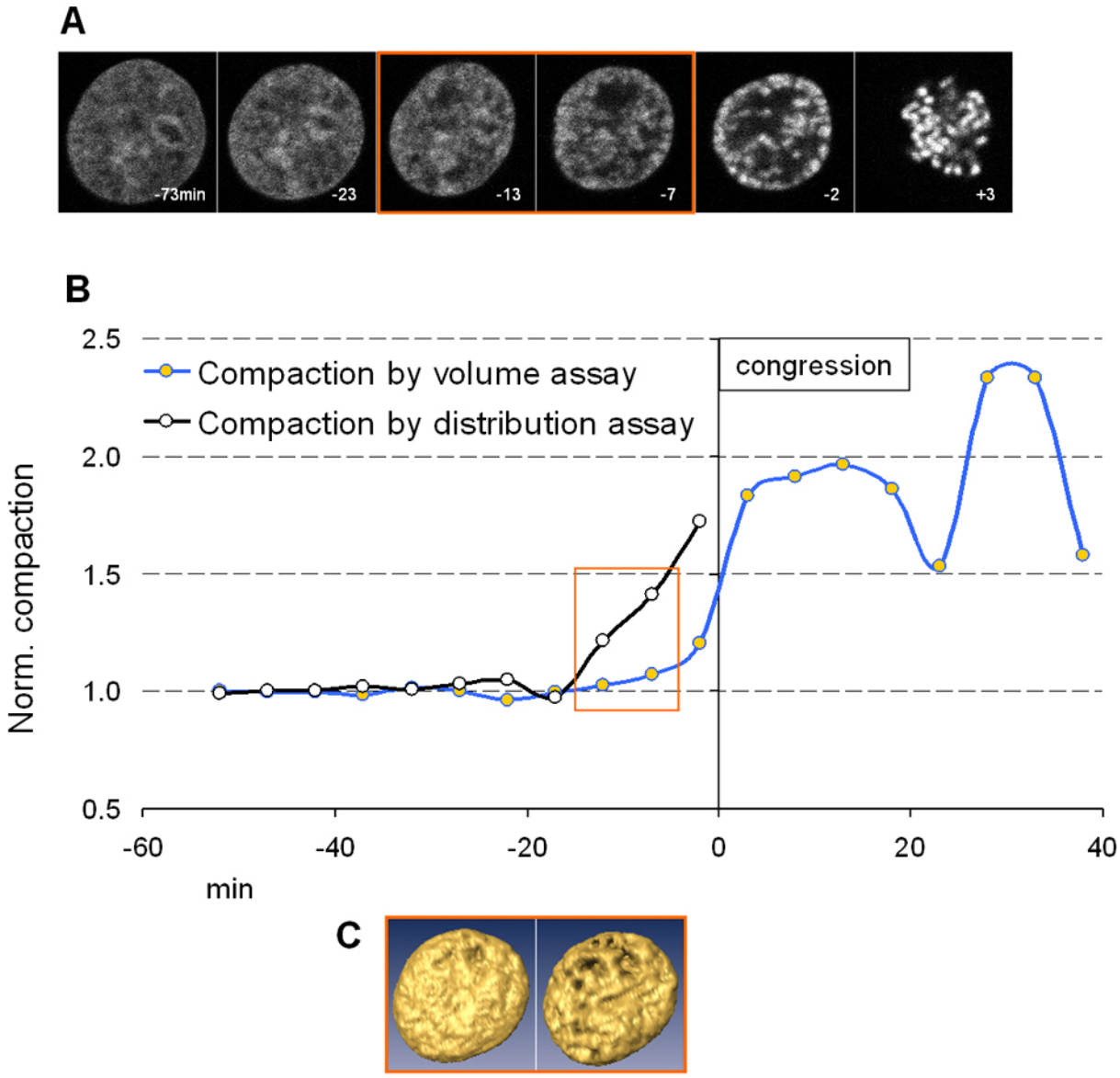

Figure 25. Volumetric vs. Intensity distribution assay to measure chromatin compaction at different scales. (A) Confocal sections of the monoclonal NRK cell line stably expressing EGFP-H2b. T = 0 is chromosome congression. **(B)** Normalized compaction calculated with the volumetric assay **(C, also fig 6)** and intensity distribution assay (figs. 11 and 17). Orange frames in A and B show the prophase stage and the respective quantitation by both assays in (B).

VII. 1.3 The quantitative study of the PNUTS-PP1 system may reveal key aspects of chromatin organization

By using the fluorescence intensity distribution assay, the depletion of the major PP1 nuclear targeting subunit PNUTS was shown to severely extend the time required to compact chromatin before prometaphase congression. This effect appeared to be specific to prophase, as the other mitotic phases were little or not extended compared to control cells. In this respect however, the prophase is usually defined morphologically as the mitotic stage when chromatin starts to condense and, in our quantitative assay, as the time when the intensity distribution of chromatin becomes significantly more heterogeneous than in interphase (Figs. 18, 19). This data is therefore consistent with two alternative interpretations. (i) PNUTS-depleted cells have a slower condensation in an extended prophase, or (ii) PNUTS-depleted cells initiate condensation prematurely, already in G2, and then complete it during prophase. To distinguish between these alternatives, the condensation analysis in live-cell RNAi experiments will be complemented with cell-cycle markers, such as PCNA or cyclin A and cyclin B in my future work.

Interestingly, the PP1 phosphatase has been proposed as a regulator of the mitotic H3-S10 phosphorylation by the Aurora B kinase, which has been linked to mitotic chromatin condensation (Hsu et al., 2000; Murnion et al., 2001). Thus, a plausible hypothesis is that chromatin targeting of PP1 through PNUTS may prevent premature histone phosphorylation by counteracting Aurora activity. The absence of PNUTS may therefore trigger premature compaction, while its added presence *in vitro* would simulate decompaction. It is thus of great interest to investigate the role of PNUTS in chromatin organization. As a start, and since the published data on the cell cycle localization and dynamics of PNUTS and PP1 is incomplete, a detailed analysis of the subcellular localization of fluorescently-tagged versions of these proteins in live cells, correlated to quantitative measures of chromatin de/condensation established here, will be revealing. Then, the functional aspects of the PNUTS-PP1 system will be further investigated. For this and in the light of the RNAi depletion phenotype described in this work, additional "rescue" experiments with exogenous PNUTS will be performed to confirm its role in prophase chromatin organization, and this will be extended to its interaction partner PP1. Furthermore, the mechanism by which the PNUTS-PP1 system potentially regulates chromatin structure will be investigated by analyzing the potential interplay with the Aurora B kinase in regulating mitotic histone phosphorylation, taking advantage of the specific Aurora B inhibitor

Hesperadin. Furthermore, a possible link between the activity of PNUTS-PP1 in the nucleus and the activity of the condensin complexes during prophase compaction will be investigated.

VII. 1.4 Comparison of the volumetric and time-lapse FRET assays

The volumetric and FRET assays measure compaction at very different levels, one at ~800nm, and the other at ~10nm. This means that events happening at the scale of large chromatin fibers and entire chromosomes are in the reach of the volumetric assay, whereas events at the scale of the nucleosome are in the reach of the FRET assay. Therefore, the potential overlap between both is very small at best and makes it difficult to directly compare them. Moreover, a rigorous interpretation of the FRET assay read-out requires structural knowledge of how the conformation of the reporter attached to H2b may change during compaction, in the context of a native chromatin fiber. Unfortunately, this knowledge is unavailable and very challenging to obtain.

Figure 26 shows results obtained with both assays from metaphase to telophase, albeit from different cells in independent experiments. As expected, both sets of results show a relatively high level of compaction in during metaphase and anaphase, and a decrease during telophase (Fig. 26 A). As described in the first part of this work, the large-scale volumetric assay reports a decompaction of chromosomes during segregation (Fig. 26 B), followed by a recompaction in late anaphase. However, the FRET results suggest that, at the molecular level, the nucleosome environment remains similar during metaphase and anaphase (Fig. 26 C).

Based on the scale of events that both assays can report on, an interesting possibility is that each assay detects different phenomena that occur at different scales. The FRET assay of nucleosomal environment could be mostly reporting changes at the level of nucleosome arrays. For example, during early mitotic compaction, the proximity between nucleosomes could increase to form very compact 30 nm fibers (Fig. 26 D). On the other hand, the volumetric assay could be mostly reporting proximity changes between larger chromatin fibers (Fig. 26 E).

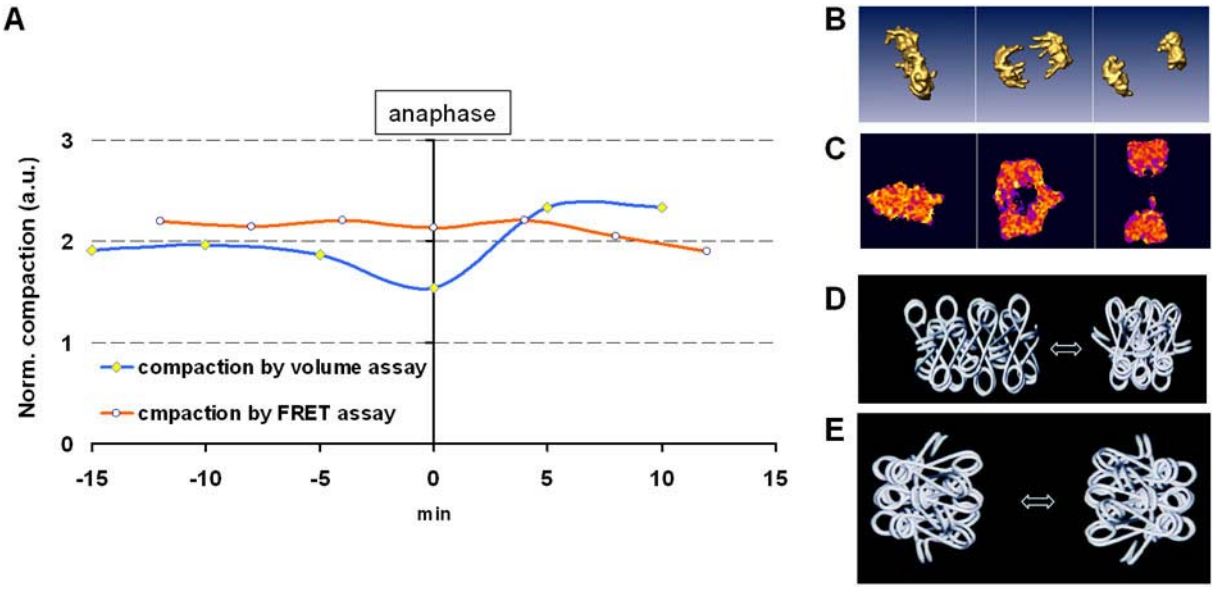

Figure 26. Volumetric vs. FRET assay to measure chromatin compaction at different scales. (A) normalized compaction for both assays in arbitrary units (a.u.). **(B and blue curve in A)** Metaphase-anaphase compaction levels by the volumetric assay (see fig.6). **(C and orange curve in A)** Metaphase-anaphase compaction levels by the FRET assay. Note that the change registered with the volumetric assay is not reported by the FRET assay. **(D)** Model of "30 nm" compaction, which is in the resolution range of the FRET reporter. **(E)** Model of higher-order compaction by increased proximity between larger chromatin fibers, which could result from coiling, folding or compression of large fibers, possibly in the resolution range of the volumetric assay (D & E adapted from Bednar et al., 1998).

It is thus plausible that the anaphase shortening characterized in a previous section may be mostly the result of increased proximity between larger fibers within a chromatid, such as higher folds of the "30 nm fiber", rather than changes at the level of nucleosome array coiling. The further characterization of the structural details of this anaphase compaction will be highly interesting in the future. This process has the potential to be part of an experimental system to investigate different levels of chromosome folding.

VII. 1.5 Limitations and perspectives of the EGFP-ReAsh FRET reporter

The tC-ReAsh FRET reporter system has proven to be very useful for measurements of nucleosome environment that report on condensation levels in fixed cells, in time-lapse imaging of live interphase cells and in live mitotic cells from prometaphase to G1. However, this system has been challenging to apply during entire mitosis starting in late G2 or prophase, because of

increased phototoxicity sensitivity of the observed cells during early mitosis. In this context, new combinations that use the fluorescein bi-arsenide derivative FlAsh may prove to be more suited for complete mitosis measurements. This is because the free-radical production from FlAsh upon illumination may be significantly lower than of ReAsh (C. Schulz, pers. com.).

In the work presented here, the combination of EGFP and ReAsh was preferred because of the very favorable spectral properties of this pair, despite its potential phototoxic effects. If the potentially less phototoxic and green-emitting FlAsh reagent was to be used, a suitable red fluorescent chromophore is needed. Until recently, such a FRET partner for FlAsh was not available. However, the recent development of photostable monomeric RFPs with high quantum yields, for example the promising monomeric red-FP variant mRFP1 and "mCherry" (Shaner et al., 2005), may be a good acceptor partner to establish a FRET system with FlAsh. Nevertheless, fluorescein is also a potent radical producing dye frequently used for chromophore assisted light inactivation and also suffers from relatively rapid photobleaching. Nevertheless even fluorescein is a potent radical producing dye frequently used for chromophore assisted light inactivation and suffers from rapid photobleaching. This FRET assay may thus remain of only limited use for time-lapse observations of mitosis until more stable dyes than arsenide derivatives are available.

VII. 1.6 Comparison of the two assays for the anaphase chromosome lengths

During interphase, the measurement of chromosomal lengths in live cells using light microscopy is challenged by the blurred boundaries between chromosomes, because of the proximity and interdigitation of chromosome territories (see Cremer and Cremer, 2001). During mitosis, this measurement is challenged by the natural dynamics and re-organization of chromosomes that culminate in chromosome segregation. This challenge is transiently eased during late prophase, when chromosomes have fully resolved into distinct rods by intra-chromosomal compaction. However, congression towards the metaphase plane quickly blurs their distinction anew. In addition, it appears unlikely that chromosome dimensions change significantly during the prophase/prometaphase transition (Gerlich et al., 2006).

Individual chromatids may also be transiently distinguished for measurement during early anaphase, when the spindle forces pull sister chromatids from each other (see fig. 7). In mammalian cells with complex karyotypes, distinct long chromatids can be identified and marked in early anaphase. These chromatids then remain traceable during most of the anaphase, because

of their predictable movement toward opposite spindle poles and because their arms protrude as rectilinear elongations out of the rest of the pericentromeric mass of chromatin. By taking advantage of this transient individualization of anaphase chromatids, two assays were developed to measure chromosome lengths in intact mammalian cells undergoing anaphase: **1)** A Photolabeling assay to selectively highlight large chromatid arm segments (Fig. 10 A, B). **2)** a Dual label approach to differentially mark chromatin and centromeres. (Fig. 9 and fig. 10 C, D).
The advantages and disadvantages of each and their complementarity potential are now discussed.

A) Microscope requirements

The PA approach required a microscope with accurate laser control, as it relies heavily on precise photolabeling of a defined sub-region of chromatin, in this case a single chromatid arm. This factor limits the application of this assay to set-ups with such high accuracy. In the experience of our laboratory, the Zeiss LSM 510 systems consistently provide the most accurate pixel by pixel laser-control. By contrast, the second dual-label approach can be performed on all confocal or deconvolution microscopes supporting 4D dual-color imaging.

B) Length information

The dual label provides a full measurement of the axial length of chromatids, from the telomere tip to the centromeres region. By contrast, the PA strategy allows only to safely label an estimated maximum of ~80% of the arm. The plausible assumption that the rest of the arm behaves in similar fashion as the labeled segment is thus needed. This was experimentally confirmed by the combination of the two assays.

C) Chromatid selectivity

Ideally for both assays, only chromatids fully contained in a thin (≤ 1.5 μm) single imaging plane over time should be measured, if assumptions about optical axis resolution are to be minimized (see introduction). The PA strategy has here the advantage of selectivity. Chromatid segments in optimal planes can be selected without relying on the chance of finding entire chromatid arms and their respective centromeric regions in one focal plane, as is the case in the dual-labeling strategy.

D) Chromatid tracking

Dual-labeling measurements become more challenging in late anaphase and telophase, when boundaries between chromosomes blur as a result of focusing towards the spindle pole. In this case, the PA strategy is advantageous, as the discretely labeled regions can be followed even

during the subsequent interphase (Fig 10 A). For this, however, since PAGFP requires 405/413 illumination, it is necessary to limit unspecific photoactivation and phototoxicity by minimizing the imaging laser power, which inevitably lowers the signal-to-noise ratio obtained. In the experience of the group, the switchable FP variant currently providing the best signal-to-noise is PAGFP. Nevertheless, the development of other stable, monomeric photoswitchable FP variants with better spectral properties and higher quantum yields will be beneficial for this approach.

D) Complementarity

Interestingly, the good agreement of the data obtained with both assays allowed to conclude that large chromosome segments are good reporters of the behavior of entire chromosomes. Thus, the unperturbed kinetics of shortening could eventually be obtained by measuring protruding chromatid segments with only a general marker (EGFP-H2b), which minimized phototoxicity (Fig 7 & 12 A, compare with fig.10). This highlights once again the importance of combining diverse approaches to better investigate the structural dynamics of mitotic chromosomes.

VII. 2 Biological Aspects of Anaphase Chromatin Supercompaction

VII. 2.1 Novel anaphase chromosome dynamics

The textbook view of chromosome compaction is that the most compact state of chromosomes is reached in metaphase (p 230Alberts et al., 2002). By measuring the volume that chromatin occupies through mitosis in living cells, it is shown here that the compaction of chromatin during late anaphase is consistently higher than in metaphase. This is suggested already by inspection of single confocal sections in mitotic time-lapse movies, where chromatin in anaphase appears brighter and less expanded than in metaphase (compare Fig. 6 A, +18 and +28 min) and consistent data has been recorded in previous studies, although anaphase was not the focus of those experiments (Swedlow et al., 1993b).

Chromatin volume reduction by microtubule-dependent shortening of chromosomes. Due to the anisotropy of conventional light microscopy an increased brightness in single optical sections can, however, be caused by reorientation of chromosomes along the optical axis, rather

than by true compaction. The quantitative 4D imaging approach showed that there is a true reduction in the three-dimensional space occupied by chromatin in late anaphase. Thus, chromatin reached its maximal compaction 10-14 minutes after all sister chromatids segregated from each other, and just before nuclear assembly and telophase decompaction. This period of mitosis has typically not been in the focus of the plethora of studies on prophase compaction, prometaphase congression, metaphase alignment and anaphase onset (reviewed in Nasmyth, 2002; Swedlow and Hirano, 2003), or - in fewer studies - on the process of decondensation in telophase (Hiraoka et al., 1989; Manders et al., 2003).

A detailed observation of mitotic chromosome dynamics, followed by a quantitative analysis of their lengths during anaphase showed that this maximal compaction is achieved by a lengthwise shortening of chromatid arms. Interestingly, the chromosome arm segments marked and measured with the PA assay kept their relative position and orientation within the mass of anaphase and telophase chromatin throughout their compaction, from a long rod shaped chromatid to a compact spheroid territory and in the subsequent decompaction in telophase. This data is consistent with earlier observations from the group that relative chromosome positions are mostly conserved through mitosis and do not undergo large-scale rearrangements in telophase (Gerlich et al., 2003).

While cytological identification of each measured chromosome was not possible in live anaphase experiments, chromatid arms of different initial lengths (3.5 - 6.5 μm) in rat (Fig. 12 B) and human cells (Fig. 15 B) showed similar shortening kinetics, indicating that this compaction mechanism is independent of chromosome size and is evolutionarily conserved in mammals.

Chromosomes shorten in condensin-depleted cells. Condensins have been shown to participate in the Cdc14-dependent anaphase axial shortening of rDNA loci in the budding yeast (D'Amours et al., 2004; Lavoie et al., 2004; Sullivan et al., 2004) and condensin I is enriched on chromosomes during anaphase in mammalian cells (Gerlich et al., 2006). Therefore, it was interesting to test if condensins would be involved in this mammalian anaphase chromatid compaction by axial shortening. Surprisingly, in condensin-depleted cells that showed the typical phenotype of prometaphase delays and massive segregation problems in early anaphase, normal axial shortening of all non-bridged chromatids was measured. The interesting possibility arises that, analogous to its role in prometaphase (Gerlich et al., 2006), condensin I could help to mechanically stabilize the compacted chromosome arms after axial shortening until nuclear assembly is completed. However, due to the nature of RNA interference depletions, it cannot be formally excluded that residual condensin activity in the RNAi depleted cells contributes to some degree to chromosome arm shortening.

VII. 2.2 Mechanism of microtubule dependence for chromosome compaction

Axial shortening of chromatids was shown to depend on the presence of polymerized and dynamic microtubules. What could be the molecular mechanism underlying this requirement? Based on the results shown here, two non-exclusive possibilities can be proposed.

I) Mechanically-mediated compaction. First, the force generated by microtubule dynamics of the central spindle in late anaphase could mechanically mediate the compaction. Interactions between microtubules and chromosome arms during mitosis have been documented (Rieder et al., 1986) and they may play a crucial role in chromosome alignment and segregation (reviewed in McIntosh et al., 2002)). In principle microtubules could create chromosome compacting forces by processive motor activity of, for instance, chromokinesins (Wang and Adler, 1995), which would use microtubules as tracks. Another possibility is that microtubule dynamics, i.e. flux or growth/shrinkage, could be coupled to chromosome arms via non-motor adaptor proteins such as MAPs (Zhai et al., 1995). Since the precise roles and importance of chromokinesins and tubulin flux are controversial (Ganem et al., 2005; Levesque and Compton, 2001), it will be interesting to probe whether they may be involved in anaphase chromatid shortening.
If processive motor activity along microtubules was responsible for chromatid shortening, this would explain the perturbed shortening observed when microtubules were depolymerized. A prediction of this hypothesis is that microtubule stabilization should in principle preserve the tracks required for motor dynamics. Nevertheless taxol hyperstabilization of microtubules also abolished chromosome shortening, arguing against a simple "motor-on-track" model. Nevertheless, shrinkage of centrosomal microtubules or even growth of pole-pole or central spindle microtubules with opposite polarity, if it were coupled by MAPs to chromosomes, could formally underlie the chromosome compaction we observed as it would be predicted to be sensitive to both depolymerization and stabilization of microtubules.

II) Biochemically-mediated compaction. Second, microtubules could be required for the localization of a biochemical activity that mediates or provides a signal for chromosome shortening. Especially interesting in this context is a recent study in the budding yeast that identified a "NoCut" checkpoint, which delays cytokinesis in anaphase cells with an abnormal

spindle-midzone. If this checkpoint was perturbed, cytokinesis proceeded prematurely, even when late-segregating chromosomes remained in the plane of the cleavage furrow, which led to chromosome damage (Norden et al., 2006). The possibility that mammals have a similar mechanism is supported by the preliminary finding that acute inhibition of Aurora B kinase, a component of the central spindle and necessary for the yeast NoCut checkpoint, impaired axial shortening. Along this line, when arm shortening was perturbed with microtubule poisons, chromatid arms remained as protrusions, but did not stay in the path of the cleavage furrow. Their integrity was thus apparently not directly threatened. By contrast, when the shortening was perturbed with an aurora B inhibitor, several long protruding segments did stay in the path of the cleavage furrow and were prone to damage by cytokinetic closure upon them (Fig. 14). It is thus tempting to speculate that a combined action of microtubule dynamics and aurora B activity could be involved in removing chromosomes from the cytokinetic cut plane by a shortening mechanism. The identification and characterization of the precise molecular mechanisms by which microtubules and Aurora kinase activity are needed to compact chromosomes axially in anaphase will be very interesting to pursue in the future.

Such an investigation, however, faces the special challenge that many, if not all, of the candidate activities may also be required for the preceding mitotic stages, e.g. Aurora B's putative function in histone phosphorylation, which could mask their role during late anaphase. Microinjection of specific antibodies against candidate proteins during the metaphase/anaphase transition is a possible experimental solution. However, this approach is highly challenging, as monolayer mitotic cells are mostly unattached to the substrate (see fig. 4). Thus, the puncturing of the cell for microinjection can easily "shake-it-off" and impede subsequent observations, especially of selected 3D planes. The development of potent, specific and cell-permeable chemical inhibitors is therefore of key importance to achieve acute inhibition of cellular activities at precisely the right moment in a mitotic stage during live imaging experiments, as it has been shown here for the microtubule poisons and Aurora kinase inhibitor.

VII. 2.3 The function(s) of axial shortening of chromosomes

In mammalian and other metazoan cells, chromosome arms frequently protrude several microns from the focused mass of peri/centromeric chromatin after segregation. Why would the cell need to compact chromosomes even further along their axis by lengthwise shortening although

segregation has been achieved? The results presented here suggest two different but non-exclusive functions.

I) Reassembling the correct nuclear architecture. After segregation, chromosomes serve as a template for nuclear envelope (NE) assembly, typically resulting in the formation of a smooth ellipsoid-shaped nucleus. Axial shortening of protruding arms could therefore make sure even late segregating chromosomes with long protruding arms are fully incorporated into a single daughter nucleus with a smooth surface and normal arrangement of chromosome territories. Consistent with this view, chromosomes that could not be fully compacted and tucked into the rest of the chromatin mass when microtubules were perturbed in late anaphase, remained as protrusions, resulting in severely lobulated nuclei (Fig. 16 C). This strongly suggests that the chromatid lengthwise shortening may be important for nuclear architecture in general. In this context, an accumulation of studies has shown that the structure and 3D localization of genes could be crucial for their expression patterns. Not only do gene-rich chromosomes seem to prefer the interior rather than the periphery of the nucleus, but gene-rich regions in more peripheral chromosomes also preferentially face the interior of the nucleus {Osborne, 2004 #76;Cremer, 2001 #20;Spector, 2003 #91; }. Moreover, recent studies have shown that some genes are preferentially associated to heterochromatin near the nuclear periphery when inactive, but may be actively relocated to more central regions upon activation (Dietzel et al., 2004; Kosak et al., 2002; Zink et al., 2004). Furthermore, *in vivo* experiments have shown that some peripheral chromosomal regions near the NE tend to more compact than centrally located regions (Hiraoka et al., 1989; Manders et al., 2003). Thus, if chromatids are not fully compacted and tucked into a single smooth chromatin mass by the time the NE forms, the protruding segments remain semi-isolated right at the time when gene expression processes and patterns are being established in telophase and G1 (Prasanth et al., 2003). This work therefore raises the intriguing possibility that anaphase compaction could be involved in ensuring the start of normal gene expression patterns for all chromosome regions in the next cell generation.

II) Preserving genome integrity. Second, axial chromatid compaction could serve as a failsafe mechanism for chromosome segregation by poleward migration. The measurements of centromere-telomere length clearly showed that shortening occurred independently from the poleward pulling forces exerted on centromeres by kinetochore microtubules. Nevertheless axial shortening may be a complementary segregating force. In naturally or abnormally occurring situations, chromosomes can fail to segregate completely in early anaphase, if the poleward pulling is insufficient, or if it has already stopped, ultimately leading to "cut" phenotypes where

non-segregated chromosomes are unequally split by the cleavage furrow. Axial compaction could provide an additional segregating force to prevent such chromosome cuts. This may normally not be necessary in mammalian cells, but it might be responsible for the rescue of even massive segregation errors, for example those seen in cells where condensin activity has been impaired (fig. 15, see cut chromosome in C, G) (Bhat et al., 1996; Gerlich et al., 2006; Hagstrom et al., 2002). Consistent with this hypothesis, segregation defects in condensin-depleted cells increased markedly if the microtubule-dependent axial shortening of chromosomes was stopped by acute application of microtubule poisons. Also, preliminary experiments of Aurora B kinase activity inhibition resulted in the persistence of several non-shortened chromosomes in the path of ingression of the cleavage furrow, with an increased risk of these chromosomes being damaged or cut by the cytokinetic closure. In yeast, inhibition of a pathway that ensures that chromosomes are not in the way of cytokinesis results in increased chromosome breakage (Norden et al., 2006), but no similar pathway has been identified in metazoans. This work suggests that axial shortening of chromatids may be a force that contributes to safeguard mammalian genome integrity by rescuing segregation defects and by removing chromosomes from the cytokinesis cutting plane.

VIII References

Adams, S.R., R.E. Campbell, L.A. Gross, B.R. Martin, G.K. Walkup, Y. Yao, J. Llopis, and R.Y. Tsien. 2002. New biarsenical ligands and tetracysteine motifs for protein labeling in vitro and in vivo: synthesis and biological applications. *J Am Chem Soc*. 124:6063-76.

Agard, D.A., and J.W. Sedat. 1983. Three-dimensional architecture of a polytene nucleus. *Nature*. 302:676-81.

Alberts, B., A. Johnson, J. Lewis, M. Raff, K. Roberts, and P. Walter. 2002. Molecular Biology of the Cell. Garland New York.

Almagro, S., D. Riveline, T. Hirano, B. Houchmandzadeh, and S. Dimitrov. 2004. The mitotic chromosome is an assembly of rigid elastic axes organized by structural maintenance of chromosomes (SMC) proteins and surrounded by a soft chromatin envelope. *J Biol Chem*. 279:5118-26.

Bannister, A.J., P. Zegerman, J.F. Partridge, E.A. Miska, J.O. Thomas, R.C. Allshire, and T. Kouzarides. 2001. Selective recognition of methylated lysine 9 on histone H3 by the HP1 chromo domain. *Nature*. 410:120-4.

Beaudouin, J., D. Gerlich, N. Daigle, R. Eils, and J. Ellenberg. 2002. Nuclear envelope breakdown proceeds by microtubule-induced tearing of the lamina. *Cell*. 108:83-96.

Beaudouin, J., F. Mora-Bermudez, T. Klee, N. Daigle, and J. Ellenberg. 2006. Dissecting the contribution of diffusion and interactions to the mobility of nuclear proteins. *Biophys J*. 90:1878-94.

Bednar, J., R.A. Horowitz, J. Dubochet, and C.L. Woodcock. 1995. Chromatin conformation and salt-induced compaction: three-dimensional structural information from cryoelectron microscopy. *J Cell Biol*. 131:1365-76.

Bednar, J., R.A. Horowitz, S.A. Grigoryev, L.M. Carruthers, J.C. Hansen, A.J. Koster, and C.L. Woodcock. 1998. Nucleosomes, linker DNA, and linker histone form a unique structural motif that directs the higher-order folding and compaction of chromatin. *Proc Natl Acad Sci U S A*. 95:14173-8.

Belmont, A.S. 2001. Visualizing chromosome dynamics with GFP. *Trends Cell Biol*. 11:250-7.

Belmont, A.S., M.B. Braunfeld, J.W. Sedat, and D.A. Agard. 1989. Large-scale chromatin structural domains within mitotic and interphase chromosomes in vivo and in vitro. *Chromosoma*. 98:129-43.

Belmont, A.S., and K. Bruce. 1994. Visualization of G1 chromosomes: a folded, twisted, supercoiled chromonema model of interphase chromatid structure. *J Cell Biol*. 127:287-302.

Belmont, A.S., S. Dietzel, A.C. Nye, Y.G. Strukov, and T. Tumbar. 1999. Large-scale chromatin structure and function. *Curr Opin Cell Biol*. 11:307-11.

Belmont, A.S., J.W. Sedat, and D.A. Agard. 1987. A three-dimensional approach to mitotic chromosome structure: evidence for a complex hierarchical organization. *J Cell Biol*. 105:77-92.

Bhat, M.A., A.V. Philp, D.M. Glover, and H.J. Bellen. 1996. Chromatid segregation at anaphase requires the barren product, a novel chromosome-associated protein that interacts with Topoisomerase II. *Cell*. 87:1103-14.

Blower, M.D., B.A. Sullivan, and G.H. Karpen. 2002. Conserved organization of centromeric chromatin in flies and humans. *Dev Cell*. 2:319-30.

Brero, A., H.P. Easwaran, D. Nowak, I. Grunewald, T. Cremer, H. Leonhardt, and M.C. Cardoso. 2005. Methyl CpG-binding proteins induce large-scale chromatin reorganization during terminal differentiation. *J Cell Biol*. 169:733-43.

Case, R.B., Y.P. Chang, S.B. Smith, J. Gore, N.R. Cozzarelli, and C. Bustamante. 2004. The bacterial condensin MukBEF compacts DNA into a repetitive, stable structure. *Science*. 305:222-7.

Ceulemans, H., and M. Bollen. 2004. Functional diversity of protein phosphatase-1, a cellular economizer and reset button. *Physiol Rev*. 84:1-39.

Christensen, M.O., M.K. Larsen, H.U. Barthelmes, R. Hock, C.L. Andersen, E. Kjeldsen, B.R. Knudsen, O. Westergaard, F. Boege, and C. Mielke. 2002. Dynamics of human DNA topoisomerases IIalpha and IIbeta in living cells. *J Cell Biol*. 157:31-44.

Clark, D.J., and T. Kimura. 1990. Electrostatic mechanism of chromatin folding. *J Mol Biol*. 211:883-96.

Claussen, U., A. Mazur, and N. Rubtsov. 1994. Chromosomes are highly elastic and can be stretched. *Cytogenet Cell Genet*. 66:120-5.

Cremer, T., and C. Cremer. 2001. Chromosome territories, nuclear architecture and gene regulation in mammalian cells. *Nat Rev Genet*. 2:292-301.

D'Amours, D., F. Stegmeier, and A. Amon. 2004. Cdc14 and condensin control the dissolution of cohesin-independent chromosome linkages at repeated DNA. *Cell*. 117:455-69.

de la Barre, A.E., D. Angelov, A. Molla, and S. Dimitrov. 2001. The N-terminus of histone H2B, but not that of histone H3 or its phosphorylation, is essential for chromosome condensation. *Embo J*. 20:6383-93.

de la Barre, A.E., V. Gerson, S. Gout, M. Creaven, C.D. Allis, and S. Dimitrov. 2000. Core histone N-termini play an essential role in mitotic chromosome condensation. *Embo J*. 19:379-91.

Dietzel, S., and A.S. Belmont. 2001. Reproducible but dynamic positioning of DNA in chromosomes during mitosis. *Nat Cell Biol*. 3:767-70.

Dietzel, S., K. Zolghadr, C. Hepperger, and A.S. Belmont. 2004. Differential large-scale chromatin compaction and intranuclear positioning of transcribed versus non-transcribed transgene arrays containing beta-globin regulatory sequences. *J Cell Sci*. 117:4603-14.

Ducat, D., and Y. Zheng. 2004. Aurora kinases in spindle assembly and chromosome segregation. *Exp Cell Res*. 301:60-7.

Earnshaw, W.C., and M.M. Heck. 1985. Localization of topoisomerase II in mitotic chromosomes. *J Cell Biol*. 100:1716-25.

Eils, R., S. Dietzel, E. Bertin, E. Schrock, M.R. Speicher, T. Ried, M. Robert-Nicoud, C. Cremer, and T. Cremer. 1996. Three-dimensional reconstruction of painted human interphase chromosomes: active and inactive X chromosome territories have similar volumes but differ in shape and surface structure. *J Cell Biol*. 135:1427-40.

Elgin, S.C. 1996. Heterochromatin and gene regulation in Drosophila. *Curr Opin Genet Dev*. 6:193-202.

Fischle, W., B.S. Tseng, H.L. Dormann, B.M. Ueberheide, B.A. Garcia, J. Shabanowitz, D.F. Hunt, H. Funabiki, and C.D. Allis. 2005. Regulation of HP1-chromatin binding by histone H3 methylation and phosphorylation. *Nature*. 438:1116-22.

Förster, T. 1948. Zwischenmolekulare Energiewanderung und Fluoreszenz. *Ann. Phys.*:55-75.

Fukagawa, T. 2004. Assembly of kinetochores in vertebrate cells. *Exp Cell Res*. 296:21-7.

Gaietta, G., T.J. Deerinck, S.R. Adams, J. Bouwer, O. Tour, D.W. Laird, G.E. Sosinsky, R.Y. Tsien, and M.H. Ellisman. 2002. Multicolor and electron microscopic imaging of connexin trafficking. *Science*. 296:503-7.

Galm, O., J.G. Herman, and S.B. Baylin. 2006. The fundamental role of epigenetics in hematopoietic malignancies. *Blood Rev*. 20:1-13.

Ganem, N.J., K. Upton, and D.A. Compton. 2005. Efficient mitosis in human cells lacking poleward microtubule flux. *Curr Biol*. 15:1827-32.

Gasser, S.M., T. Laroche, J. Falquet, E. Boy de la Tour, and U.K. Laemmli. 1986. Metaphase chromosome structure. Involvement of topoisomerase II. *J Mol Biol*. 188:613-29.

Gerlich, D., J. Beaudouin, M. Gebhard, J. Ellenberg, and R. Eils. 2001. Four-dimensional imaging and quantitative reconstruction to analyse complex spatiotemporal processes in live cells. *Nat Cell Biol*. 3:852-5.

Gerlich, D., J. Beaudouin, B. Kalbfuss, N. Daigle, R. Eils, and J. Ellenberg. 2003. Global chromosome positions are transmitted through mitosis in mammalian cells. *Cell*. 112:751-64.

Gerlich, D., and J. Ellenberg. 2003. 4D imaging to assay complex dynamics in live specimens. *Nat Cell Biol*. Suppl:S14-9.

Gerlich, D., T. Hirota, B. Koch, J.M. Peters, and J. Ellenberg. 2006. Condensin I Stabilizes Chromosomes Mechanically through a Dynamic Interaction in Live Cells. *Curr Biol*. 16:333-44.

Giet, R., and D.M. Glover. 2001. Drosophila aurora B kinase is required for histone H3 phosphorylation and condensin recruitment during chromosome condensation and to organize the central spindle during cytokinesis. *J Cell Biol*. 152:669-82.

Gimenez-Abian, J.F., I. Sumara, T. Hirota, S. Hauf, D. Gerlich, C. de la Torre, J. Ellenberg, and J.M. Peters. 2004. Regulation of sister chromatid cohesion between chromosome arms. *Curr Biol*. 14:1187-93.

Grewal, S.I., and S.C. Elgin. 2002. Heterochromatin: new possibilities for the inheritance of structure. *Curr Opin Genet Dev*. 12:178-87.

Grewal, S.I., and J.C. Rice. 2004. Regulation of heterochromatin by histone methylation and small RNAs. *Curr Opin Cell Biol*. 16:230-8.

Gruber, S., C.H. Haering, and K. Nasmyth. 2003. Chromosomal cohesin forms a ring. *Cell*. 112:765-77.

Guacci, V., D. Koshland, and A. Strunnikov. 1997. A direct link between sister chromatid cohesion and chromosome condensation revealed through the analysis of MCD1 in S. cerevisiae. *Cell*. 91:47-57.

Hagstrom, K.A., V.F. Holmes, N.R. Cozzarelli, and B.J. Meyer. 2002. C. elegans condensin promotes mitotic chromosome architecture, centromere organization, and sister chromatid segregation during mitosis and meiosis. *Genes Dev*. 16:729-42.

Hammond, S.M. 2005. Dicing and slicing: the core machinery of the RNA interference pathway. *FEBS Lett*. 579:5822-9.

Hansen, J.C. 2002. Conformational dynamics of the chromatin fiber in solution: determinants, mechanisms, and functions. *Annu Rev Biophys Biomol Struct*. 31:361-92.

Hauf, S., R.W. Cole, S. LaTerra, C. Zimmer, G. Schnapp, R. Walter, A. Heckel, J. van Meel, C.L. Rieder, and J.M. Peters. 2003. The small molecule Hesperadin reveals a role for Aurora B in correcting kinetochore-microtubule attachment and in maintaining the spindle assembly checkpoint. *J Cell Biol*. 161:281-94.

Hauf, S., I.C. Waizenegger, and J.M. Peters. 2001. Cohesin cleavage by separase required for anaphase and cytokinesis in human cells. *Science*. 293:1320-3.

Heitz, E. 1928. Das heterochromatin der moose. *I. Jahrb. Wiss. Botanik*. 69:762-818.

Henikoff, S., T. Furuyama, and K. Ahmad. 2004. Histone variants, nucleosome assembly and epigenetic inheritance. *Trends Genet*. 20:320-6.

Herman, B. 1989. Resonance energy transfer microscopy. *Methods Cell Biol*. 30:219-43.

Herman, B., R.V. Krishnan, and V.E. Centonze. 2004. Microscopic analysis of fluorescence resonance energy transfer (FRET). *Methods Mol Biol*. 261:351-70.

Hirano, T. 2002. The ABCs of SMC proteins: two-armed ATPases for chromosome condensation, cohesion, and repair. *Genes Dev*. 16:399-414.

Hirano, T., and T.J. Mitchison. 1994. A heterodimeric coiled-coil protein required for mitotic chromosome condensation in vitro. *Cell*. 79:449-58.

Hiraoka, Y., J.S. Minden, J.R. Swedlow, J.W. Sedat, and D.A. Agard. 1989. Focal points for chromosome condensation and decondensation revealed by three-dimensional in vivo time-lapse microscopy. *Nature*. 342:293-6.

Hirota, T., D. Gerlich, B. Koch, J. Ellenberg, and J.M. Peters. 2004. Distinct functions of condensin I and II in mitotic chromosome assembly. *J Cell Sci*. 117:6435-45.

Hirota, T., J.J. Lipp, B.H. Toh, and J.M. Peters. 2005. Histone H3 serine 10 phosphorylation by Aurora B causes HP1 dissociation from heterochromatin. *Nature*. 438:1176-80.

Horowitz, R.A., D.A. Agard, J.W. Sedat, and C.L. Woodcock. 1994. The three-dimensional architecture of chromatin in situ: electron tomography reveals fibers composed of a continuously variable zig-zag nucleosomal ribbon. *J Cell Biol*. 125:1-10.

Houchmandzadeh, B., and S. Dimitrov. 1999. Elasticity measurements show the existence of thin rigid cores inside mitotic chromosomes. *J Cell Biol*. 145:215-23.

Houchmandzadeh, B., J.F. Marko, D. Chatenay, and A. Libchaber. 1997. Elasticity and structure of eukaryote chromosomes studied by micromanipulation and micropipette aspiration. *J Cell Biol*. 139:1-12.

Hsu, J.Y., Z.W. Sun, X. Li, M. Reuben, K. Tatchell, D.K. Bishop, J.M. Grushcow, C.J. Brame, J.A. Caldwell, D.F. Hunt, R. Lin, M.M. Smith, and C.D. Allis. 2000. Mitotic phosphorylation of histone H3 is governed by Ipl1/aurora kinase and Glc7/PP1 phosphatase in budding yeast and nematodes. *Cell*. 102:279-91.

Huisinga, K.L., B. Brower-Toland, and S.C. Elgin. 2006. The contradictory definitions of heterochromatin: transcription and silencing. *Chromosoma*. 115:110-22.

Ivanov, D., and K. Nasmyth. 2005. A topological interaction between cohesin rings and a circular minichromosome. *Cell*. 122:849-60.

Janicki, S.M., T. Tsukamoto, S.E. Salghetti, W.P. Tansey, R. Sachidanandam, K.V. Prasanth, T. Ried, Y. Shav-Tal, E. Bertrand, R.H. Singer, and D.L. Spector. 2004. From silencing to gene expression: real-time analysis in single cells. *Cell*. 116:683-98.

Jonkman, J.E., J. Swoger, H. Kress, A. Rohrbach, and E.H. Stelzer. 2003. Resolution in optical microscopy. *Methods Enzymol*. 360:416-46.

Kanda, T., K.F. Sullivan, and G.M. Wahl. 1998. Histone-GFP fusion protein enables sensitive analysis of chromosome dynamics in living mammalian cells. *Curr Biol*. 8:377-85.

Khodjakov, A., I.S. Gabashvili, and C.L. Rieder. 1999. "Dumb" versus "smart" kinetochore models for chromosome congression during mitosis in vertebrate somatic cells. *Cell Motil Cytoskeleton*. 43:179-85.

Khodjakov, A., and C.L. Rieder. 2006. Imaging the division process in living tissue culture cells. *Methods*. 38:2-16.

Kimura, H., and P.R. Cook. 2001. Kinetics of core histones in living human cells: little exchange of H3 and H4 and some rapid exchange of H2B. *J Cell Biol*. 153:1341-53.

Kimura, K., and T. Hirano. 1997. ATP-dependent positive supercoiling of DNA by 13S condensin: a biochemical implication for chromosome condensation. *Cell*. 90:625-34.

Kimura, K., V.V. Rybenkov, N.J. Crisona, T. Hirano, and N.R. Cozzarelli. 1999. 13S condensin actively reconfigures DNA by introducing global positive writhe: implications for chromosome condensation. *Cell*. 98:239-48.

Kireeva, N., M. Lakonishok, I. Kireev, T. Hirano, and A.S. Belmont. 2004. Visualization of early chromosome condensation: a hierarchical folding, axial glue model of chromosome structure. *J Cell Biol*. 166:775-85.

Kornberg, R.D., and Y. Lorch. 1999. Twenty-five years of the nucleosome, fundamental particle of the eukaryote chromosome. *Cell*. 98:285-94.

Kosak, S.T., J.A. Skok, K.L. Medina, R. Riblet, M.M. Le Beau, A.G. Fisher, and H. Singh. 2002. Subnuclear compartmentalization of immunoglobulin loci during lymphocyte development. *Science*. 296:158-62.

Lachner, M., D. O'Carroll, S. Rea, K. Mechtler, and T. Jenuwein. 2001. Methylation of histone H3 lysine 9 creates a binding site for HP1 proteins. *Nature*. 410:116-20.

Lachner, M., R.J. O'Sullivan, and T. Jenuwein. 2003. An epigenetic road map for histone lysine methylation. *J Cell Sci*. 116:2117-24.

Landsverk, H.B., M. Kirkhus, M. Bollen, T. Kuntziger, and P. Collas. 2005. PNUTS enhances in vitro chromosome decondensation in a PP1-dependent manner. *Biochem J*. 390:709-17.

Lavoie, B.D., E. Hogan, and D. Koshland. 2004. In vivo requirements for rDNA chromosome condensation reveal two cell-cycle-regulated pathways for mitotic chromosome folding. *Genes Dev*. 18:76-87.

Levenson, J.M., and J.D. Sweatt. 2005. Epigenetic mechanisms in memory formation. *Nat Rev Neurosci*. 6:108-18.

Levesque, A.A., and D.A. Compton. 2001. The chromokinesin Kid is necessary for chromosome arm orientation and oscillation, but not congression, on mitotic spindles. *J Cell Biol*. 154:1135-46.

Lewis, C.D., and U.K. Laemmli. 1982. Higher order metaphase chromosome structure: evidence for metalloprotein interactions. *Cell*. 29:171-81.

Lippincott-Schwartz, J., and G.H. Patterson. 2003. Development and use of fluorescent protein markers in living cells. *Science*. 300:87-91.

Losada, A., M. Hirano, and T. Hirano. 1998. Identification of Xenopus SMC protein complexes required for sister chromatid cohesion. *Genes Dev*. 12:1986-97.

Losada, A., M. Hirano, and T. Hirano. 2002. Cohesin release is required for sister chromatid resolution, but not for condensin-mediated compaction, at the onset of mitosis. *Genes Dev*. 16:3004-16.

Luger, K. 2002. The tail does not always wag the dog. *Nat Genet*. 32:221-2.

Luger, K., and J.C. Hansen. 2005. Nucleosome and chromatin fiber dynamics. *Curr Opin Struct Biol*. 15:188-96.

Luger, K., A.W. Mader, R.K. Richmond, D.F. Sargent, and T.J. Richmond. 1997. Crystal structure of the nucleosome core particle at 2.8 A resolution. *Nature*. 389:251-60.

Luger, K., and T.J. Richmond. 1998a. DNA binding within the nucleosome core. *Curr Opin Struct Biol*. 8:33-40.

Luger, K., and T.J. Richmond. 1998b. The histone tails of the nucleosome. *Curr Opin Genet Dev*. 8:140-6.

Lund, A.H., and M. van Lohuizen. 2004. Epigenetics and cancer. *Genes Dev*. 18:2315-35.

Machida, Y.J., J.L. Hamlin, and A. Dutta. 2005. Right place, right time, and only once: replication initiation in metazoans. *Cell*. 123:13-24.

Machin, F., J. Torres-Rosell, A. Jarmuz, and L. Aragon. 2005. Spindle-independent condensation-mediated segregation of yeast ribosomal DNA in late anaphase. *J Cell Biol*. 168:209-19.

Maeshima, K., and U.K. Laemmli. 2003. A two-step scaffolding model for mitotic chromosome assembly. *Dev Cell*. 4:467-80.

Manders, E.M., A.E. Visser, A. Koppen, W.C. de Leeuw, R. van Liere, G.J. Brakenhoff, and R. van Driel. 2003. Four-dimensional imaging of chromatin dynamics during the assembly of the interphase nucleus. *Chromosome Res*. 11:537-47.

Marsden, M.P., and U.K. Laemmli. 1979. Metaphase chromosome structure: evidence for a radial loop model. *Cell*. 17:849-58.

Marshall, W.F., J.F. Marko, D.A. Agard, and J.W. Sedat. 2001. Chromosome elasticity and mitotic polar ejection force measured in living Drosophila embryos by four-dimensional microscopy-based motion analysis. *Curr Biol*. 11:569-78.

McGuinness, B.E., T. Hirota, N.R. Kudo, J.M. Peters, and K. Nasmyth. 2005. Shugoshin prevents dissociation of cohesin from centromeres during mitosis in vertebrate cells. *PLoS Biol*. 3:e86.

McIntosh, J.R., E.L. Grishchuk, and R.R. West. 2002. Chromosome-microtubule interactions during mitosis. *Annu Rev Cell Dev Biol*. 18:193-219.

Mellone, B.G., L. Ball, N. Suka, M.R. Grunstein, J.F. Partridge, and R.C. Allshire. 2003. Centromere silencing and function in fission yeast is governed by the amino terminus of histone H3. *Curr Biol*. 13:1748-57.

Michaelis, C., R. Ciosk, and K. Nasmyth. 1997. Cohesins: chromosomal proteins that prevent premature separation of sister chromatids. *Cell*. 91:35-45.

Mikhailov, A., R.W. Cole, and C.L. Rieder. 2002. DNA damage during mitosis in human cells delays the metaphase/anaphase transition via the spindle-assembly checkpoint. *Curr Biol*. 12:1797-806.

Murnion, M.E., R.R. Adams, D.M. Callister, C.D. Allis, W.C. Earnshaw, and J.R. Swedlow. 2001. Chromatin-associated protein phosphatase 1 regulates aurora-B and histone H3 phosphorylation. *J Biol Chem*. 276:26656-65.

Nasmyth, K. 2002. Segregating sister genomes: the molecular biology of chromosome separation. *Science*. 297:559-65.

Nasmyth, K. 2005. How do so few control so many? *Cell*. 120:739-46.

Nasmyth, K., and C.H. Haering. 2005. The structure and function of SMC and kleisin complexes. *Annu Rev Biochem*. 74:595-648.

Norden, C., M. Mendoza, J. Dobbelaere, C. Kotwaliwale, S. Biggins, and Y. Barral. 2006. The NoCut pathway links completion of cytokinesis to spindle midzone function to prevent chromosome breakage. *Cell*. 125:85-98.

Paulson, J.R., and U.K. Laemmli. 1977. The structure of histone-depleted metaphase chromosomes. *Cell*. 12:817-28.

Phair, R.D., S.A. Gorski, and T. Misteli. 2004. Measurement of dynamic protein binding to chromatin in vivo, using photobleaching microscopy. *Methods Enzymol*. 375:393-414.

Prasanth, K.V., P.A. Sacco-Bubulya, S.G. Prasanth, and D.L. Spector. 2003. Sequential entry of components of the gene expression machinery into daughter nuclei. *Mol Biol Cell*. 14:1043-57.

Prigent, C., and S. Dimitrov. 2003. Phosphorylation of serine 10 in histone H3, what for? *J Cell Sci*. 116:3677-85.

Rabut, G., and J. Ellenberg. 2004. Automatic real-time three-dimensional cell tracking by fluorescence microscopy. *J Microsc*. 216:131-7.

Redon, C., D. Pilch, E. Rogakou, O. Sedelnikova, K. Newrock, and W. Bonner. 2002. Histone H2A variants H2AX and H2AZ. *Curr Opin Genet Dev*. 12:162-9.

Richards, E.J. 2006. Inherited epigenetic variation - revisiting soft inheritance. *Nat Rev Genet*.

Richards, E.J., and S.C. Elgin. 2002. Epigenetic codes for heterochromatin formation and silencing: rounding up the usual suspects. *Cell*. 108:489-500.

Rieder, C.L., E.A. Davison, L.C. Jensen, L. Cassimeris, and E.D. Salmon. 1986. Oscillatory movements of monooriented chromosomes and their position relative to the spindle pole result from the ejection properties of the aster and half-spindle. *J Cell Biol*. 103:581-91.

Rieder, C.L., and E.D. Salmon. 1994. Motile kinetochores and polar ejection forces dictate chromosome position on the vertebrate mitotic spindle. *J Cell Biol*. 124:223-33.

Rieder, C.L., A. Schultz, R. Cole, and G. Sluder. 1994. Anaphase onset in vertebrate somatic cells is controlled by a checkpoint that monitors sister kinetochore attachment to the spindle. *J Cell Biol*. 127:1301-10.

Rogakou, E.P., D.R. Pilch, A.H. Orr, V.S. Ivanova, and W.M. Bonner. 1998. DNA double-stranded breaks induce histone H2AX phosphorylation on serine 139. *J Biol Chem*. 273:5858-68.

Rydberg, B., W.R. Holley, I.S. Mian, and A. Chatterjee. 1998. Chromatin conformation in living cells: support for a zig-zag model of the 30 nm chromatin fiber. *J Mol Biol*. 284:71-84.

Saitoh, N., I.G. Goldberg, E.R. Wood, and W.C. Earnshaw. 1994. ScII: an abundant chromosome scaffold protein is a member of a family of putative ATPases with an unusual predicted tertiary structure. *J Cell Biol*. 127:303-18.

Salic, A., J.C. Waters, and T.J. Mitchison. 2004. Vertebrate shugoshin links sister centromere cohesion and kinetochore microtubule stability in mitosis. *Cell*. 118:567-78.

Sambrook, J., and D. Russel. 2001. Molecular clonning: a laboratory manual. Cold Spring Harbour Laboratory Press, New York.

Schalch, T., S. Duda, D.F. Sargent, and T.J. Richmond. 2005. X-ray structure of a tetranucleosome and its implications for the chromatin fibre. *Nature*. 436:138-41.

Sedat, J., and L. Manuelidis. 1978. A direct approach to the structure of eukaryotic chromosomes. *Cold Spring Harb Symp Quant Biol*. 42 Pt 1:331-50.

Shaner, N.C., P.A. Steinbach, and R.Y. Tsien. 2005. A guide to choosing fluorescent proteins. *Nat Methods*. 2:905-9.

Shilatifard, A. 2006. Chromatin Modifications by Methylation and Ubiquitination: Implications in the Regulation of Gene Expression. *Annu Rev Biochem*.

Stray, J.E., and J.E. Lindsley. 2003. Biochemical analysis of the yeast condensin Smc2/4 complex: an ATPase that promotes knotting of circular DNA. *J Biol Chem*. 278:26238-48.

Strick, T.R., T. Kawaguchi, and T. Hirano. 2004. Real-time detection of single-molecule DNA compaction by condensin I. *Curr Biol*. 14:874-80.

Strukov, Y.G., Y. Wang, and A.S. Belmont. 2003. Engineered chromosome regions with altered sequence composition demonstrate hierarchical large-scale folding within metaphase chromosomes. *J Cell Biol*. 162:23-35.

Sullivan, M., T. Higuchi, V.L. Katis, and F. Uhlmann. 2004. Cdc14 phosphatase induces rDNA condensation and resolves cohesin-independent cohesion during budding yeast anaphase. *Cell*. 117:471-82.

Sumara, I., E. Vorlaufer, P.T. Stukenberg, O. Kelm, N. Redemann, E.A. Nigg, and J.M. Peters. 2002. The dissociation of cohesin from chromosomes in prophase is regulated by Polo-like kinase. *Mol Cell*. 9:515-25.

Swedlow, J.R., D.A. Agard, and J.W. Sedat. 1993a. Chromosome structure inside the nucleus. *Curr Opin Cell Biol*. 5:412-6.

Swedlow, J.R., and T. Hirano. 2003. The making of the mitotic chromosome: modern insights into classical questions. *Mol Cell*. 11:557-69.

Swedlow, J.R., K. Hu, P.D. Andrews, D.S. Roos, and J.M. Murray. 2002. Measuring tubulin content in Toxoplasma gondii: a comparison of laser-scanning confocal and wide-field fluorescence microscopy. *Proc Natl Acad Sci U S A*. 99:2014-9.

Swedlow, J.R., J.W. Sedat, and D.A. Agard. 1993b. Multiple chromosomal populations of topoisomerase II detected in vivo by time-lapse, three-dimensional wide-field microscopy. *Cell*. 73:97-108.

Tachibana, M., K. Sugimoto, M. Nozaki, J. Ueda, T. Ohta, M. Ohki, M. Fukuda, N. Takeda, H. Niida, H. Kato, and Y. Shinkai. 2002. G9a histone methyltransferase plays a dominant role in euchromatic histone H3 lysine 9 methylation and is essential for early embryogenesis. *Genes Dev*. 16:1779-91.

Tanaka, T., J. Fuchs, J. Loidl, and K. Nasmyth. 2000. Cohesin ensures bipolar attachment of microtubules to sister centromeres and resists their precocious separation. *Nat Cell Biol*. 2:492-9.

Uhlmann, F., D. Wernic, M.A. Poupart, E.V. Koonin, and K. Nasmyth. 2000. Cleavage of cohesin by the CD clan protease separin triggers anaphase in yeast. *Cell*. 103:375-86.

van Holde, K.E. 1988. Chromatin. Springer Berlin.

Waizenegger, I.C., S. Hauf, A. Meinke, and J.M. Peters. 2000. Two distinct pathways remove mammalian cohesin from chromosome arms in prophase and from centromeres in anaphase. *Cell*. 103:399-410.

Wang, S.Z., and R. Adler. 1995. Chromokinesin: a DNA-binding, kinesin-like nuclear protein. *J Cell Biol*. 128:761-8.

Warren, W.D., S. Steffensen, E. Lin, P. Coelho, M. Loupart, N. Cobbe, J.Y. Lee, M.J. McKay, T. Orr-Weaver, M.M. Heck, and C.E. Sunkel. 2000. The Drosophila RAD21 cohesin persists at the centromere region in mitosis. *Curr Biol*. 10:1463-6.

Wassenegger, M. 2005. The role of the RNAi machinery in heterochromatin formation. *Cell*. 122:13-6.

Wei, Y., L. Yu, J. Bowen, M.A. Gorovsky, and C.D. Allis. 1999. Phosphorylation of histone H3 is required for proper chromosome condensation and segregation. *Cell*. 97:99-109.

White, C.L., R.K. Suto, and K. Luger. 2001. Structure of the yeast nucleosome core particle reveals fundamental changes in internucleosome interactions. *Embo J*. 20:5207-18.

Wirth, K.G., G. Wutz, N.R. Kudo, C. Desdouets, A. Zetterberg, S. Taghybeeglu, J. Seznec, G.M. Ducos, R. Ricci, N. Firnberg, J.M. Peters, and K. Nasmyth. 2006. Separase: a universal trigger for sister chromatid disjunction but not chromosome cycle progression. *J Cell Biol*. 172:847-60.

Wolffe, A. 1998. Chromatin: Structure and Function. Academic Press.

Woodcock, C.L., S.A. Grigoryev, R.A. Horowitz, and N. Whitaker. 1993. A chromatin folding model that incorporates linker variability generates fibers resembling the native structures. *Proc Natl Acad Sci U S A*. 90:9021-5.

Wouters, F.S., P.J. Verveer, and P.I. Bastiaens. 2001. Imaging biochemistry inside cells. *Trends Cell Biol*. 11:203-11.

Zachariae, W., and K. Nasmyth. 1999. Whose end is destruction: cell division and the anaphase-promoting complex. *Genes Dev*. 13:2039-58.

Zhai, Y., P.J. Kronebusch, and G.G. Borisy. 1995. Kinetochore microtubule dynamics and the metaphase-anaphase transition. *J Cell Biol*. 131:721-34.

Zink, D., M.D. Amaral, A. Englmann, S. Lang, L.A. Clarke, C. Rudolph, F. Alt, K. Luther, C. Braz, N. Sadoni, J. Rosenecker, and D. Schindelhauer. 2004. Transcription-dependent spatial arrangements of CFTR and adjacent genes in human cell nuclei. *J Cell Biol*. 166:815-25.

Zink, D., N. Sadoni, and E. Stelzer. 2003. Visualizing chromatin and chromosomes in living cells. *Methods*. 29:42-50.

IX Appendix

IX. 1 Macro Codes for the Intensity Distribution Assay

IX. 1.1 Masker-Quantifier

// This imageJ tool combines masking and quantitation. It selects a region within an image or //stack by first masking the same target region by Gaussian //diffusion, thresholding and //binarization; then it extracts the pixel count, intensity integral, mean //intensity and mean //standard deviation of pixels with intensity values above a given threshold, within //an image //or images in a stack.

```
macro "Masker_Quantifier 1.0"

	{
	requires("1.34h");

//	Input
	threshold=getNumber("Masking Threshold",15);
	stack1 = getImageID;
	p=nSlices;
	rename("Raw");
	run("Duplicate...", "title=Masker duplicate");
	lx=getWidth-1;
	ly=getHeight-1;
	p=nSlices;
//
		selectWindow("Masker");
		run("Gaussian Blur...", "radius=4 stack");
		for (k=1; k<=p; k++) {
		w=k-1;
		setSlice(k);
		for (i=0; i<=lx; i++) {
		for (j=0; j<=ly; j++) {

			value=getPixel(i,j);
			if (value>threshold) setPixel(i,j,1);
			else setPixel(i,j,0);   }
								}
							}
	run("Image Calculator...", "image1=Raw operation=Multiply image2=Masker
	create stack");
	rename("Masked");

//	input 2
	selectWindow("Masked");
	Qt=getNumber("Quantitation threshold",10);
	lx=getWidth-1;
```

```
        ly=getHeight-1;
        stack1 = getImageID;
        p=nSlices;

//      Output
        integ=newArray(p);
        mean=newArray(p);
        number=newArray(p);
        Stdev=newArray(p);

//      (k=1; k<=p; k++) {

                w=k-1;
                setSlice(k);
                sum1=0;
                Numpixels=0;
                for (i=0; i<=lx; i++) {
                for (j=0; j<=ly; j++) {

                        value=getPixel(i,j);
          if (value>Qt) { sum1=sum1+value; Numpixels=Numpixels+1; }
                                        }
                                }
                integ[w]=sum1;
                mean[w]=sum1/Numpixels;
                number[w]=Numpixels;

                sum2=0;
                for (i=0; i<=lx; i++) {
                  for (j=0; j<=ly; j++) {

                        value=getPixel(i,j);
                if (value>Qt)
                        sum2=sum2+(value-sum1/Numpixels)*(value-sum1/Numpixels);
                                        }
                                }
                Stdev[w]=sqrt(sum2/(Numpixels-1));
                                        }

                run("Clear Results");
                row=0;
                for (k=0; k<p; k++) {
                setResult("Pixels", row, number[k]);
                setResult("Integral", row, integ[k]);
                setResult("Mean Intensity", row, mean[k]);
                setResult("St. deviation", row, Stdev[k]);
                row++;
                                        }
                updateResults();
        }
        }
```

IX. 1.2 Focalizer

// This imageJ tool selects each most-in-focus slice per stack of fluorescent images, within a time //series, based on the intensity integral of pixels above a given threshold. Best performance is //achieved on images with one or few fluorescent structures, such as chromatin, or the mitotic //spindle.

```
macro "4D Focalizer 1.0"

	{
	requires("1.34h");

//	Input
	if (nSlices==1)
	exit("This tool requires a time-lapse with 3D stacks");

	SliN=getNumber("Slices per Stack",18);
	t=nSlices/SliN;
	value=t-floor(t);
	if (value!=0)
	exit("This tool requires a constant number of slices per stack");

	threshold=getNumber("Threshold",10);
	lx=getWidth-1;
	ly=getHeight-1;
//
	stack1 = getImageID;
	rename("Original");
	run("New...", "name=inFocus type=8-bit fill=White width="+getWidth()+"
	height="+getHeight()+" slices="+t);

	for (k=1; k<=t; k++)  {
		selectWindow("Original");
			sum2=0;
			v=0;
			for (l=1; l<=SliN; l++){
			sum1=0;

		selectWindow("Original");
			setSlice(l+(k-1)*SliN);
			for (i=0; i<=lx; i++)   {
			for (j=0; j<=ly; j++)   {
			value=getPixel(i,j);

			if (value>threshold) { sum1=sum1+value;}
                                                }
                                                }

			if (sum1>sum2) {sum2=sum1; v=l;}
                                                }
```

```
                    setSlice(v+(k-1)*SliN); run("Copy");

 selectWindow("inFocus");
 setSlice(k);
 run("Paste");
         setResult("column #", k-1, v);
                                              }
updateResults();
}
```

IX. 2 Publications

Automated analysis of the mitotic phases of human cells in 3D fluorescence microscopy image sequences

Nathalie Harder[1], Felipe Mora-Bermúdez[2], William Godinez Navarro[1], Jan Ellenberg[2], Roland Eils[1], and Karl Rohr[1]

[1]German Cancer Research Centre (DKFZ), Dept. Theoretical Bioinformatics, and University of Heidelberg, IPMB, Dept. Bioinformatics and Functional Genomics, Im Neuenheimer Feld 580, D-69120 Heidelberg, Germany
[2]European Molecular Biology Laboratory (EMBL), Gene Expression and Cell Biology/Biophysics Programmes, Meyerhofstrasse 1, D-69117 Heidelberg, Germany
Email: n.harder@dkfz-heidelberg.de

Abstract. The amount of data produced by high-throughput screens of the gene function raises the demand for automated analysis. In particular, the evaluation of images acquired in genome-wide cell phenotype screens constitutes a substantial bottleneck and motivates the development of automated image analysis methods. Here we introduce a computational scheme to process 3D multi-cell time-lapse images as they are produced in high-throughput RNAi experiments. We describe an approach to automatically segment, track, and classify cell nuclei into different mitotic phases. This enables automated analysis of the duration of single phases of the cell live cycle and thus the identification of cell cultures that show an abnormal mitotic behaviour. Our scheme proves a high average accuracy of around 89%, suggesting a promising future for automating the evaluation of high-throughput experiments.

1 Introduction

In recent years the technology of *RNA interference* (RNAi) has become the method of choice for identifying the biological function of genes in the field of functional genomics. With this screening method all known genes of a considered organism are systematically silenced one after the other, and then the resulting morphological changes are analyzed. However, such large-scale knockdown screens provide enormous amounts of data which require tools for automated image analysis.

Our work is carried out within the EU project *MitoCheck*, which aims to explore the coordination of mitotic processes in human cells at a molecular level and to contribute to revealing the mechanisms of cancer development. To identify the genes that are involved in cell division (mitosis), genome-wide high-throughput RNAi screens are performed. Fluorescence microscopy time-lapse images of the treated cell culture are acquired to study the effect of a silenced gene on mitosis.

This contribution is concerned with the automated evaluation of an assay to analyze the duration of the different phases in mitotic progression. In *normal* cells of one type the duration of the mitotic phases is similar. To study the duration of mitotic phases of *treated* cells a specific assay has been developed which is characterized by significant elongations of mitotic phases compared to control experiments. To automatically determine whether mitotic phases of treated cells are longer compared to normal cells, cells have to be observed throughout their live cycle and for each time point the respective phase has to be determined.

Previous work on automated analysis of cell images has been done in different application fields. Based on fluorescence microscopy imaging complete cells as well as single subcellular structures have been studied. The automated recognition of subcellular structures is a major task in location proteomics and work has been done in this field given 2D (e.g., [1–3]) and 3D (e.g., [4]) single cell images. Classification of complete cells has been performed, for example, to investigate the influence of drugs on cellular proteins [5]. In [6] tracking of cells in 2D microscopy images has been used to improve segmentation and cell quantification. Automated analysis of cell images plays an increasing role particularly for the evaluation of high-throughput cell phenotype screens. Approaches for *single-frame* multi-cell *2D* images have been described in [7–9].

We have developed an approach to analyse multi-cell *image sequences* from large-scale RNAi screens. In comparison to previous work, we analyse *3D* cell array time-lapse images that include multiple cell nuclei in *different mitotic phases*. Each image of an image sequence contains three slices that have been acquired with a confocal fluorescence microscope. Our computational scheme for analyzing the duration of mitotic phases consists of four main steps: Segmentation of multi-cell images, tracking of cells, image feature extraction, and classification into the mitotic phases. For fast and accurate segmentation we use a region adaptive thresholding technique. Our tracking scheme is able to cope with the splitting of cells during mitosis which is important in our application. With this scheme tree-structured tracks are computed which represent cell pedigrees. Based on the tracking result we automatically select the most informative slice out of the 3D image, which is then used for feature extraction. Compared to previous work, we incorporate temporal changes of the cell morphology between ancestrally related cells by directly including dynamic image features. A Support Vector Machine classifier is used to classify the cells into the following seven mitotic phases: *interphase, prophase, prometaphase, metaphase, anaphase1, anaphase2*, and *telophase*. Based on the classification result in subsequent images the duration of the different phases can be determined. It is the first time that an automated scheme is presented which yields a detailed classification into the above mentioned phases of dividing cells. Our approach has been successfully applied to four image sequences from genome-wide high-throughput RNAi screens. We have compared the performance with ground truth provided by manual evaluation and it turned out that we obtain an average accuracy of around 89%.

2 Methods

2.1 Image Analysis Workflow

For a detailed analysis of the different phases of dividing cells high-resolution confocal fluorescence microscopy images of the DNA have been acquired. Compared to previous work we here use 3D images consisting of three confocal planes (slices). The reason is that cells change their morphology during mitosis, i.e. in the interphase they are flat, but with the beginning of cell division they arch upward and take the shape of a hemisphere. Therefore, if we would use the same focal plane throughout the cell cycle the cell structure (DNA) could not well be observed. Since we are using multi-cell images that contain cells in different mitotic phases, it is impossible to define one focal plane per time step that well represents all cells. Therefore, three slices from three different focal planes are aquired that cover the range of possible cell shape changes. Because of technical reasons in the image acquisition process the number of slices is restricted to three. This relatively small number of slices does not allow a complete 3D analysis. Thus, we apply the workflow shown in Fig. 1 for automated analysis. In the first step, we apply a maximum intensity projection (MIP) for each time step, resulting in 2D images. In the second step, we perform segmentation and tracking based on these MIP images to determine the correspondences of cell nuclei in subsequent frames. Based on the segmentation and tracking result we now go back to the original 3D images and define 3D ROIs for each cell. For each 3D ROI we choose the slice containing the most information for feature selection. The reason of using the original images lies in the fact that these images contain much more detailed information about the inner intensity structure of a cell. Finally, static and dynamic features are extracted and classification is performed resulting in a sequence of mitotic phases for each cell trajectory.

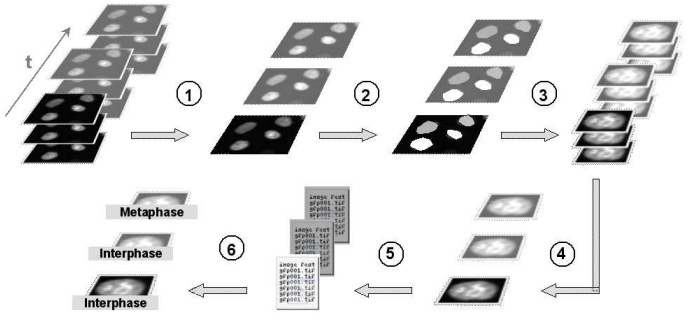

Fig. 1. Image analysis workflow: (1) Maximum intensity projection of multi-cell 3D images; (2) Segmentation and tracking in 2D; (3) Extraction of 3D ROIs including single cells based on the segmentation and tracking results; (4) Selection of the most informative slice; (5) Feature extraction; (6) Classification

2.2 Segmentation of Multi-Cell Images

Since we have to cope with a huge number of multi-cell images, fast and reliable segmentation and labeling of single objects is crucial. Various advanced segmentation algorithms have been described in the literature, but as computation time plays an important role here, the speed of the algorithm is a decisive criterion. We have investigated three different thresholding techniques which we previously used for static 2D multi-cell images. It turned out that global threshold segmentation does not produce satisfying results especially for low-contrast cells. Instead, local adaptive thresholding can segment the cell nuclei with high accuracy (see Fig. 2). Consequently we apply the latter technique which incorporates several improvements compared to [9]. The algorithm uses a quadratic sliding window to calculate local thresholds for different regions of an image. A local threshold is only calculated if the variance within the window reaches a user-defined threshold, else a global threshold is used [10]. This ensures that only for regions that contain a certain amount of information the local threshold is calculated, which significantly reduces the computation time. The threshold is applied to a quadratic region at the center of the sliding window and the window is shifted by the length of this inner region. Compared to [9] this modification reduces segmentation errors at the region borders. To calculate the global and the local intensity thresholds we applied two histogram-based threshold selection schemes: The *Otsu* method [11] and the *Kittler&Illingworth* method [12]. We found that the combination of [11] to determine the global threshold and [12] to determine the local thresholds yielded the best results (see Fig. 2c).

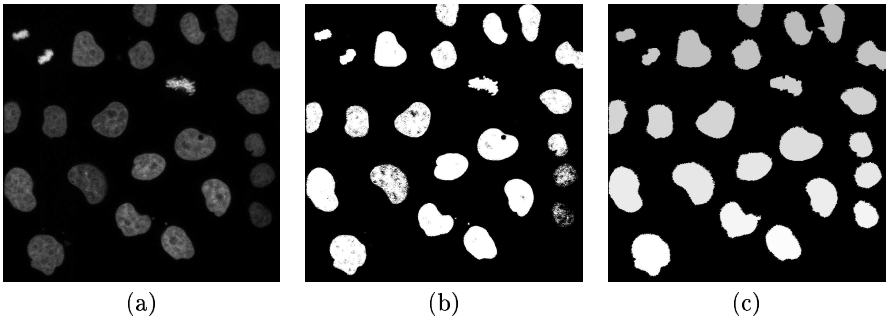

(a) (b) (c)

Fig. 2. (a) Original image, (b) Global threshold (Otsu), (c) Local adaptive threshold

2.3 Tracking of Mitotic Cell Nuclei

To analyze the mitotic behavior of single cells in multi-cell images, a tracking scheme is required which determines the temporal connections and can handle splitting objects. We have developed the following two-step tracking scheme: First, initial, non-splitting trajectories are established, and second, mitotic events are detected and the related trajectories are merged. In the first step the initial trajectories are determined using a feature point tracking algorithm based on

[13]. As feature points we use the centers of gravity of segmented cell nuclei. For each frame of an image sequence the algorithm considers the predecessor and successor frame. In these frames, object correspondences are determined by searching for trajectories with maximum smoothness. In the second step, all trajectories that do not start in the first frame are taken into account as possible mitotic events. The decision whether a trajectory should be treated as mitosis event is made depending on the distance-overlap-ratio of potential parent and child objects [14]. In addition, the smoothness of the potential compound trajectory is taken into account. For the identified splitting events the corresponding tracks are finally merged.

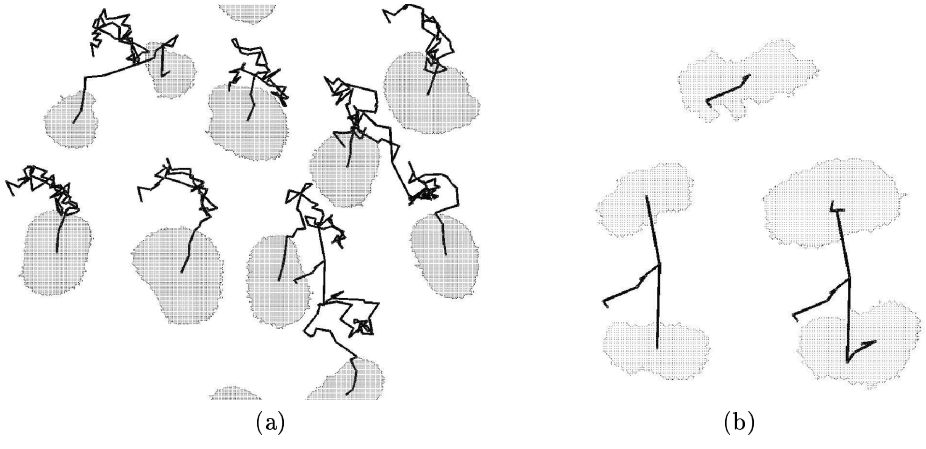

(a) (b)

Fig. 3. (a) Tracking result including three mitotic cells, (b) Example of the splitting of one cell in three consecutive images

2.4 Extraction of Static and Dynamic Features from Most Informative Slices

As described in section 2.1, we compute for each cell nucleus 3D ROIs in the original 3D images. Within these ROIs we select the cell's individual *most informative slice* in order to extract image features. Two selection criteria for determining the slice that contains the most information have been tested: the maximum total intensity and the maximum entropy. We found that the *maximum-intensity* criterion performs very well compared to manual selection, whereas the *maximum-entropy* criterion often failed and showed a high sensivity to noise. Consequently, here we apply the maximum-intensity criterion. Within the most informative slice we compute a set of static and dynamic image features. The static features comprise granularity features, object- and edge-related features, tree-structured wavelet features, Haralick texture features, grey scale invariants, and Zernike moments. The dynamic features represent the morphological changes of cells in adjacent frames. To this end, we compute the difference of three basic image features (*object size, mean intensity,* and *standard deviation*) for each cell to its pre-

decessor and to its successor. We chose these three features because they exhibit characteristic changes during mitosis as the example plot of the mean intensity in Fig. 4 demonstrates. For example, between *Prophase* and *Prometaphase* we can observe a steep rise of the mean intensity and for *Anaphase1* a chracteristic spike. In total we compute 332 features for each cell nucleus. For the training set, we standardize each feature w.r.t. a mean value of zero and a standard deviation of one. In the test set, the feature values are linearly transformed based on the transformation parameters from the training set.

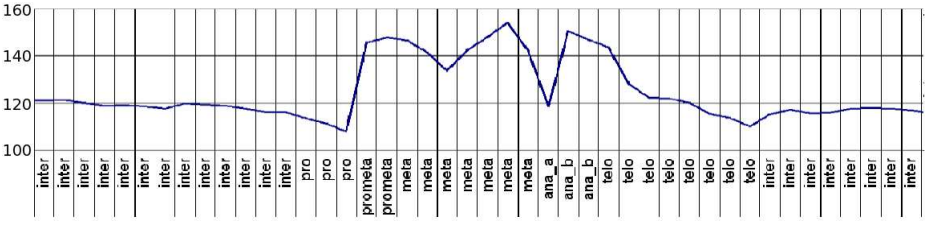

Fig. 4. Plot of the mean intensity and the manually assigned phases throughout mitosis for one cell

2.5 Classification

We apply a Support Vector Machine (SVM) classifier with a Radial Basis Function (RBF) as kernel function to classify the nuclei into the seven classes *Interphase, Prophase, Prometaphase, Metaphase, Anaphase1, Anaphase2,* and *Telophase* (see Fig. 5). SVMs are mathematically well-founded and they have the advantage that their complexity is independent of the dimension in feature space compared to other classification methods. This property allows us to work with a high number of features and we can skip the feature selection step as it is not crucial. We solve the multi-class classification problem with a "one-against-one" approach. For k classes this method constructs $k(k-1)/2$ binary classifiers and trains each classifier for two classes. To optimize the penalty parameter C and the kernel parameter γ for the Radial Basis Function, we perform a three-fold cross-validation with varying values of C and γ on the training set (model selection) prior to the actual training of the classifier.

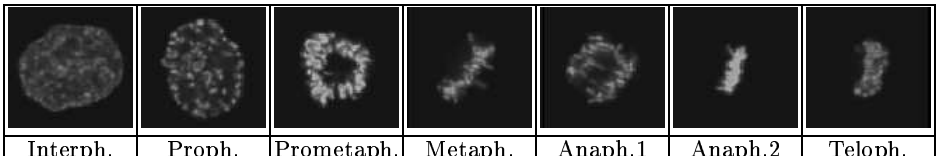

Interph.	Proph.	Prometaph.	Metaph.	Anaph.1	Anaph.2	Teloph.
1143	*79*	*56*	*120*	*17*	*89*	*263*

Fig. 5. Example images of the different mitotic phases and number of available samples

3 Experimental Results

3.1 Image Data

In our study we use 3D image sequences that have been aquired with a confocal fluorescence microscope in the framework of the EU project MitoCheck at the European Molecular Biology Laboratory (EMBL) Heidelberg. Chromosome morphology is visualized using a HeLa (Kyoto) cell line stably expressing the chromosomal marker histone 2B-EGFP. One image contains about 20 nuclei with an average diameter of approximatly 100-150 pixels (in the *Interphase*). All images have a gray value depth of 8 bit and a spatial resolution of 1024×1024 pixels. Each image sequence comprises 124 to 128 time steps with a temporal resolution of 10 min and three image slices per time step.

3.2 Classification Results

We have applied our approach given four sequences of 3D multi-cell images. Using Maximum Intensity Projection on all stacks of all sequences resulted in 500 projected multi-cell images. These images have been segmented and tracked. The tracking scheme was able to detect ..% of the mitosis events. Since the subsequent processing steps rely on correctly detected mitosis events we corrected the few remaining ones manually. Static and dynamic features have been extracted based on the most informative slice for all segmented and tracked nuclei. To provide ground truth for the classification, all nuclei have been classified manually into one of the seven phases of the cell life cycle: (1)*Interphase*, (2)*Prophase*, (3)*Prometaphase*, (4)*Metaphase*, (5)*Anaphase1* (chromosome segregation in progress), (6)*Anaphase2* (chromosome segregation finished), and (7)*Telophase*. We split the available samples for each class randomly into training data and test data at a ratio of 2:1. The numbers of samples and example images for each class are given in Fig. 5. The feature values were standardized and a Support Vector Machine classifier was trained as described in section 2.5. An evaluation of the experimental results yielded accuracies for the different phases (classes) between 80% and 98% and an average accuracy of 90.1%. In order to check the reliability of the result we repeated the classification step, applying a five-fold outer cross-validation on the whole data set. This classification yielded an average accuracy of 88.5% (see confusion matrix Tab. 2). Thus, both classification results correspond well and we can draw the conclusion that we can rely on an average classification accuracy of around 89%.

To examine the effect of including dynamic features, we removed all dynamic features and repeated both classification experiments. In this case we obtained an average accuracy of 80.5% for the experiment without cross validation, and 79.1% for the experiment with five-fold cross validation (see confusion matrix Tab. 1). Again, both results correspond well.

It also turns out that by *including* dynamic features we can achive much higher accuracies . The improvement becomes even more obvious when we compare the accuracies for the single phases of both experiments as listed in Tabs. 2

and 1: If dynamic features are included the accuracies are significantly higher for all phases, except for the *Telophase*. The largest improvement can be observed for *Anaphase1* with an increase from 29.4% to 64.7% and for *Prometaphase* with an increase from 78.6% to 91.1%. Since the three phases *Prometa-*, *Meta-*, and *Anaphase1* are characterized by movements of the chromosomal strctures, they have high within-class variabilities and also high between-class similarities. This is the reason for misclassifications that can be observed between these classes in the confusion matrices. Especially for these three classes the incorporation of dynamic features results in a major improvement.

True Class	**Classifier Output**							**Accur.**
	Inter	Pro	Prometa	Meta	Ana1	Ana2	Telo	[%]
Inter	**1109**	8	0	1	0	0	26	97.0
Pro	11	**66**	1	0	1	0	0	83.5
Prometa	0	0	**44**	6	6	0	0	78.6
Meta	1	0	5	**110**	0	0	4	91.7
Ana1	1	0	5	3	**5**	2	1	29.4
Ana2	0	0	0	0	1	**76**	12	85.4
Telo	21	0	0	1	2	8	**231**	87.8

Table 1. Confusion matrix and accuracies for the experiment with five-fold cross validation; dynamic features have *not* been included; overall accuracy: 79.1%.

True Class	**Classifier Output**							**Accur.**
	Inter	Pro	Prometa	Meta	Ana1	Ana2	Telo	[%]
Inter	**1114**	6	0	1	0	0	22	97.5
Pro	5	**72**	2	0	0	0	0	91.1
Prometa	0	0	**51**	5	0	0	0	91.1
Meta	0	0	2	**114**	1	1	2	95.0
Ana1	1	0	2	2	**11**	1	0	64.7
Ana2	0	0	0	0	1	**84**	4	94.4
Telo	33	0	0	1	1	3	**225**	85.6

Table 2. Confusion matrix and accuracies for the experiment with five-fold cross validation; dynamic features have been *included*; average accuracy: 90.1%.

4 Discussion and Conlusion

We have presented an approach for automated analysis of the duration of mitotic phases in 3D confocal microscopy image sequences. Our approch segments and tracks splitting cells throughout the sequences and thus determines cell pedigrees. By using static and dynamic features our scheme classifies the cells with a high accuracy into seven mitotic phases. Based on the sequence of phases that have been computed in subsequent frames, the duration of each phase can be

determined. The determined phase durations can be compared to control experiments to automatically identify experiments that show delays in mitotic phases.

Acknowledgement

This work has been supported by the EU project MitoCheck.

References

1. Danckaert, A., Gonzalez-Couto, E., Bollondi, L., Thompson, N., Hayes, B.: Automated recognition of intracellular organelles in confocal microscope images. Traffic **3** (2002) 66–73
2. Huang, K., Murphy, R.: Boosting accuracy of automated classification of fluorescence microscope images for location proteomics. BMC Bioinformatics **5** (2004) 78
3. Conrad, C., Erfle, H., Warnat, P., Daigle, N., Löch, T., Ellenberg, J., Pepperkok, R., Eils, R.: Automatic identification of subcellular phenotypes on human cell arrays. Genome Research **14** (2004) 1130–1136
4. Chen, X., Murphy, R.: Robust classification of subcellular location patterns in high resolution 3d fluorescence microscope images. In: Proc. 26th Annu. Int. Conf. IEEE Engineering in Medicine and Biology Society, San Francisco, CA (2004) 1632–1635
5. Lindblad, J., Wählby, C., Bengtsson, E., Zaltsman, A.: Image analysis for automatic segmentation of cytoplasms and classification of rac1 activation. Cytometry Part A **57A** (2003) 22–33
6. Yang, F., Mackey, M., Ianzini, F., Gallardo, G., Sonka, M.: Cell segmentation, tracking, and mitosis detection using temporal context. In Duncan, J., Gerig, G., eds.: Proc. MICCAI'2005. Volume 3749., Palm Springs, CA, USA, Springer-Verlag (2005) 302–309
7. Perlman, Z., Slack, M., Feng, Y., Mitchison, T., Wu, L., Altschuler, S.: Multidimensional drug profiling by automated microscopy. Science **306** (2004) 1194–1198
8. Zhou, X., Liu, K.Y., Bradley, P., Perrimon, N., Wong, S.T.: Towards automated cellular image segmentation for RNAi genome-wide screening. In Duncan, J., Gerig, G., eds.: Proc. MICCAI'2005. Volume 3749., Palm Springs, CA, USA, Springer-Verlag (2005) 302–309
9. Harder, N., Neumann, B., Held, M., Liebel, U., Erfle, H., Ellenberg, J., Eils, R., Rohr, K.: Automated recognition of mitotic patterns in fluorescence microscopy images of human cells. In: Proc. IEEE Int. Symp. Biomedical Imaging (ISBI'2006), Arlington, USA (2006)
10. Gonzalez, R., Woods, R.: Digital Image Processing. 2nd edn. Prentice Hall (2002)
11. Otsu, N.: A threshold selection method from grey level histograms. IEEE Transactions on Systems, Man and Cybernetics **9** (1979) 62–66
12. Kittler, J., Illingworth, J.: Minimum error thresholding. Pattern Recognition **19**(1) (1986) 41–47
13. Chetverikov, D., Verestoy, J.: Tracking feature points: a new algorithm. In: Proc. 14th Int. Conf. Pattern Recognition, Brisbane, Australia (1998) 1436–1438
14. Withers, J.: Tracking cell splits and merges. In: Southwest Symp. Image Analysis and Interpretation. (1996) 117–122

Dissecting the Contribution of Diffusion and Interactions to the Mobility of Nuclear Proteins

Joël Beaudouin, Felipe Mora-Bermúdez, Thorsten Klee, Nathalie Daigle, and Jan Ellenberg
Gene Expression and Cell Biology/Biophysics Programs, European Molecular Biology Laboratory, Heidelberg, Germany

ABSTRACT Quantitative characterization of protein interactions under physiological conditions is vital for systems biology. Fluorescence photobleaching/activation experiments of GFP-tagged proteins are frequently used for this purpose, but robust analysis methods to extract physicochemical parameters from such data are lacking. Here, we implemented a reaction-diffusion model to determine the contributions of protein interaction and diffusion on fluorescence redistribution. The model was validated and applied to five chromatin-interacting proteins probed by photoactivation in living cells. We found that very transient interactions are common for chromatin proteins. Their observed mobility was limited by the amount of free protein available for diffusion but not by the short residence time of the bound proteins. Individual proteins thus locally scan chromatin for binding sites, rather than diffusing globally before rebinding at random nuclear positions. By taking the real cellular geometry and the inhomogeneous distribution of binding sites into account, our model provides a general framework to analyze the mobility of fluorescently tagged factors. Furthermore, it defines the experimental limitations of fluorescence perturbation experiments and highlights the need for complementary methods to measure transient biochemical interactions in living cells.

INTRODUCTION

Since the first studies on nuclear protein dynamics (1–4), a large number of studies have shown that the majority of nuclear proteins examined so far are highly dynamic: they diffuse rapidly in the nucleoplasm and typically show a fast exchange with their binding sites (e.g., (5–8)). This dynamic behavior is thought to have a major role in chromatin organization and plasticity, and in regulation of gene expression. Conceptually high dynamics have been interpreted as evidence that nuclear proteins find their specific binding sites by random three-dimensional diffusion and collision in the entire nuclear space. To model the interaction of nuclear proteins quantitatively for systems biology, methods to accurately determine their binding times under physiological conditions are needed.

Fluorescence recovery after photobleaching (FRAP), and more recently, photoactivation (PA) as well, have become methods of choice to visualize the dynamics of fluorescently tagged proteins in cells (9–11). These fluorescence perturbation methods offer the possibility to quantitatively characterize diffusive processes and kinetics of interactions with binding sites in a physiological context and can be readily performed on most commercial confocal laser scanning microscopes. By contrast, analyzing such experiments to extract physicochemical parameters of molecular mobility is nontrivial. Several analysis models have been developed, some to characterize diffusion alone (12–15), but most models were designed to characterize chemical interactions. However, fluorescence redistributions can be limited by interactions and diffusion, which, in principle, requires us to solve the complex problem of reaction-diffusion systems. Although this was done in some mostly theoretical studies (14,16–19) almost all biological studies have assumed that diffusion was not limiting the fluorescence recovery (6,20–22) and therefore neglected it to simplify the analysis. Many studies (for example, of nuclear proteins) assumed that if fluorescence redistribution was long compared to the case of freely diffusing molecules, diffusion could be neglected in the analysis (e.g., (23)). Unfortunately, this assumption is incorrect, because very transient interactions where diffusion is clearly limiting, can also lead to slow fluorescence redistributions—as was also noticed recently by others during the preparation of this article (18). In addition, all analysis methods we are aware of have ignored or largely simplified the cellular geometry, within which protein mobility occurs, and assumed a homogeneous distribution of binding sites. Although neglecting diffusion and ignoring cellular geometry and the distribution of binding sites can lead to wrong interpretations of fluorescence perturbation experiments, these assumptions that underlie widely used analysis methods are typically not validated in the biological literature.

The goal of this study was therefore to analyze the contribution of both diffusion and chemical interactions to the kinetics of fluorescence redistribution. To compare our data to previous studies, we used the well-studied case of chromatin interacting proteins. We used photoactivation of proteins tagged with photoactivatable GFP (PAGFP, (11)) to perturb steady-state distribution of fluorescence and followed its redistribution by standard fluorescence confocal microscopy. Analysis was performed by simulating the

Submitted July 22, 2005, and accepted for publication November 28, 2005.

Address reprint requests to J. Ellenberg, E-mail: jan.ellenberg@embl.de.

J. Beaudouin's present address is German Cancer Research center (DKFZ), Div. Theoretical Bioinformatics (B080), Im Neuenheimer Feld 580 (TP3), D-69120 Heidelberg, Germany.

0006-3495/06/03/1878/17 $2.00

doi: 10.1529/biophys.105.071241

relaxation after perturbation with a reaction-diffusion model and fitting to the experimental data. Importantly, the model used the real geometry of the nucleus and took the inhomogeneous distribution of binding sites (in this case, chromatin) into account. We applied our method to the chromatin proteins guanine nucleotide exchange factor RCC1 (24), the histone methyltransferase SUV39H1, and its hyperactive mutant (25), and five isoforms of the linker histone H1 (26). All three types of proteins bind either to nucleosomes or DNA in general, without known sequence specificity. In contrast to previous studies, we found that diffusion limits the fluorescence redistribution for all of these proteins, and that with the exception of the hyperactive mutant of SUV39H1, the interaction was so transient that only the upper limit of its residence time and the fraction of unbound protein could be measured with standard fluorescence perturbation methods. Our method provides a new general framework to analyze the contribution of diffusion and interaction to fluorescence redistributions in the nucleus, and can be extended to other cellular compartments.

MATERIALS AND METHODS

DNA constructs, protein purification, cell lines, and cell culture

H2B-diHcRed was described in Gerlich et al. (27). β-galactosidase-diHcRed was made by fusing the entire coding sequence of β-galactosidase (28) 5′ to diHcRed (27), generating a LPDPPVAT linker between the two proteins. pEGFP-RCC1 was made by fusing the entire coding sequence of RCC1 (a generous gift from Iain Mattaj) 3′ to EGFP (Clontech Laboratories, Palo Alto, CA) generating a SGLRS linker between the two proteins. PAGFP-RCC1 was made by replacing the coding sequence of EGFP by PAGFP (11). H2B-PAGFP was made by fusing the entire coding sequence of H2B 5′ to PAGFP generating a DPP linker between the two proteins. PAGFP-hERα was made using EGFP-hERα (29) and replacing EGFP by PAGFP. H1.1, H1.2, H1.3, H1.4, and H1.5-PAGFP were made by fusing the entire coding sequence of the different H1 5′ to PAGFP generating the linker PGIHRPVAT between the proteins. PAGFP-SUV39H1 and PAGFP-SUV39H1-H320R were made by fusing the entire coding sequence of SUV39H1 and the mutant H320R (25) 3′ to PAGFP generating a YSD-LEGGRDYKDDDDKGGR linker between the two proteins. EGFP-HP1β was made by fusing the entire coding sequence of HP1β (a generous gift from Howard Worman) 3′ to EGFP, generating a SGLRSLE linker between the two proteins.

Normal rat kidney (NRK) cells stably expressing H1.1-PAGFP, H1.2-PAGFP, H1.3-PAGFP, H1.4-PAGFP, H1.5-PAGFP, PAGFP-SUV39H1, H2B-PAGFP, and H2B-diHcRed were selected according to standard protocols and maintained in DMEM/10% FCS/0.5 mg/ml G418. Transfections were done using FuGene 6 (Roche, Mannheim, Germany). PAGFP-RCC1, PAGFP-hERα, and PAGFP-SUV39H1-H320R were transiently transfected and experiments were performed 24 h or 48 h after transfection for PAGFP-RCC1and PAGFP-hERα, and one week after transfection in the case of PAGFP-SUV39H1-H320R. PAGFP-hERα photoactivation was performed in the presence of 10 nM of β-estradiol (Sigma, Taufkirchen, Germany).

For microscopy, cells were cultured in No. 1 LabTekII chambered cover glasses (Nalge Nunc International, Naperville, IL) and maintained at 37°C on the microscope as described (30). In all experiments either H2B-DiHcRed or β-galactosidase-diHcRed were used as nuclear reference for image alignment.

PAGFP-RCC1 was histidine-tagged and purified on a nickel-agarose column (Qiagen, Valencia, CA). It was immobilized in a 30% acrylamide gel cast between a coverslip and a microscope slide to test photoactivation settings.

Photoactivation and three-dimensional imaging

Photoactivation experiments were performed on a Zeiss LSM 510 or a LSM 510 Meta (Carl Zeiss, Jena, Germany). PAGFP was photoactivated using a 80-mW Kr, 413-nm laser (Coherent, Dieburg, Germany) on the LSM 510 or a 20-mW, 405-nm laser diode (Point Source, Hamble, UK) on the LSM 510 Meta and observed at 488 nm. The 488-nm laser line was used at low power to prevent any residual photobleaching or photoactivation. A 40× PlanApochromat IRIS NA 1.0 oil objective (Zeiss) was used and the pinhole was wide-open to ensure imaging the entire nucleus. All images were 128 × 128 pixels to allow short frame acquisition times (100 ms). For all experiments, half of the nucleus was photoactivated and the whole nucleus was imaged. In the case of PAGFP alone, the cytoplasmic pool of protein was photoactivated and subsequently photobleached to prevent any contribution from the cytoplasm to the measurements. The experiment was then performed within the next 30 s on the nucleus to minimize the equilibration between nucleus and cytoplasm. H2B-PAGFP was imaged using an autofocus and tracking macro as described (31).

Simulations in three dimensions were performed starting from stacks of confocal sections of real nuclei with 0.3*0.3*0.35 μm^3 (xyz) voxel sizes.

Image segmentation, alignment, and quantitation

Segmentation of three-dimensional stacks and quantitation of fluorescence intensities for the simulation were performed using in-house developed plugins for ImageJ (http://rsb.info.nih.gov/ij/). Photoactivation sequences were aligned as follows: first, each sequence was aligned using the nuclear diHcRed signal using a registration plug-in on ImageJ (http://bigwww.epfl.ch/thevenaz/turboreg/); then the same transformation was applied on the PAGFP signal using a in-house modified version of the plugin.

Quantitation for data fitting was performed with the LSM 2.8 software using an in-house developed macro to measure and format the fluorescence intensities for simulation and parameter optimization. Background was subtracted and intensities were normalized to the total intensity. Typically, nuclei were divided in six regions distributed along the main fluorescence redistribution direction, covering the whole nucleus.

Quantitation of fluorescence recovery was performed with ImageJ. Fluorescence of a bleached or a nonphotoactivated region was background-subtracted and normalized to the total intensity, also background-subtracted. This measurement was then normalized to 0 for the image taken right after photobleaching or photoactivation and to 100 for the steady-state distribution of fluorescence, yielding a direct readout of the percentage of recovery.

Computer simulation and curve fitting

Partial differential equations were simulated numerically using a finite difference approach. The following equation,

$$\frac{\partial[\text{free}(\vec{r},t)]}{\partial t} = D\Delta([\text{free}(\vec{r},t)]) - k_{on}[C(\vec{r})][\text{free}(\vec{r},t)] + k_{off}[\text{bound}(\vec{r},t)],$$

$$\frac{\partial[\text{bound}(\vec{r},t)]}{\partial t} = k_{on}[C(\vec{r})][\text{free}(\vec{r},t)] - k_{off}[\text{bound}(\vec{r},t)],$$

becomes, in finite differences in three dimensions,

$$\frac{\partial[\text{free}(i,j,k,t)]}{\partial t} = \frac{D}{p_i^2}([\text{free}(i-1,j,k,t)] + [\text{free}(i+1,j,k,t)] - 2[\text{free}(i,j,k,t)]) + \frac{D}{p_j^2}([\text{free}(i,j-1,k,t)] + [\text{free}(i,j+1,k,t)] - 2[\text{free}(i,j,k,t)]) + \frac{D}{p_k^2}([\text{free}(i,j,k-1,t)] + [\text{free}(i,j,k+1,t)] - 2[\text{free}(i,j,k,t)]) - k_1(i,j,k)[\text{free}(i,j,k,t)] + k_{off}[\text{bound}(i,j,k,t)],$$

$$\frac{\partial[\text{bound}(i,j,k,t)]}{\partial t} = k_1(i,j,k)[\text{free}(i,j,k,t)] - k_{off}[\text{bound}(i,j,k,t)],$$

with p_i, p_j, and p_k the spatial steps in the three dimensions and $[\text{free}(i,j,k,t)]$ and $[\text{bound}(i,j,k,t)]$ the local concentration of free and bound fluorescent proteins at the position (i,j,k) in the grid.

$k_1(i,j,k)\text{is}(k_{off}/Free)(i^{st}(i,j,k)/i^{st}_{average} - Free)$, with i^{st} (i,j,k) the steady-state intensity at the position (i,j,k) in the grid and $i^{st}_{average}$ the sum of all the i^{st} (i,j,k) dividing by the number of grid elements that are inside the nucleus.In two dimensions, the equation becomes

$$\frac{\partial[\text{free}(i,j,t)]}{\partial t} = \frac{D}{p_i^2}([\text{free}(i-1,j,t)] + [\text{free}(i+1,j,t)] - 2[\text{free}(i,j,t)]) + \frac{D}{p_j^2}([\text{free}(i,j-1,t)] + [\text{free}(i,j+1,t)] - 2[\text{free}(i,j,t)]) - k_1(i,j)[\text{free}(i,j,t)] + k_{off}[\text{bound}(i,j,t)],$$

$$\frac{\partial[\text{bound}(i,j,t)]}{\partial t} = k_1(i,j)[\text{free}(i,j,t)] - k_{off}[\text{bound}(i,j,t)],$$

with p_i and p_j the spatial steps in the two dimensions. For our simulations, we chose $p_i = p_j$.

In three dimensions, the nucleus was subdivided in cuboids (Fig. 2 *A*), all of identical size with a typical side length of 0.3 μm (doubling the size did not significantly change the simulation result). As proteins were assumed not to cross the nuclear envelope, fluxes were fixed to zero across nuclear boundaries. The system of ordinary differential equations derived from the discretization was simulated and fitted to data using the solver Berkeley Madonna (www.berkeleymadonna.com). Initial conditions were measured from images taken right after photoactivation. Steady-state distributions of fluorescence were measured from images either before photoactivation at 413 or 405 nm or when the redistribution was complete at 488 nm. Integration was performed using a Runge-Kutta fourth-order algorithm with an adaptive step-size. The curve fit used the downhill simplex method. The six measured regions were fitted to the simulation except in the case of SUV39H1-H320R, where only two measured regions were fitted (see Results). Residuals were calculated by subtracting the fit from the data and normalizing it to the values of the fit at the end of the simulation.

The simplified two-dimensional model, and potentially other unidentified systematic experimental errors, induced small but systematic deviation of the residuals from zero (see Supplementary Material, Fig. S3A), which makes the statistical analysis of the fit and of the confidence interval by classical methods not conclusive (data not shown). We therefore broadened this confidence interval by using an empirical cutoff at two times the square of the residuals obtained by the best fit (see one example in Supplementary Material, Fig. S3B).

RESULTS

A general reaction-diffusion model in the geometry of the nucleus

A simple experimental test for diffusion limited mobility: gradient smoothing

To characterize the interaction kinetics of proteins with chromatin by photoactivation and kinetic modeling, we first tested experimentally whether diffusion could be neglected by analyzing gradient shapes after photoactivation. If the intensity profile of the gradient changes during fluorescence redistribution, diffusion has to be modeled, otherwise it can be neglected (32). As expected, the highly mobile PAGFP alone expressed in normal rat kidney (NRK) cells, which should only diffuse, showed a smoothing gradient over time (Fig. 1 *A*). By contrast, the slowly exchanging core histone H2B (33) exhibited a completely constant intensity profile after normalization (Fig. 1 *B*). We then tested five dynamic chromatin interacting proteins tagged with (PA)GFP and expressed in NRK cells: RCC1, SUV39H1, and its hyperactive mutant, H1.1, estrogen receptor hERα, and heterochromatin protein 1 HP1β. For all five proteins, fluorescence gradients smoothed over time and diffusion therefore had to be taken into account to model the mobility of these proteins (see Fig. 1 *C* for RCC1, and Supplementary Material, Fig. S1, for the other proteins). Importantly, the timescale of fluorescence redistribution did not correlate with gradient smoothing. Chromatin interacting proteins that showed a change of gradient shape required between 2.8 s (SUV39H1) and 24.5 min (H1.1) for 80% fluorescence redistribution (Fig. 1 and Supplementary Material, Fig. S1, *last image of each row*). This clearly shows that the length of fluorescence redistribution cannot be used to determine if it is limited by diffusion or not.

A general three-dimensional reaction-diffusion model for chromatin interacting proteins

We therefore developed a model that included both diffusion and chemical interactions to simulate the fluorescence redistribution after photoactivation and fit the simulation to the experiments to determine the amount of bound protein, its residence time and, where possible, the diffusion coefficient of the unbound protein. The model was initially

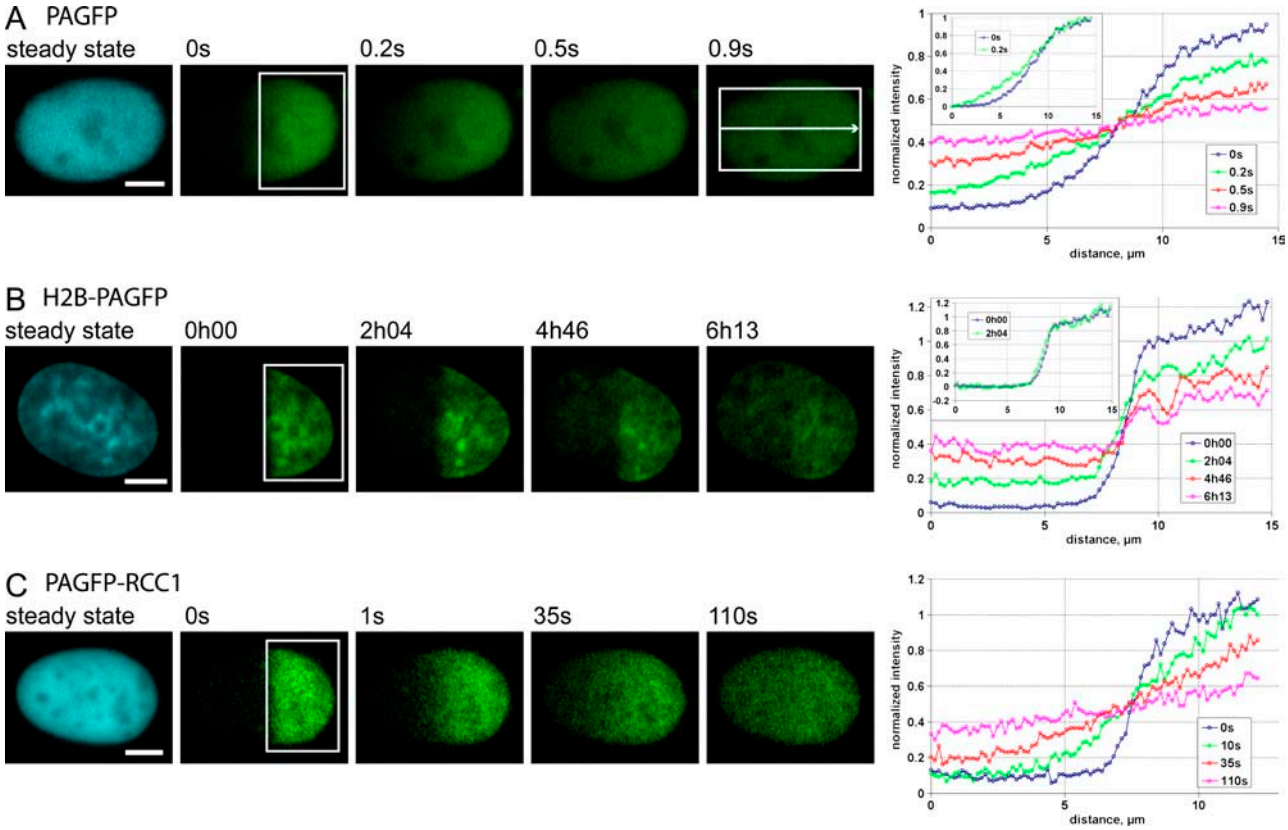

FIGURE 1 Test for diffusion-limited mobility NRK cells expressing PAGFP transiently (*A*), H2B-PAGFP stably (*B*), and PAGFP-RCC1 transiently (*C*). The first image of each dataset shows protein steady-state distribution in the nucleus imaged at 413 or 405 nm at low laser power before photoactivation. In all cases, half of the nucleus was photoactivated (*open rectangle* on *second frame* of each dataset). The last image represent 80% of fluorescence redistribution compared to steady state. To measure intensity profiles, each dataset was cropped using cropping regions like the one represented on the last frame of PAGFP. For each protein intensity, profiles were measured along the long axis of the nucleus, averaged along the short axis and normalized with the profile in steady state to generate fluorescence profiles for each time point. Plots display fluorescence intensity versus distance along the nucleus. The insets for PAGFP and H2B-PAGFP show the same profiles normalized between 0 and 1: note that whereas normalized profiles do not change for H2B-PAGFP, they become smoother for PAGFP and for PAGFP-RCC1. Scale bars: 5 μm.

built in three dimensions based on the real geometry of the nucleus and distribution of chromatin of each observed cell.

We assumed that proteins are immobile when bound to chromatin, because chromatin does not show large-scale movements over 1 h in mammalian cells (34–36) and that free molecules can normally diffuse within the whole nucleus with a single diffusion coefficient D following Fick's second law,

$$\frac{\partial[\text{free}(\vec{r},t)]}{\partial t} = D\Delta([\text{free}(\vec{r},t)]), \quad (1)$$

where $[\text{free}(\vec{r},t)]$ is the local concentration of unbound fluorescent molecules. We also assumed that chromatin occupies a negligible volume and that all binding sites are equally accessible. The interaction between proteins and chromatin was modeled as a simple first-order chemical reaction,

$$free + C \underset{k_{off}}{\overset{k_{on}}{\rightleftharpoons}} bound, \quad (2)$$

where *free* is the free protein, C is the free binding site on chromatin, *bound* is the bound protein, and k_{on} and k_{off} are the on- and off-rates of the interaction. Combining diffusion and interaction kinetics, changes in the local concentrations of fluorescent proteins during fluorescence redistribution can then be described by the partial differential equations of

$$\frac{\partial[\text{free}(\vec{r},t)]}{\partial t} = D\Delta([\text{free}(\vec{r},t)]) - k_{on}[C(\vec{r})][\text{free}(\vec{r},t)] + k_{off}[\text{bound}(\vec{r},t)]$$
$$\frac{\partial[\text{bound}(\vec{r},t)]}{\partial t} = k_{on}[C(\vec{r})][\text{free}(\vec{r},t)] - k_{off}[\text{bound}(\vec{r},t)]. \quad (3)$$

It is important to note that photobleaching/activation perturbs the fluorescence only and is assumed not to modify the chemical interaction of fluorescent molecules. Therefore, the fluorescence perturbation does not affect the distribution of chemical species, seen independently of their fluorescent state. Therefore, as in our case chemical interactions can be considered to be in steady state over the whole experiment,

the distribution of free binding sites $[C(\vec{r})]$ does not depend on time. Their spatial distribution is nevertheless not known, leading to an unknown parameter $k_{on}[C(\vec{r})]$ that depends on space. Nevertheless, we could show that this spatial dependency can be fully determined from the fluorescence distribution in steady state (see Appendix A), and that Eq. 3 can be rewritten by replacing $k_{on}[C(\vec{r})]$ by a parameter $k_1(\vec{r}) = (k_{off}/\text{Free})[i^{st}(\vec{r})/i^{st}_{average} - \text{Free}]$ where $i^{st}(\vec{r})$ is the steady-state intensity distribution in space, proportional to the concentration of fluorescent protein (37), $i^{st}_{average}$is the average steady-state intensity over the whole nucleus and *Free* is the global fraction of unbound proteins in steady state:

$$\frac{\partial[\text{free}(\vec{r},t)]}{\partial t} = D\Delta([\text{free}(\vec{r},t)]) - k_1(\vec{r})[\text{free}(\vec{r},t)] + k_{off}[\text{bound}(\vec{r},t)]$$

$$\frac{\partial[\text{bound}(\vec{r},t)]}{\partial t} = k_1(\vec{r})[\text{free}(\vec{r},t)] - k_{off}[\text{bound}(\vec{r},t)]. \quad (4)$$

Although Eq. 3 contains two parameters, D and k_{off}, that are constant and one parameter, $k_{on}[C(\vec{r})]$, that depends on space, Eq. 4 has the major advantage of containing three parameters, D, k_{off}, and *Free* that do not depend on space, and only requires the intensity distribution in steady state, which can easily be measured experimentally.

The reaction-diffusion Eq. 4 was simulated in silico using the real geometry of a nucleus and a typical distribution of chromatin interacting proteins (Fig. 2). As it cannot be solved analytically in such a complex geometry, it was solved numerically using a finite difference approach (Fig. 2 *A*; see also Materials and Methods, above). Initial conditions are needed for the free and bound fluorescent protein concentrations, but for chromatin proteins the resolution of light microscopy does not allow the discrimination between these two populations, and images just after photoactivation only provide their local sum $i(\vec{r},t)$. We thus further assumed that the ratio between free and bound fluorescent proteins after activation is the same as in steady state, which is correct either when the fluorescence perturbation (photoactivation/bleaching) is so fast that no significant free protein movement occurs during the perturbation, or when the interaction is so fast that local free and bound pools immediately equilibrate.

Two-dimensional simplification of the reaction-diffusion model

Most molecular kinetics are too fast to be imaged in three dimensions by acquiring *z*-stacks of images over time. We therefore performed all image acquisitions in two dimensions on a confocal laser scanning microscope with a wide-open pinhole and a low numerical aperture objective focused in the middle of the nucleus, such that the entire nuclear depth could be illuminated and detected (Fig. 3 *A*). To directly use this two-dimensional information, and to reduce the computing time, we then tested the validity of a two-dimensional model. In this simplified model we assumed that the steady-state concentration of free proteins was homogeneous and that the distribution of bound and free fluorescent proteins could be considered as two-dimensional (see Materials and Methods, above, for the finite difference equations), whereas, in fact, our two-dimensional observations correspond to the convolution of the reaction-diffusion process in three dimensions with the point-spread function (PSF) axially centered in the middle of the nucleus. To test the simplification we simulated a photoactivation experiment in three dimensions (Fig. 3 *B*, *first row*; see Supplementary Material 1 for the details of the procedure and (38) for the assumptions used), that we convolved radially, using the axial profile of Fig. 3 *A* to project in two dimensions and mimic our observation (Fig. 3 *B*, *second row*). We then tested the simplified model with these two-dimensional convolved images by fitting the six regions depicted on the figure (Fig. 3 *B*, *second row*, *last frame*) equally distributed in the direction of the fluorescence gradient. As can be seen on the plots, it can be fitted to the convolved images, and the fitted parameters are similar to the one used for the three-dimensional simulation. This shows that deconvolution of

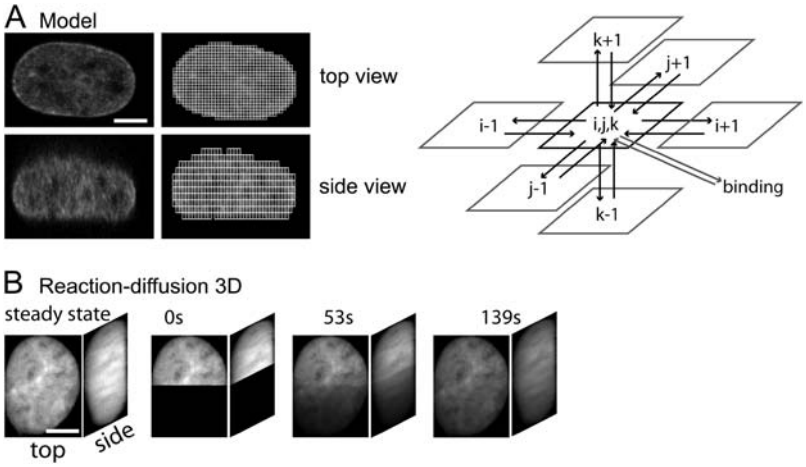

FIGURE 2 Modeling. (*A*) Finite difference approach of reaction-diffusion model. The nucleus, in this case an NRK cell expressing transiently PAGFP-SUV39H1, is discretized in cuboids (*images*). The reaction occurs in each cuboid (*arrows* ''binding'') and exchange of free proteins occurs between the nearest-neighbors by diffusion (*solid arrows*). (*B*) Simulation of a photoactivation experiment in three dimensions starting from a cell transiently expressing PAGFP-SUV39H1. The three-dimensional sequence shows the simulated nucleus before perturbation (*first image*) and during fluorescence redistribution, from the top and the side (*total intensity projection*).

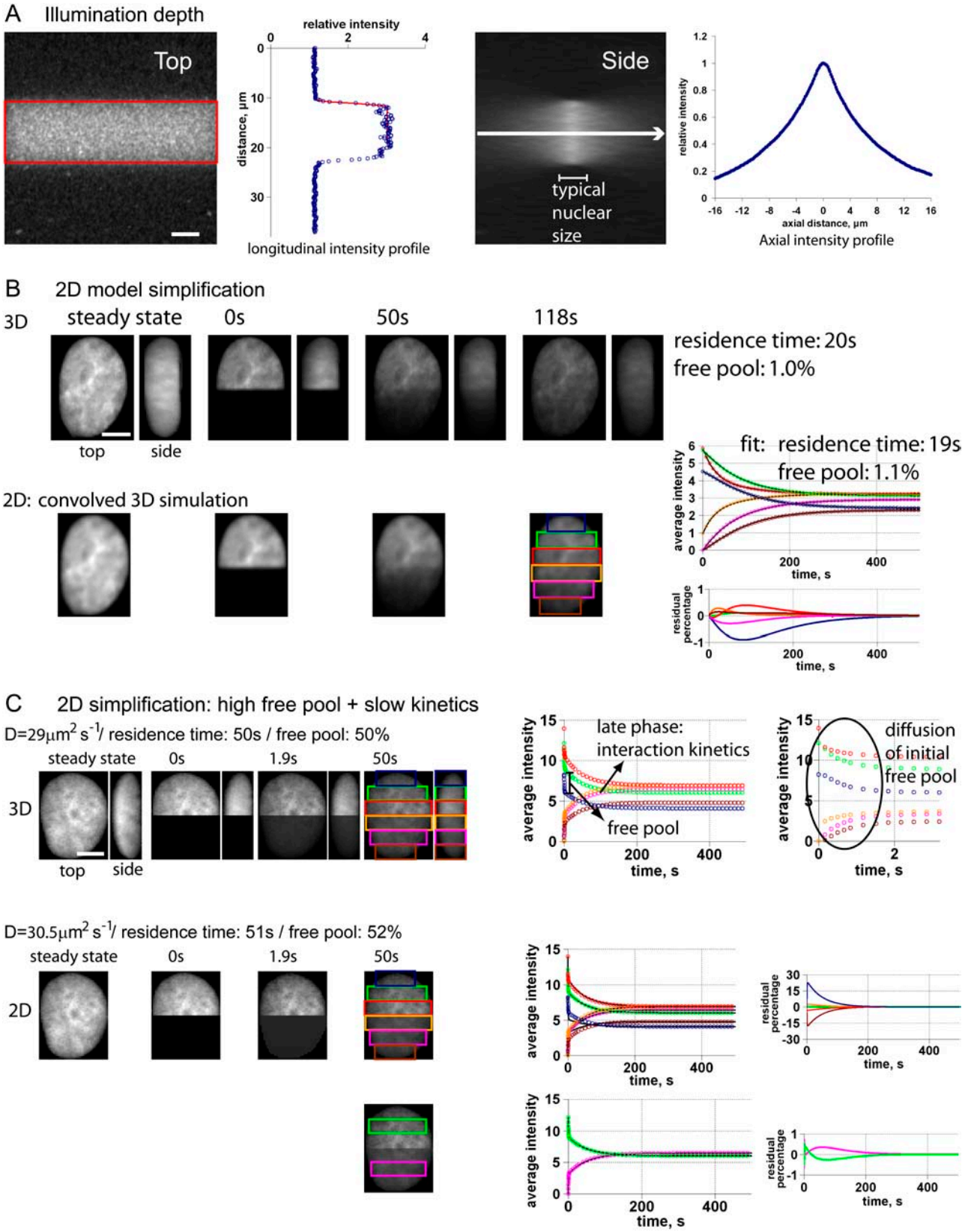

FIGURE 3 Two-dimensional simplification. (*A*) PAGFP-RCC1 fixed in a 30% acrylamide gel was photoactivated in the red region using a 40× iris objective with a numerical aperture fixed to 1.0, seen from the top and the side. Scale bar: 5 μm. The longitudinal profile shows the average intensity of the profile generated by photoactivation in the confocal section where photoactivation was focused. The red curves correspond to a fit of half of this profile with the

images is not necessary and that a two-dimensional model is sufficient to characterize protein dynamics. To statistically test the two-dimensional simplification and the influence of the real geometry, we simulated photoactivation in three dimensions in seven different nuclei, ignoring the convolution and assuming an homogeneous axial illumination in this case. The quality of the fit and the parameters were the same as when the PSF was considered. Starting from $k_{off} = 0.05\ s^{-1}$, a low 1% free pool and a diffusion coefficient D of 29 $\mu m^2\ s^{-1}$ in three dimensions, and keeping $D = 29\ \mu m^2\ s^{-1}$ in two dimensions, the two-dimensional fit gave $k_{off} = 0.051\ s^{-1} \pm 0.001\ s^{-1}$ and a free pool of 1.04% ± 0.01%, with residual differences between the two- and three-dimensional simulations below 1%.

We found only one particular case where the two-dimensional simplification is invalid, i.e., when the percentage of free fluorescent proteins is large and the dissociation of proteins from chromatin is slow compared to diffusion. This case represented in Fig. 3 *C* is characterized by an early phase of diffusion of free proteins when there is no significant contribution of the chemical interaction (Fig. 3 *C*, *zoom* of the *early part of the plot*), followed by a slower phase corresponding mostly to the dynamics of the interaction. The intensity amplitude of the early phase corresponds to the amount of free proteins, which fill the nonactivated half of the nucleus homogeneously according to the assumptions of the two-dimensional simplification (Fig. 3 *C*, *second row*, time 1.9 s). On the other hand, the three-dimensional simulation predicts an inhomogeneity due to the variable depth of the nucleus, which makes the two-dimensional simplification invalid when one tries to fit all the regions to the model (Fig. 3 *C*, *plots* of *second row*). Nevertheless we observed that when we fitted only the two regions depicted on the third row of Fig. 3 *C*, we could estimate the three parameters, D, free pool, and k_{off} with good precision, with residual differences between three-dimensional simulation and two-dimensional fit below 1%. Starting from $D = 29\ \mu m^2\ s^{-1}$, $Free = 50\%$, and $k_{off} = 0.020\ s^{-1}$ in three dimensions, the two-dimensional fit gave $D = 32\ \mu m^2\ s^{-1} \pm 1\ \mu m^2\ s^{-1}$, $Free = 52\% \pm 1\%$, and $k_{off} = 0.020 \pm 0.001\ s^{-1}$ for eight nuclei. In all other cases, the two-dimensional simplification was satisfactory for all nuclear regions. When the free pool is small enough, the amplitude of the first phase is too small to contribute to the fit, and when the interaction is fast enough, the first purely diffusive phase is no longer visible.

In conclusion, we could show that within the geometry of the nucleus of intact cells, a simplified two-dimensional reaction-diffusion model can globally describe the mobility of chromatin-interacting proteins with good precision. In cases where the free pool is high and the interaction slow compared to diffusion, the parameter estimation must be restricted to certain regions, but such cases are easy to identify before parameter estimation, as they show clear biphasic redistribution kinetics (see also the representative case of PAGFP-SUV39H1-H320R, below).

Calibration of nuclear viscosity

The model contains three parameters: the diffusion coefficient, the fraction of unbound proteins, and the dissociation rate or its inverse, the residence time of the interaction with chromatin. As can be seen on Fig. 4 *A*, PA experiments will not always allow us to identify all three parameters, because in some cases, different combinations of parameters fit the data equally well. In such cases, we calculated the diffusion coefficient independently from the model based on the molecular weight of the protein and the viscosity of the nucleoplasm. The apparent viscosity of the nucleoplasm was calibrated using PAGFP alone as an inert probe regarding binding interactions in the nucleus.

Nucleoplasmic PAGFP diffusion was probed by photoactivating half of the nucleus and measuring its redistribution over time as described above (Fig. 4 *B*). The pure diffusion model Eq. 1 was simulated in two dimensions, using an empirical method proposed by Siggia et al. (39) that we validated for the nucleus the same way as in the previous section (see Supplementary Material 2 and Fig. S2 for details). Nuclear PAGFP photoactivation was performed on 67 nuclei. The example shown in Fig. 4 *B* shows that the fit is qualitatively very close to the data, with residuals below 6%. On average, we measured a two-dimensional diffusion coefficient of 40.6 $\mu m^2\ s^{-1} \pm 3.8\ \mu m^2\ s^{-1}$. Given that the GFP diffusion coefficient in water is 87 $\mu m^2\ s^{-1}$ at room temperature (40,41) and that water viscosity drops from 1.00 to

FIGURE 3 (Continued)
error function. The axial intensity profile corresponds to the profile of illumination in depth along the arrow of the image. (*B*) Simulation of a photoactivation experiment in three dimensions, using the depth profile from panel *A* and a Gaussian radial PSF for the photoactivation profile (*first row*, *total intensity top* and *side projection*), and two-dimensional observation of the simulation, using the same depth profile and radial PSF as for the photoactivation profile (*second row*). The first images of each row represent the steady-state distribution of fluorescence and the following represent the fluorescence redistribution. The first plot shows the average fluorescence intensity over time of the six regions depicted on the last images of the two-dimensional sequence (*circles*) and the fit using the simplified two-dimensional model (*solid curves*). The second plot represents the residuals, <1% for the six regions, between the three-dimensional simulations and the two-dimensional fit. (*C*) Three-dimensional simulation with a higher percentage of free proteins, starting from cell stably expressing PAGFP-SUV39H1 (*first row*). The second plot in the first row is a zoom of the early phase of the first plot and shows the diffusion of the initial free pool of fluorescent proteins. The amplitude of this early phase is related to the amount of free proteins. The late phase visible on the first plot corresponds mostly to the kinetics of the interaction. In this case, the same regions as in *B* cannot be well fitted with the two-dimensional simplified model (*second row*) with residuals reaching 25%, but it improves drastically (see *solid curves* and *residuals* of the *third row*) and parameters are close to the three-dimensional situation when one uses only the two regions depicted on the image of the third row. Scale bars: 5 μm.

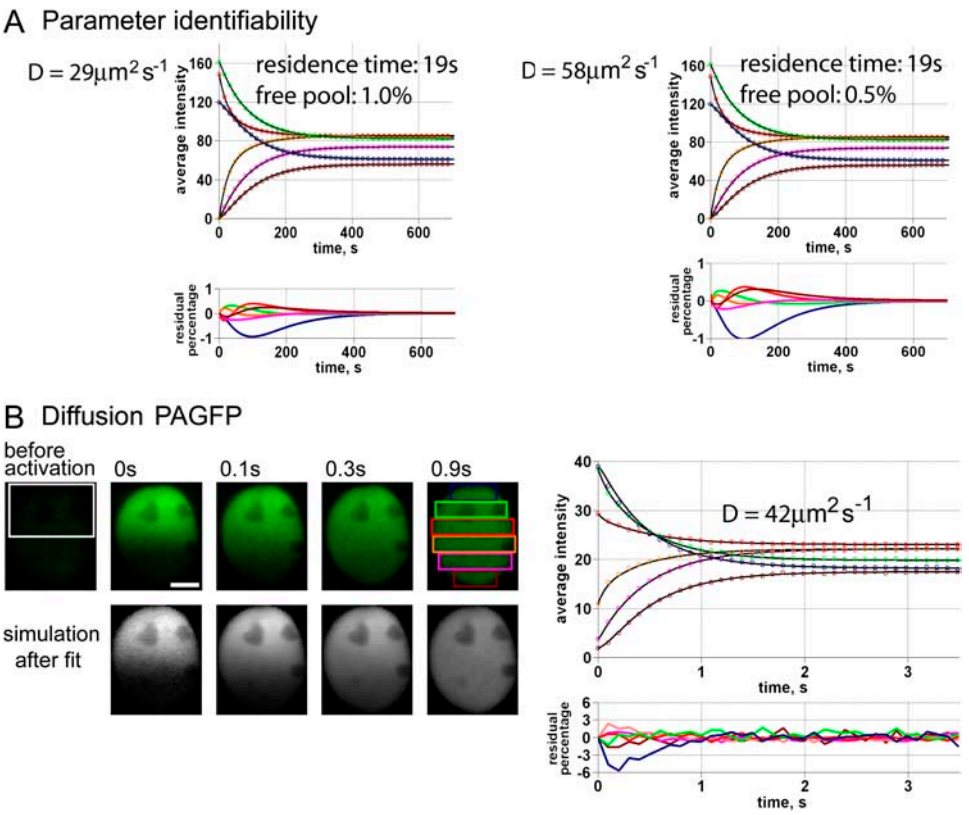

FIGURE 4 Parameter identifiability. (*A*) Fit and residuals for Fig. 3 *B* starting from two different fixed diffusion coefficients. It should be noted that the fits are almost similar, showing that in such a case the diffusion constant has to be determined separately to be able to estimate the other parameters. (*B*) PAGFP photoactivation. The nucleus was photoactivated (*open region*, *first image*) and imaged over time (*first row*). The intensities of the six regions depicted on the last image were plotted over time (*upper plot*, *circles*) and fitted (*solid curves*). Residuals are below 6% (*lower plot*). The sequence on the second row is the simulation using the parameter from the fit. Scale bar: 5 μm.

0.69 cP between 20°C and 37°C (42), we found the apparent viscosity of the nucleoplasm to be ~3.1 times higher than water, consistent with the literature (43–45).

Knowing the apparent viscosity, the diffusion coefficient of chromatin-interacting proteins was then calculated from the mass of the protein, using the Stokes-Einstein relation,

$$D = kT/(6\pi\eta R), \tag{5}$$

D is the diffusion coefficient, k the Boltzmann constant, T the temperature, η the viscosity, and R the spherical radius of the molecule. We approximated the radius to be proportional to the cubic root of its mass, yielding

$$D_{\text{protein}} = D_{\text{PAGFP}}(m_{\text{PAGFP}}/m_{\text{protein}})^{1/3}, \tag{6}$$

with m_{protein} as the molecular weight of the protein (Table 1). As all our proteins of interest were of similar size, their diffusion coefficient was estimated to ~30 $\mu m^2 s^{-1}$. This is only an approximation, which likely contributes an uncertainty of up to a factor of 2 in the diffusion coefficient.

Measuring chromatin interactions with the model

We then applied the model to simulate photoactivation experiments of PAGFP fusion proteins to analyze the interactions of RCC1, SUV39H1, and its hyperactive mutant SUV39H1-H320R, and the five human isoforms of H1 with chromatin. We found two classes of behavior. The most common, instantaneous interaction with chromatin is illustrated in detail by PAGFP-RCC1. Despite large differences in the timescales of redistribution, the dynamics of SUV39H1 and H1 isoforms were extremely similar to that of RCC1. The second class of behavior, a noninstantaneous interaction with chromatin, is illustrated by the hyperactive mutant of SUV39H1.

PAGFP-RCC1 interacts instantaneously with chromatin and 2% of the protein pool is unbound in steady state

RCC1 interacts with the core histones H2A and H2B (24). FRAP experiments on GFP-RCC1 have already shown that its association with chromatin is dynamic: the half-time of recovery was found to be ~2 s for a bleached spot in U2OS cells (46), and ~10 s for a bleached stripe in tsBN2 (47), and one study fitted the recovery with a diffusive model with an apparent diffusion coefficient of 0.5 $\mu m^2\ s^{-1}$ in 3T3 cells (48). We performed the experiment as described before for PAGFP alone, using transient expression of PAGFP-RCC1 in NRK cells (Fig. 5 *A*). The model using Eq. 4 was fitted to the measured intensities using $D = 30\ \mu m^2\ s^{-1}$ (Table 1), yielding as an initial set of parameters a dissociation rate k_{off} of 2 s^{-1}, i.e., a residence time of 0.5 s, and an unbound pool *Free* of 2.9%. The fit was qualitatively in good agreement with the data (Fig. 5 *A*) and residuals did not exceed 8% (Fig. 5 *A* and Supplementary Material, Fig. S3 *A*, for the details of the residuals).

TABLE 1 Fit results

Protein name	Molecular weight	Diffusion coefficient	Percentage of free proteins	Dissociation constant	*n*
PAGFP-RCC1	74 kDa	30 $\mu m^2 s^{-1}$ imposed	2.1% ± 0.6%	>0.15 s^{-1}	19
PAGFP-SUV39H1	77 kDa	30 $\mu m^2 s^{-1}$ imposed	36% ± 8%	>0.9 s^{-1}	20
PAGFP-SUV39H1-H320R	77 kDa	5.7 ± 1.6 $\mu m^2 s^{-1}$ fit*	57% ± 17%	$5.1.10^{-3}$ ± $2.2.10^{-3}$ s^{-1}	8
H1.1-PAGFP	50 kDa	34 $\mu m^2 s^{-1}$ imposed	0.09% ± 0.04%	>6e–3s^{-1}	19
H1.2-PAGFP	49 kDa	34 $\mu m^2 s^{-1}$ imposed	0.08% ± 0.03%		12
H1.3-PAGFP	50 kDa	34 $\mu m^2 s^{-1}$ imposed	0.05% ± 0.02%		10
H1.4-PAGFP	50 kDa	34 $\mu m^2 s^{-1}$ imposed	0.04% ± 0.01%		11
H1.5-PAGFP	50 kDa	34 $\mu m^2 s^{-1}$ imposed	0.03% ± 0.01%		13

Diffusion coefficients come from the fit unless the model could not estimate them, in which case they were imposed. When the lower limit of dissociation rate is given, it means that the actual value is not measurable experimentally. The value *n* is the number of nuclei investigated for each construct.
*As the fitted diffusion coefficient is much lower than expected from the size of the protein, it can be interpreted as an apparent one, corresponding to an instantaneous reaction.

We then tested the certainty of the parameters for PAGFP-RCC1 by plotting the sum of the square of the differences between experimental data and simulation for different combinations of k_{off} and *Free*. Fig. 5 *B* shows the importance of exploring parameter space in this manner: the dark-blue region represents the area of parameters that fit the data qualitatively well (see Supplementary Material, Fig. S3 *B*, for simulations with parameters of this area), and this region is infinite toward the high values of k_{off}. By contrast, the percentage of free molecules could be identified as 2.9% ± 0.2% (*white bounded region* on Fig. 5 *B*) (could be up to 4.3%; *isolated white bounded region* on Fig. 5 *B*) and the lower limit of the dissociation rate k_{off} could be determined as 0.4 s^{-1}, i.e., a maximum residence time of 2.5 s (could be as low 0.2 s^{-1}).

From the chemical point of view, this means that the interaction of PAGFP-RCC1 is too transient to be accurately measured by fluorescence perturbation methods such as PA/FRAP. At first glance, this is counterintuitive, as the fluorescence redistribution of PAGFP-RCC1 was very slow compared to PAGFP alone (compare Fig. 1, *A* and *C*, and Figs. 4 *B* and 5 *A*). The speed of redistribution of RCC1, however, does not reflect the length of the interaction but rather its affinity. The small fraction of free molecules, 2.9%, are very often trapped on their ubiquitous binding sites, and although they reside in the bound state for short times, they can therefore not diffuse efficiently over long distances and need long times to redistribute across the nucleus.

In such a case, the reaction-diffusion model Eq. 4 can be strongly simplified because the interaction can be considered as instantaneous. For homogeneously distributed binding sites, it has been shown that the model then becomes effectively diffusive (49), and also for an inhomogeneous distribution of binding sites we can rewrite the model to (Appendix B)

$$\frac{\partial i(\vec{r},t)}{\partial t} = D * Free * i^{st}_{average} \Delta\left(\frac{i(\vec{r},t)}{i^{st}(\vec{r})}\right), \qquad (7)$$

with $i(\vec{r},t)$ the local fluorescence intensity. For relatively homogeneous distributions of binding sites Eq. 7 is approximately a diffusive equation with an effective diffusion coefficient equal to the product of the diffusion coefficient with the percentage of free proteins, *D*Free*. Thus, the speed of redistribution depends only on the diffusion coefficient of the protein and on the percentage of protein available for diffusion in steady state, but not on the kinetics of the interaction. If the unbound fraction is low, the fluorescence redistribution is slow. Fig. 5 *C* shows a fit performed on the same data as on Fig. 5 *A* using Eq. 7. The residuals are as expected identical and the estimated fraction of free protein is very similar, 2.8%. It should be noted that this would lead to an effective diffusion coefficient of *D*Free* = 0.8 μm^2 s^{-1}, close to already published values (48), but the correct interpretation possible by the model is that 97% of RCC1 is bound to chromatin and that the interaction can be considered as instantaneous. The analysis was performed on 19 nuclei and led to an average percentage of free molecules of 2.1% ± 0.6% (Table 1), with the uncertainty linked to our estimation of the diffusion coefficient (see above).

PAGFP-SUV39H1 interacts instantaneously with chromatin and 36% of the protein pool is unbound in steady state

SUV39H1 is a methyltransferase that specifically methylate lysine 9 of histone H3 (25), a key epigenetic modification involved in gene silencing. SUV39H1 binds to core histones without apparent preferences in vitro (50).

Photoactivation experiments to probe SUV39H1 interaction with chromatin were performed in NRK cells stably expressing PAGFP-SUV39H1. Models were simulated and fit to the data with a diffusion coefficient of 30 μm^2 s^{-1}. Fluorescence redistribution could be fit equally well by the reaction-diffusion model Eq. 4 (data not shown) and by the instantaneous reaction model Eq. 7 (Fig. 6, *A–C*). Thus, similar to PAGFP-RCC1, the percentage of free protein and only the lower limit of the dissociation rate could be determined. The analysis of 20 nuclei led to an average free protein pool of 36% ± 8% and a lower limit of dissociation rate of 0.9 s^{-1}, i.e., a residence time of, at most, 1.1 s determined from the parameter space analysis (Fig. 6 *B*).

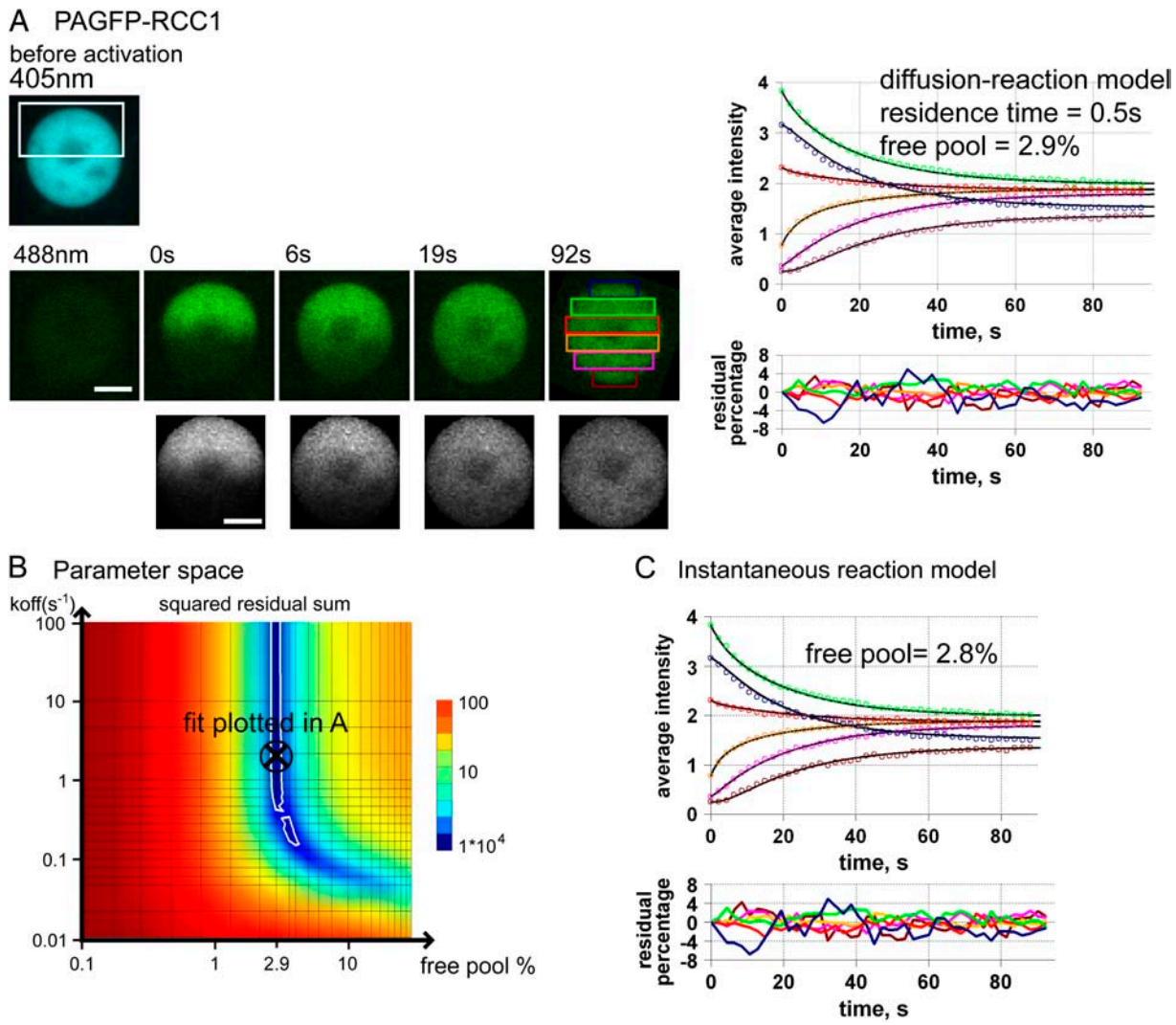

FIGURE 5 PAGFP-RCC1. The percentage of free molecules and only the lower limit of dissociation rate can be estimated. (*A*) Nucleus of NRK cell transiently expressing PAGFP-RCC1, acquired at 405 nm, low power, and 488 nm before photoactivation (*first two images*) and at 488 nm after activation (*second row*). The plots represent the average intensity over time of the regions depicted on the last image (*circles*) and the fit (*solid curves*, *first plot*), and the residuals (*second plot*). The simulation using the parameters from the fit is shown on the last image row. Scale bar: 5 μm. (*B*) Color-coded sum of the square of the residuals for different values of dissociation rates k_{off} and percentage of free proteins. The black-cross fit on the parameter space corresponds to the fit in *A*. The regions with white boundaries correspond to the values of sum of residual squares that are less than the double of the one corresponding to the fit. (*C*) Same plots as in panel *A*, but using a instantaneous reaction model. Note that it is almost completely similar to panel *A*.

Five isoforms of H1-PAGFP interact instantaneously with chromatin and have <0.1% of unbound protein in steady state

Histones H1 are components of the nucleosomal subunits that play an important role in chromatin structure and function (26). The dynamics of some isoforms have already been investigated by FRAP (3,51), which gave a recovery in the range of 1 min for a small bleached spot, a time that was interpreted as the residence time.

We stably expressed five isoforms of H1-PAGFP, H1.1-5, in NRK cells. Models were simulated using a diffusion coefficient of 34 $\mu m^2\ s^{-1}$. All isoforms showed very similar behavior, which is illustrated for H1.1-PAGFP in Fig. 6 *D*. The behavior of fluorescence redistribution is similar to PAGFP-RCC1 and PAGFP-SUV39H1. It could be fit by the reaction-diffusion model Eq. 4 (data not shown) as well as by the instantaneous reaction model Eq. 7 (Fig. 6 *F*), yielding an average fraction of free protein of 0.09% $\pm$ 0.04% ($n = 19$). Due to the stiffness of the reaction-diffusion model Eq. 4 with such a low percentage of unbound molecules, we could not explore parameter space as exhaustively as for PAGFP-RCC1 and PAGFP-SUV39H1 at reasonable computational cost. We therefore only plotted the sum of the residual squares for different values of dissociation rate k_{off}, fixing the percentage of free proteins that

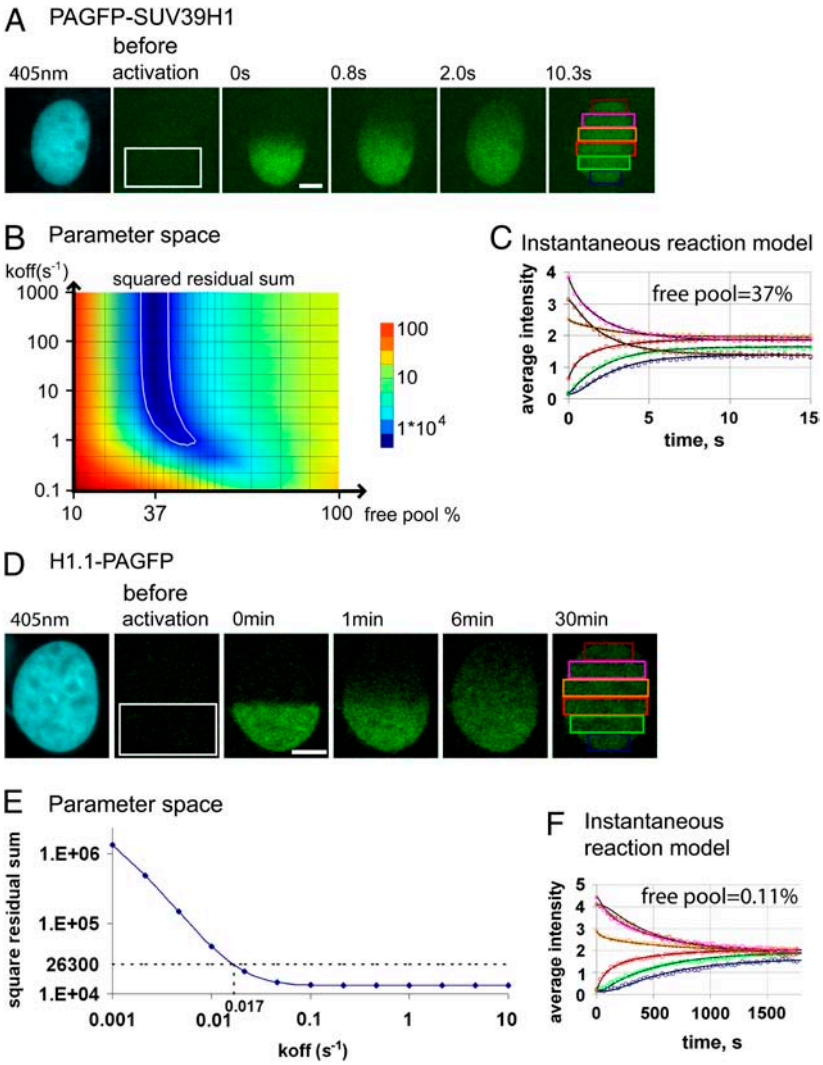

FIGURE 6 PAGFP-SUV39H1 and H1.1PAGFP. Different timescales but same conclusions as for PAGFP-RCC1; only the lower limit of dissociation rate can be estimated. (*A*) Nucleus of an NRK cell stably expressing PAGFP-SUV39H1, acquired at 405 nm, low power, before activation (*first image*) and at 488 nm before and after activation of half of the nucleus (*open region*, *second image*). (*B*) Parameter space as in Fig. 5 *B*. (*C*) Instantaneous reaction model for PAGFP-SUV39H1, almost similar to a reaction-diffusion model (not shown). (*D*) NRK cell stably expressing H1.1-PAGFP. Images as in *A*. (*E*) The parameter space represents the sum of the squares of the residuals for different values of dissociation rates k_{off}, the percentage of free proteins being fixed to the value given by the fit. The horizontal dashed line corresponds to the double of the minimum of this sum, giving the lower limit of dissociation rate 0.017 s^{-1} depicted on the plot. (*F*) Instantaneous reaction model for H1.1-PAGFP, similar to a reaction-diffusion model (not shown). Scale bars: 5 μm.

best fit the data (Fig. 6 *E*). Because of the curved distribution of best-fitting k_{off} values (see Figs. 5 *B* and 6 *B*), this procedure could lead to an underestimation of the lowest possible limit of k_{off} of a factor of 2.9 for PAGFP-RCC1 and 2.4 for PAGFP-SUV39H1 (Supplementary Material, Fig. S4). Because the lower limit of k_{off} is 0.017 s^{-1}, according to the plot (Fig. 6 *E*), we can estimate it to $6*10^{-3}$ s^{-1}—i.e., a residence time of no more than 170 s, with a correction factor of 2.7.

The results for the four other isoforms are summarized in Table 1. The percentages of free protein are all similar to H1.1-PAGFP and, as the levels of noise are comparable, the lower limits of the dissociation rate are also expected to be similar (see Discussion).

It should be noted that the model shows a complete recovery of fluorescence, contrary to what has been published for H1°-GFP and H1c-GFP (3). It should also be noted that our timescale of fluorescence redistribution is much longer than the published ones (3,51), notably because our photoactivated regions are much larger, which directly affects a diffusion-limited redistribution (see Discussion).

Hyperactive PAGFP-SUV39H1-H320R is bound for 200 s on chromatin

The hyperactive mutant of PAGFP-SUV39H1-H320R is mutated in the catalytic SET domain of the enzyme, unexpectedly resulting in an increase of activity (25). It was transiently expressed in NRK cells. Likely due to the toxicity of the mutant in living cells, only very low levels of expression could be observed, which explains the lower signal/noise ratio of the images compared to the other proteins studied here (Fig. 7). In contrast to the wild-type protein, most nuclei exhibited a high percentage of diffusive proteins that led to a fast early redistribution followed by a slower phase limited by the kinetics of the chemical interaction (Fig. 7, *plots*), as already mentioned for validation of the two-dimensional model. In this case, all three parameters of

the reaction-diffusion model could be identified using the two regions depicted on the images of Fig. 7. The fit yielded an average diffusion coefficient of 5.7 $\mu m^2 s^{-1} \pm 1.6\ \mu m^2 s^{-1}$, a percentage of free diffusive proteins of 57% ± 17% and a dissociation rate of $5.1*10^{-3}\ s^{-1} \pm 2.2*10^{-3}\ s^{-1}$, i.e., a residence time of 196 s ($n = 8$).

The diffusion coefficient of 5.7 $\mu m^2\ s^{-1}$ is nevertheless smaller than 30 $\mu m^2\ s^{-1}$ expected from the size of the protein. The diffusion coefficient of the early redistribution, may therefore also correspond to an effective diffusion coefficient, reduced by a relatively large fraction of protein bound in an instantaneous interaction, like in the case of wild-type PAGFP-SUV39H1. The redistribution of fluorescence would then be due to two types of interactions: one fast, compared to diffusion that led to an apparent diffusive process at early times similar to the wild-type protein; and one slow, with a dissociation rate of $5.1*10^{-3}\ s^{-1}$ and a percentage of free proteins, i.e., proteins that are not bound in the second interaction, of 57%. To understand the estimated parameters in the context of two reactions, we wrote the reaction-diffusion equations for a model where the second interaction is a stabilization of the first:

$$free + C \underset{k_{off1}}{\overset{k_{on1}}{\rightleftharpoons}} bound1$$
$$bound1 \underset{k_{off2}}{\overset{k_{on2}}{\rightleftharpoons}} bound2.$$

If the first interaction can be considered as instantaneous, then we can write the differential equations describing the system in a similar way to Eq. 4 (see Appendix C). The interpretation of the dissociation rate remains the same: it corresponds to k_{off2}. What we call here the free pool of 57% is actually the ratio$([free(\vec{r})]+[bound1(\vec{r})])/total$. The fraction of free proteins regarding only the first reaction $[free(\vec{r},t)]/([free(\vec{r},t)]+[bound1(\vec{r},t)])$is the ratio of the apparent diffusion coefficient with the real D of the free proteins (see Appendix C), i.e., 19% assuming a diffusion coefficient of 30 $\mu m^2\ s^{-1}$. The real fraction of free proteins, $[free(\vec{r})]/total$, is therefore the product of these 19% with the apparent free pool of 57%, i.e., 11%.

DISCUSSION

Comparison to other FRAP experiment and analysis methods

One of the main experimental approaches used to quantitatively characterize diffusion (12,52) and reactions limited by diffusion (18) consists in bleaching a small spot and analytically analyzing the fluorescence recovery in this spot. Compared to this classical FRAP approach, the method presented here requires more computational skills and more time, but offers several advantages. First, the theoretical analysis of the spot-bleaching technique has always assumed an infinite system, a questionable assumption as most cellular compartments are not very large compared to the bleached spot. By contrast, our method takes the complete geometry of the sample, including boundaries, into account. Moreover, the spot technique requires the size and shape of the bleaching intensity profile to be known (12), which requires nontrivial optical calibrations. Our method is independent of the geometry of bleaching/photoactivation, and does not require the characterization of the amount of bleaching, as in certain cases for the spot technique (12). Furthermore, spots are typically chosen small to make the rest of the sample infinite, as possible leading to noisy data. Here, we measure the intensity in the whole nucleus, offering a much better precision in model validation and parameter estimation. Finally, fluorescence distributions are typically considered as homogeneous in space to simplify the analysis, whereas here such simplification is not needed: the distributions of both bound and unbound molecules are taken into account, allowing higher precision and a convincing validation of the model.

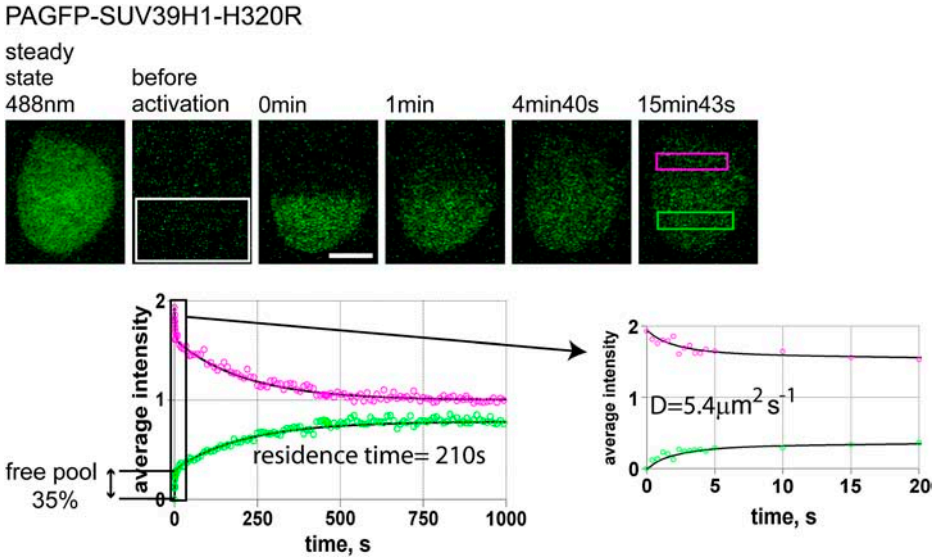

FIGURE 7 PAGFP-SUV39H1-H320R case. Free pool of 35% and residence time of 210 s. Nucleus of NRK cell stably expressing the hyperactive PAGFP-SUV39H1-H320R, acquired at 488 nm. Contrary to the other cases, the steady-state distribution was not measured at 405 nm as the signal was too low. The intensities of the two regions depicted on the last image are plotted (*circles*) and fitted (*solid curves*) as in Fig. 3 *C*. The second plot correspond to a zoom of the early part of the first plot.

Limits of residence times that can be measured by FRAP/PA

Three of the proteins we examined, RCC1, H1, and wild-type SUV39H1 illustrate that for generic chromatin-interacting proteins, the binding reaction can appear instantaneous in FRAP/PA experiments and that only a lower limit for k_{off} can be determined from such experiments. Exploiting the possibility to do in silico experiments with our reaction-diffusion model, we wanted to generally test the dependence of the ability to identify the dissociation rate on the percentage of free proteins, which reflects the affinity of the interaction in steady state.

To this end, we used a simplified one-dimensional reaction-diffusion model with a homogeneous distribution of binding sites and a hypothetical protein with a diffusion coefficient of 30 $\mu m^2\ s^{-1}$. For given percentages of free protein, we tested at what dissociation rate the reaction-diffusion model can no longer be discriminated from an instantaneous reaction model with a tolerance of 5% between the two models (see Supplementary Material 3 for details). Fig. 8 shows that the method has the best sensitivity for high dissociation rates if ~30% of the protein is unbound, then dissociation rates up to ~30 s^{-1}— i.e., residence times as short as 33 ms can be identified. For amounts of free protein from 0 to 30%, the limit that can be estimated for the dissociation rate increases proportionally with the free fraction. For higher percentages of free proteins, the identifiable limit of dissociation rate decreases rapidly again with the free fraction, presumably because the contribution of the bound fraction to the fluorescence equilibration diminishes significantly. These in silico results are in good agreement with our experimental data on the instantaneous interactions of SUV39H1, RCC1, and H1.1 with chromatin. For all three proteins, the limit of the identifiable dissociation rate increased with the free fraction (Fig. 8, *vertical lines*).

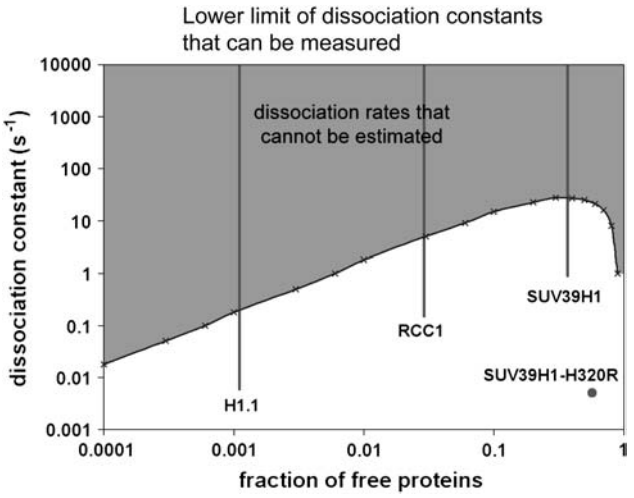

FIGURE 8 Estimation of dissociation rates. Experimental and theoretical limits. Positions of the different constructs on the diagram of fraction of free proteins versus dissociation rates. The curve between the shaded and the unshaded regions corresponds to the limit of dissociation rates that can be estimated, with a tolerance of 5%, determined from the comparison between reaction-diffusion and instantaneous reaction models. The shaded region corresponds to the space where the dissociation rate cannot be estimated. It should be noted that although the dissociation rates of H1.1-PAGFP, PAGFP-RCC1, and PAGFP-SUV39H1 cannot be determined, their limit is outside the shaded region, likely because this limit also takes into account data noise and systematic errors.

Thus, for cases where interactions appear instantaneous, FRAP/PA experiments are suitable to measure the amount of free protein but give limited information on the kinetics of the interaction. As illustrated over the parameter space in Fig. 8, combinations of dissociation rate and unbound fraction that can be physiologically expected can easily be found in the half-space, where k_{off} cannot be identified. Thus there is clearly a need for complementary methods to measure transient biochemical interactions in living cells. Fluorescence correlation spectroscopy may be a good alternative to access this information as the timescales accessible by this technique are orders-of-magnitude shorter than with FRAP/PA.

General implications for the interpretation of FRAP and PA experiments

Slow redistribution does not mean stable interaction

Our study clearly shows that the analysis of FRAP and PA experiments to determine interaction parameters is not trivial. Simplifying the reaction-diffusion process that typically drives the mobility of nuclear proteins to a model where diffusion is ignored has been often used in recent studies (e.g., (6,21)), but may lead to wrong parameter values and biological interpretations if the simplification is not justified. It is clear from our data that a long timescale of redistribution compared to diffusion alone is not indicative of long-lived interaction, because an instantaneous interaction with a ubiquitous binding site can lead to any timescale of recovery depending on how small the unbound fraction of protein is. Such behavior can then be modeled by an instantaneous reaction equation limited by an apparent diffusion coefficient that can take any value below the real diffusion coefficient, depending on the free protein fraction available for diffusion. A long timescale of fluorescence recovery may correspond to a long-lived interaction, but it may also correspond to a very transient interaction with high affinity.

In this context, the number of free binding sites may influence the dynamics of fluorescence recovery. This could notably explain why the H1 isoform H1° becomes more dynamic when HMG proteins, which compete with H1 for the same binding sites, is microinjected into nuclei (53): the reduction in the number of binding sites for H1° could increase the amount of free H1°, leading to a faster fluorescence recovery; likely, however, without any change in association and dissociation kinetics.

Half-time of recovery is not a measure of residence times

It is also clear that the half-time of recovery that is typically measured in FRAP studies may not be related at all to the

residence time of a protein on its binding site. In this study, the examples of RCC1, SUV39H1, and of the different H1 isoforms clearly illustrate this, because their residence time cannot be measured. Even in the case of SUV39H1-H320R, the half-time of recovery is not informative: since more than half of the proteins are considered as unbound and the dissociation rate is small, the early fast recovery will contribute to more than half of the complete recovery. Therefore the half-time of recovery will relate mostly to the early, diffusive part of the recovery curve, and not to the later part, which contains the information about the residence time.

Moreover, whereas kinetics of chemical reactions depend only on concentration changes over time, diffusive processes depend on both time and space. This means that half-times of recovery can strongly depend on the geometry of photobleaching/activation: for a purely diffusive process the characteristic time of diffusion is roughly proportional to the square of the spatial scale of fluorescence recovery. For example, bleaching a spot of ~ 1 μm in diameter or bleaching half of a nucleus, ~ 5 μm in diameter, will result in a 25-fold increase in half-time of recovery. This explains why published half-times of recovery can be so different for a given protein, e.g., GFP-RCC1 (46,47). Therefore the half-time of recovery that is typically measured in FRAP experiments should only be interpreted as a measurement of the dynamics of the protein and not as a residence time on a binding site or a diffusion coefficient, unless that is clearly justified. Moreover, in cases where diffusion is limiting fluorescence redistribution, half-times of fluorescence recovery can only be compared between identical experimental geometries.

On the other hand, trying to model fluorescence recovery by a diffusive process with popular analytical solutions (12) may also lead to misinterpretation of the results. This method only works for purely diffusive processes or when the interactions are very fast compared to diffusion, in which case it will yield an effective diffusion coefficient lowered by the fraction of unbound protein. It is not applicable in any other cases.

Deriving equilibrium dissociation constant and association rate in living cells

From the reaction-diffusion Eq. 3 it can be seen that k_{on} cannot be estimated from photobleaching/activation without information on the concentration of free binding sites. Likewise the equilibrium dissociation constant K_D, which is the product of *Free*/(1-*Free*) and the concentration of free binding sites, cannot be determined without the latter.

PAGFP-RCC1 interacts with histones, which in cells are assembled into nucleosomes, therefore

$$K_D = \frac{[\text{PAGFP}-\text{RCC1}^{\text{free}}][\text{Nucleosome}]}{[\text{PAGFP}-\text{RCC1}^{\text{bound}}]} = \frac{Free}{1-Free}[\text{nucleosome}],$$

where [nucleosome] is the concentration of free nucleosomes available for RCC1 binding. Here,

$$K_D = 0.02 * [\text{nucleosome}].$$

The amount of free nucleosomes available for RCC1 binding is nevertheless not known and cannot be estimated from our experiments as nucleosomes can be occupied by RCC1 tagged and untagged, as well as by many other nucleosome binding proteins, whose concentrations and affinities are unknown. We can therefore only estimate its upper limit, assuming that all nucleosomes are free. Given that a rat cell contains $\sim 6*10^9$ basepairs of DNA and nucleosomes repeat at intervals of ~ 200 basepairs, we can estimate that a rat cell contains $\sim 3*10^7$ nucleosomes (54). As the nuclear volume is ~ 0.7 pl, the total concentration of nucleosomes is ~ 70 μM. If we assume one binding site per nucleosome, the dissociation constant K_D is then smaller than 1.4 μM. The real value is the product of this upper limit by the fraction of free binding sites, a number difficult to estimate. It should be noticed that K_D has been estimated to ~ 5 nM in vitro (55), suggesting that only $\sim 0.5\%$ of nucleosomes are available for RCC1 binding in steady state.

The case of H1 is very similar: as one linker histone H1 binds to one histone octamer, like RCC1, this leads to an upper limit for the dissociation constant K_D of 70 nM. Like in the case of RCC1, the real dissociation constant is the product of this upper limit with the fraction of free histones. In vitro H1 binds nucleosomes with a K_D of 7.4 nM (56), suggesting that $\sim 10\%$ of nucleosomes are available for binding to H1 in steady state.

Implications for dynamics of protein-DNA interactions

The problem of specific protein-DNA recognition has been a challenging issue since 1970 when the *Escherichia coli* lac repressor was found to find its target at a much higher rate than predicted for a diffusion-controlled process (57). It was therefore suggested that more elaborate mechanisms than simple three-dimensional diffusional collisions should occur (58,59). Notably it has been proposed that proteins can interact with nonspecific sequences of DNA at low affinity and then diffuse along the DNA molecule in one dimension, restricting the volume which has to be searched by the protein and resulting in more efficient encounters with specific sites. Most FRAP studies on chromatin interacting proteins have been taken to suggest that the three-dimensional diffusional collision process was universal in living eukaryotic cells (60). The suggestion that chromatin interacting proteins can diffuse all over the nucleus before interacting with a binding site is in contradiction with the very high association rates found for the lac repressor. The interpretation of FRAP data was based on the assumption that diffusion does not limit fluorescence recovery, an assumption not validated in

most studies. Here we could see that in the cases of RCC1, Suv39H1 and H1, this assumption is not valid. In the context of a three-dimensional reaction-diffusion model these individual proteins will therefore reassociate with a binding site in close proximity, which could be compatible with a one-dimensional diffusion along DNA molecules. Our present study shows that FRAP studies showing rapid nuclear protein mobilities do not provide per se grounds to rule out the one-dimensional diffusion hypothesis for eukaryotic cells. It might therefore be worth considering testing it with appropriate methods.

APPENDIX A: REFORMULATION OF REACTION-DIFFUSION EQUATIONS USING STEADY-STATE FLUORESCENCE DISTRIBUTION

Equation 3 is the standard reaction-diffusion with immobile bound molecules:

$$\frac{\partial[\text{free}(\vec{r},t)]}{\partial t} = D\Delta([\text{free}(\vec{r},t)]) - k_{on}[C(\vec{r})][\text{free}(\vec{r},t)] + k_{off}[\text{bound}(\vec{r},t)]$$

$$\frac{\partial[\text{bound}(\vec{r},t)]}{\partial t} = k_{on}[C(\vec{r})][\text{free}(\vec{r},t)] - k_{off}[\text{bound}(\vec{r},t)]. \quad (8)$$

Our goal was to modify the product $k_{on}[C(\vec{r})]$ by using the spatial information we have in steady state to get parameters that do not depend on space anymore.

The steady-state intensity $i^{st}(\vec{r})$ is proportional to the sum of free and bound protein steady-state concentrations, with a proportionality coefficient A,

$$i^{st}(\vec{r}) = A([\text{free}(\vec{r})]^{st} + [\text{bound}(\vec{r})]^{st}), \quad (9)$$

where $[\ ]^{st}$ represents concentrations in steady state. In such conditions, we have local chemical equilibrium of

$$k_{on}[C(\vec{r})][\text{free}(\vec{r})]^{st} = k_{off}[\text{bound}(\vec{r})]^{st}, \quad (10)$$

and because of the expressions in Eq. 8 are equal to zero and because of Eq. 10, we have no gradients of free molecules:

$$D\Delta([\text{free}(\vec{r})]^{st}) = 0.$$

This means that $[\text{free}(\vec{r})]^{st}$ is actually a constant in space $free^{st}$. One can therefore write Eq. 10 as

$$k_{on}[C(\vec{r})] = (k_{off}/free^{st})[\text{bound}(\vec{r})]^{st}, \quad (11)$$

or, using Eq. 9,

$$k_{on}[C(\vec{r})] = k_{off}(i^{st}(\vec{r})/(A*free^{st}) - 1).$$

To get rid of the unknown proportionality coefficient A, we introduced a new parameter Free equal to the ratio of the total amount of free fluorescent molecules over the total amount of fluorescent molecules in the nucleus.

$$Free = \iiint free^{st} / \iiint (free^{st} + [\text{bound}(\vec{r})]^{st})$$

or

$$Free = A \iiint free^{st} / \iiint i^{st}(\vec{r}),$$

with $\iiint$ representing the sum over the whole nuclear volume. By dividing both terms of the ratio by the nuclear volume we see that Free is also proportional to the ratio of the average amount of free molecules, which is $free^{st}$ because this is a constant, and the average of steady-state intensity $i^{st}_{average}$:

$$Free = A * free^{st} * i^{st}_{average}.$$

Eq. 11 then becomes

$$k_{on}[C(\vec{r})] = \frac{k_{off}}{Free}(i^{st}(\vec{r})/i^{st}_{average} - Free),$$

which we noted $k_1(\vec{r})$ in the main text. $i^{st}(\vec{r})$ could be directly measured from images showing the steady-state distribution of fluorescent molecules. $i^{st}_{average}$ was determined by summing $i^{st}(\vec{r})$ over the whole nucleus and dividing it by the nuclear volume.

APPENDIX B: DIFFUSION-REACTION MODEL WITH INSTANTANEOUS REACTION

In such a case, the reaction-diffusion model,

$$\frac{\partial[\text{free}(\vec{r},t)]}{\partial t} = D\Delta([\text{free}(\vec{r},t)]) - k_1(\vec{r})[\text{free}(\vec{r},t)] + k_{off}[\text{bound}(\vec{r},t)]$$

$$\frac{\partial[\text{bound}(\vec{r},t)]}{\partial t} = k_1(\vec{r})[\text{free}(\vec{r},t)] - k_{off}[\text{bound}(\vec{r},t)], \quad (12)$$

can be simplified, because the fact that the reaction is instantaneous means that we always have chemical equilibrium even during the diffusion,

$$k_1(\vec{r})[\text{free}(\vec{r},t)] = k_{off}[\text{bound}(\vec{r},t)], \quad (13)$$

and therefore

$$\frac{\partial[\text{free}(\vec{r},t)]}{\partial t} = D\Delta([\text{free}(\vec{r},t)]). \quad (14)$$

Now the measured intensity $i(\vec{r},t)$ is proportional to the sum of the free and bound pool of proteins, with a coefficient of proportionality A,

$$i(\vec{r},t) = A([\text{free}(\vec{r},t)] + [\text{bound}(\vec{r},t)]) \quad (15)$$

or, using Eq. 13,

$$i(\vec{r},t) = A(1 + k_1(\vec{r})/k_{off})[\text{free}(\vec{r},t)]. \quad (16)$$

So from Eq. 12,

$$\frac{\partial i(\vec{r},t)}{\partial t} = AD\Delta([\text{free}(\vec{r},t)]), \quad (17)$$

or

$$\frac{\partial i(\vec{r},t)}{\partial t} = D\Delta\left(\frac{k_{off}}{k_{off} + k_1(\vec{r})} i(\vec{r},t)\right). \quad (18)$$

Given that $k_1(\vec{r})$ is defined as

$$k_1(\vec{r}) = k_{off} * (i^{st}(\vec{r})/i^{st}_{average} - Free)/Free, \quad (19)$$

Eq. 18 can be rewritten as

$$\frac{\partial i(\vec{r},t)}{\partial t} = D.Free.i^{st}_{average}\Delta(i(\vec{r},t)/i^{st}(\vec{r})).$$

APPENDIX C: DIFFUSION-REACTION MODEL WITH A FIRST INSTANTANEOUS REACTION AND A SLOW STABILIZATION

$$free + C \underset{k_{off1}}{\overset{k_{on1}}{\rightleftharpoons}} bound1$$
$$bound1 \underset{k_{off2}}{\overset{k_{on2}}{\rightleftharpoons}} bound2.$$

To simplify the writing of the equations, we consider here an homogeneous distribution of binding sites,

$$\begin{aligned}\frac{\partial[\text{free}(\vec{r},t)]}{\partial t} &= D\Delta([\text{free}(\vec{r},t)]) - k_{on1}[C][\text{free}(\vec{r},t)] \\ &\quad + k_{off1}[\text{bound1}(\vec{r},t)] \\ \frac{\partial[\text{bound1}(\vec{r},t)]}{\partial t} &= k_{on1}[C][\text{free}(\vec{r},t)] - k_{off1}[\text{bound1}(\vec{r},t)] \\ &\quad - k_{on2}[\text{bound1}(\vec{r},t)] + k_{off2}[\text{bound2}(\vec{r},t)] \\ \frac{\partial[\text{bound2}(\vec{r},t)]}{\partial t} &= k_{on2}[\text{bound1}(\vec{r},t)] - k_{off2}[\text{bound2}(\vec{r},t)].\end{aligned} \tag{20}$$

If the first interaction can be considered as instantaneous, then

$$k_{on1}[C][\text{free}(\vec{r},t)] = k_{off1}[\text{bound1}(\vec{r},t)]. \tag{21}$$

The free pool of proteins seen in the case of PAGFP-SUV39H1 corresponds to proteins that are not stabilized, i.e. to$[(f+b1)(\vec{r},t)] = [\text{free}(\vec{r},t)] + [\text{bound1}(\vec{r},t)]$, which is described by the sum of the two first equations of Eq. 20,

$$\begin{aligned}\frac{\partial[(f+b1)(\vec{r},t)]}{\partial t} &= D\Delta([\text{free}(\vec{r},t)]) - k_{on2}[\text{bound1}(\vec{r},t)] \\ &\quad + k_{off2}[\text{bound2}(\vec{r},t)],\end{aligned}$$

i.e., using Eq. 21,

$$\begin{aligned}\frac{\partial[(f+b1)(\vec{r},t)]}{\partial t} &= (D * k_{off1}/(k_{off1} + k_{on1}[C]))\Delta([(f+b1)(\vec{r},t)]) \\ &\quad - k_{on2} * k_{on1}[C]/(k_{off1} + k_{on1}[C])[(f+b1)(\vec{r},t)] \\ &\quad + k_{off2}[\text{bound2}(\vec{r},t)],\end{aligned}$$

which is equivalent to the reaction-diffusion Eq. 4, by replacing $[\text{free}(\vec{r},t)]$ by $[\text{free}(\vec{r},t)]+[\text{bound1}(\vec{r},t)]$ and the diffusion coefficient by an apparent one which is its product with the fraction of free proteins regarding only the first reaction:$[\text{free}(\vec{r},t)]/([\text{free}(\vec{r},t)]+[\text{bound1}(\vec{r},t)])$.

SUPPLEMENTARY MATERIAL

An online supplement to this article can be found by visiting BJ Online at http://www.biophysj.org.

We thank Iain Mattaj for the kind gift of the RCC1 cDNA, Howard Worman for the kind gift of the HP1β cDNA, and Christine Ruckenbauer and Jan Michael Peters for the kind gift of GFP-SUV39H1 and GFP-SUV39H1-H320R. We also thank Werner Albig and Detlef Doenecke for the kind gift of the five H1 isoform cDNAs. J.E. acknowledges funding from the German Research Council (DFG grant No. EL 246/1-1 and grant No. EL 246/2-1/2).

REFERENCES

1. Houtsmuller, A. B., S. Rademakers, A. L. Nigg, D. Hoogstraten, J. H. Hoeijmakers, and W. Vermeulen. 1999. Action of DNA repair endonuclease ERCC1/XPF in living cells. *Science*. 284:958–961.
2. Phair, R. D., and T. Misteli. 2000. High mobility of proteins in the mammalian cell nucleus. *Nature*. 404:604–609.
3. Misteli, T., A. Gunjan, R. Hock, M. Bustin, and D. T. Brown. 2000. Dynamic binding of histone H1 to chromatin in living cells. *Nature*. 408:877–881.
4. McNally, J. G., W. G. Muller, D. Walker, R. Wolford, and G. L. Hager. 2000. The glucocorticoid receptor: rapid exchange with regulatory sites in living cells. *Science*. 287:1262–1265.
5. Bubulya, P. A., and D. L. Spector. 2004. On the movements of nuclear components in living cells. *Exp. Cell Res.* 296:4–11.
6. Phair, R. D., P. Scaffidi, C. Elbi, J. Vecerova, A. Dey, K. Ozato, D. T. Brown, G. Hager, M. Bustin, and T. Misteli. 2004. Global nature of dynamic protein-chromatin interactions in vivo: three-dimensional genome scanning and dynamic interaction networks of chromatin proteins. *Mol. Cell. Biol.* 24:6393–6402.
7. Belmont, A. 2003. Dynamics of chromatin, proteins, and bodies within the cell nucleus. *Curr. Opin. Cell Biol.* 15:304–310.
8. Hager, G. L., C. Elbi, and M. Becker. 2002. Protein dynamics in the nuclear compartment. *Curr. Opin. Genet. Dev.* 12:137–141.
9. Phair, R. D., and T. Misteli. 2001. Kinetic modelling approaches to in vivo imaging. *Nat. Rev. Mol. Cell Biol.* 2:898–907.
10. Lippincott-Schwartz, J., E. Snapp, and A. Kenworthy. 2001. Studying protein dynamics in living cells. *Nat. Rev. Mol. Cell Biol.* 2:444–456.
11. Patterson, G. H., and J. Lippincott-Schwartz. 2002. A photoactivatable GFP for selective photolabeling of proteins and cells. *Science*. 297: 1873–1877.
12. Axelrod, D., D. E. Koppel, J. Schlessinger, E. Elson, and W. W. Webb. 1976. Mobility measurement by analysis of fluorescence photobleaching recovery kinetics. *Biophys. J.* 16:1055–1069.
13. Kaufman, E. N., and R. K. Jain. 1990. Quantification of transport and binding parameters using fluorescence recovery after photobleaching. Potential for in vivo applications. *Biophys. J.* 58:873–885.
14. Berk, D. A., F. Yuan, M. Leunig, and R. K. Jain. 1993. Fluorescence photobleaching with spatial Fourier analysis: measurement of diffusion in light-scattering media. *Biophys. J.* 65:2428–2436.
15. Tsay, T. T., and K. A. Jacobson. 1991. Spatial Fourier analysis of video photobleaching measurements. Principles and optimization. *Biophys. J.* 60:360–368.
16. Tardy, Y., J. L. McGrath, J. H. Hartwig, and C. F. Dewey. 1995. Interpreting photoactivated fluorescence microscopy measurements of steady-state actin dynamics. *Biophys. J.* 69:1674–1682.
17. Coscoy, S., F. Waharte, A. Gautreau, M. Martin, D. Louvard, P. Mangeat, M. Arpin, and F. Amblard. 2002. Molecular analysis of microscopic ezrin dynamics by two-photon FRAP. *Proc. Natl. Acad. Sci. USA*. 99:12813–12818.
18. Sprague, B. L., R. L. Pego, D. A. Stavreva, and J. G. McNally. 2004. Analysis of binding reactions by fluorescence recovery after photobleaching. *Biophys. J.* 86:3473–3495.
19. Farla, P., R. Hersmus, B. Geverts, P. O. Mari, A. L. Nigg, H. J. Dubbink, J. Trapman, and A. B. Houtsmuller. 2004. The androgen receptor ligand-binding domain stabilizes DNA binding in living cells. *J. Struct. Biol.* 147:50–61.
20. Bulinski, J. C., D. J. Odde, B. J. Howell, T. D. Salmon, and C. M. Waterman-Storer. 2001. Rapid dynamics of the microtubule binding of ensconsin in vivo. *J. Cell Sci.* 114:3885–3897.
21. Dundr, M., U. Hoffmann-Rohrer, Q. Hu, I. Grummt, L. I. Rothblum, R. D. Phair, and T. Misteli. 2002. A kinetic framework for a mammalian RNA polymerase in vivo. *Science*. 298:1623–1626.
22. Rabut, G., V. Doye, and J. Ellenberg. 2004. Mapping the dynamic organization of the nuclear pore complex inside single living cells. *Nat. Cell Biol.* 6:1114–1121.

23. Phair, R. D., S. A. Gorski, and T. Misteli. 2004. Measurement of dynamic protein binding to chromatin in vivo, using photobleaching microscopy. *Methods Enzymol.* 375:393–414.

24. Nemergut, M. E., C. A. Mizzen, T. Stukenberg, C. D. Allis, and I. G. Macara. 2001. Chromatin docking and exchange activity enhancement of RCC1 by histones H2A and H2B. *Science.* 292:1540–1543.

25. Rea, S., F. Eisenhaber, D. O'Carroll, B. D. Strahl, Z. W. Sun, M. Schmid, S. Opravil, K. Mechtler, C. P. Ponting, C. D. Allis, and T. Jenuwein. 2000. Regulation of chromatin structure by site-specific histone H3 methyltransferases. *Nature.* 406:593–599.

26. Brown, D. T. 2003. Histone H1 and the dynamic regulation of chromatin function. *Biochem. Cell Biol.* 81:221–227.

27. Gerlich, D., J. Beaudouin, B. Kalbfuss, N. Daigle, R. Eils, and J. Ellenberg. 2003. Global chromosome positions are transmitted through mitosis in mammalian cells. *Cell.* 112:751–764.

28. Verhoeyen, E., H. Hauser, and D. Wirth. 2001. Evaluation of retroviral vector design in defined chromosomal loci by FLP-mediated cassette replacement. *Hum. Gene Ther.* 12:933–944.

29. Reid, G., M. Hübner, R. Métivier, H. Brand, S. Denger, D. Manu, J. Beaudouin, J. Ellenberg, and F. Gannon. 2003. Cyclic, proteasome-mediated turnover of unliganded and liganded ER-α on responsive promoters is an integral feature of estrogen signaling. *Mol. Cell.* 11:695–707.

30. Gerlich, D., J. Beaudouin, M. Gebhard, J. Ellenberg, and R. Eils. 2001. Four-dimensional imaging and quantitative reconstruction to analyse complex spatiotemporal processes in live cells. *Nat. Cell Biol.* 3:852–855.

31. Rabut, G., and J. Ellenberg. 2004. Automatic real-time three-dimensional cell tracking by fluorescence microscopy. *J. Microsc.* 216(Pt2): 131–137.

32. Bormann, G. B., and F. De Schutter. E. 2001. Computational Modeling of Genetic and Biochemical Networks. MIT Press, Cambridge, MA. 189–224.

33. Kimura, H., and P. R. Cook. 2001. Kinetics of core histones in living human cells: little exchange of H3 and H4 and some rapid exchange of H2B. *J. Cell Biol.* 153:1341–1353.

34. Chubb, J. R., S. Boyle, P. Perry, and W. A. Bickmore. 2002. Chromatin motion is constrained by association with nuclear compartments in human cells. *Curr. Biol.* 12:439–445.

35. Abney, J. R., B. Cutler, M. L. Fillbach, D. Axelrod, and B. A. Scalettar. 1997. Chromatin dynamics in interphase nuclei and its implications for nuclear structure. *J. Cell Biol.* 137:1459–1468.

36. Gerlich, D., J. Mattes, and R. Eils. 2003. Quantitative motion analysis and visualization of cellular structures. *Methods.* 29:3–13.

37. Fink, C., F. Morgan, and L. M. Loew. 1998. Intracellular fluorescent probe concentrations by confocal microscopy. *Biophys. J.* 75:1648–1658.

38. Braeckmans, K., L. Peeters, N. N. Sanders, S. C. De Smedt, and J. Demeester. 2003. Three-dimensional fluorescence recovery after photobleaching with the confocal scanning laser microscope. *Biophys. J.* 85:2240–2252.

39. Siggia, E. D., J. Lippincott-Schwartz, and S. Bekiranov. 2000. Diffusion in inhomogeneous media: theory and simulations applied to whole cell photobleach recovery. *Biophys. J.* 79:1761–1770.

40. Swaminathan, R., C. P. Hoang, and A. S. Verkman. 1997. Photobleaching recovery and anisotropy decay of green fluorescent protein GFP-S65T in solution and cells: cytoplasmic viscosity probed by green fluorescent protein translational and rotational diffusion. *Biophys. J.* 72:1900–1907.

41. Terry, B. R., E. K. Matthews, and J. Haseloff. 1995. Molecular characterisation of recombinant green fluorescent protein by fluorescence correlation microscopy. *Biochem. Biophys. Res. Commun.* 217: 21–27.

42. Franks, F. 1972. Water: A Comprehensive Treatise. Plenum Press, New York, London.

43. Seksek, O., J. Biwersi, and A. S. Verkman. 1997. Translational diffusion of macromolecule-sized solutes in cytoplasm and nucleus. *J. Cell Biol.* 138:131–142.

44. Wachsmuth, M., W. Waldeck, and J. Langowski. 2000. Anomalous diffusion of fluorescent probes inside living cell nuclei investigated by spatially resolved fluorescence correlation spectroscopy. *J. Mol. Biol.* 298:677–689.

45. Lukacs, G. L., P. Haggie, O. Seksek, D. Lechardeur, N. Freedman, and A. S. Verkman. 2000. Size-dependent DNA mobility in cytoplasm and nucleus. *J. Biol. Chem.* 275:1625–1629.

46. Hutchins, J. R., W. J. Moore, F. E. Hood, J. S. Wilson, P. D. Andrews, J. R. Swedlow, and P. R. Clarke. 2004. Phosphorylation regulates the dynamic interaction of RCC1 with chromosomes during mitosis. *Curr. Biol.* 14:1099–1104.

47. Cushman, I., D. Stenoien, and M. S. Moore. 2004. The dynamic association of RCC1 with chromatin is modulated by RAN-dependent nuclear transport. *Mol. Biol. Cell.* 15:245–255.

48. Li, H. Y., D. Wirtz, and Y. Zheng. 2003. A mechanism of coupling RCC1 mobility to RanGTP production on the chromatin in vivo. *J. Cell Biol.* 160:635–644.

49. Crank, J. 1975. The Mathematics of Diffusion. Oxford University Press, Oxford, UK.

50. Lachner, M., D. O'Carroll, S. Rea, K. Mechtler, and T. Jenuwein. 2001. Methylation of histone H3 lysine 9 creates a binding site for HP1 proteins. *Nature.* 410:116–120.

51. Lever, M. A., J. P. Th'ng, X. Sun, and M. J. Hendzel. 2000. Rapid exchange of histone H1.1 on chromatin in living human cells. *Nature.* 408:873–876.

52. Soumpasis, D. M. 1983. Theoretical analysis of fluorescence photobleaching recovery experiments. *Biophys. J.* 41:95–97.

53. Catez, F., H. Yang, K. J. Tracey, R. Reeves, T. Misteli, and M. Bustin. 2004. Network of dynamic interactions between histone H1 and high-mobility-group proteins in chromatin. *Mol. Cell. Biol.* 24: 4321–4328.

54. Alberts, B. 1994. Molecular Biology of the Cell, 3rd Ed. Garland, New York.

55. Bilbao-Cortes, D., M. Hetzer, G. Langst, P. B. Becker, and I. W. Mattaj. 2002. RAN binds to chromatin by two distinct mechanisms. *Curr. Biol.* 12:1151–1156.

56. Ura, K., K. Nightingale, and A. P. Wolffe. 1996. Differential association of HMG1 and linker histones B4 and H1 with dinucleosomal DNA: structural transitions and transcriptional repression. *EMBO J.* 15:4959–4969.

57. Riggs, A. D., S. Bourgeois, and M. Cohn. 1970. The lac repressor-operator interaction. 3. Kinetic studies. *J. Mol. Biol.* 53:401–417.

58. Halford, S. E., and J. F. Marko. 2004. How do site-specific DNA-binding proteins find their targets? *Nucleic Acids Res.* 32:3040–3052.

59. von Hippel, P. H., and O. G. Berg. 1989. Facilitated target location in biological systems. *J. Biol. Chem.* 264:675–678.

60. Misteli, T. 2001. Protein dynamics: implications for nuclear architecture and gene expression. *Science.* 291:843–847.